Epitaxie de couches d'alliages quaternaires à base d'InAlGaN pour les transistors de haute performance

Mrad Mrad

THÈSE

Pour obtenir le grade de

DOCTEUR DE L'UNIVERSITE GRENOBLE ALPES

Spécialité : **Physique des matériaux**

Arrêté ministériel : 25 mai 2016

Présentée par

Mrad MRAD

Thèse dirigée par **Guy FEUILLET** et encadrée par **Matthew CHARLES**

Préparée au sein du **CEA-LETI**
Dans **l'École Doctorale de Physique - Grenoble**

Epitaxie de couches d'alliages quaternaires à base d'InAlGaN pour les transistors de haute performance

Thèse soutenue publiquement le **7 Juillet 2020** devant le jury composé de:

Mme Sylvie CONTRERAS
Chargée de recherche, Université de Montpellier II, Rapporteur
M. Yvon CORDIER
Directeur de Recherche, CRHEA - CNRS Valbonne, Rapporteur
M. Etienne GHEERAERT
Professeur, Université Joseph Fourier - Institut Néel, Président
Mme Marie LESECQ
Maître de conférences, Université de Lille 1, Examinateur
Mme Rachel OLIVER
Professeur, Université de Cambridge, Examinateur
M. Guy FEUILLET
Directeur de Recherche, CEA-LETI, Directeur de thèse
M. Matthew CHARLES
Ingénieur de recherche, CEA-LETI, Co-Encadrant de thèse

[Science is] the desire to know causes – William Hazlitt

Acknowledgments

This PhD work has been carried out at the CEA-LETI laboratory in Grenoble. Behind this achievement, there are a great many people, who gave me help, support and inspiration so that it was made possible. Therefore, I take this opportunity to express my special gratitude to all of them for contributing to my thesis success.

First, I would like to genuinely thank my thesis director ***Guy Feuillet*** *for believing in me and giving me the opportunity to join the LETI lab and conduct three years of research under his direction. Guy is someone you will instantly love and never forget once you meet him. He's the funniest advisor and one of the smartest people I know. I would like to thank him for having given me his vision of research and his working methods in order to guarantee the rigor required by the scientific work.*

I thank the members of my thesis jury, Dr. ***Sylvie Contreras,*** *Dr.* ***Yvon Cordier,*** *Prof.* ***Etienne Gheeraert,*** *Dr.* ***Marie Lesecq,*** *and Prof.* ***Rachel Oliver*** *for devoting their time to read this manuscript. Furthermore, I would like to thank them for their constructive comments and remarks.*

My warmest thanks go to my thesis supervisor ***Matthew Charles*** *to whom I present my deep gratitude for his excellent supervision, his many advices and for all the hours he devoted to the good conduct of this research work. I am sure that I could not have done all the work without his encouragements, motivation and patience. I would also like to tell him how much I appreciated his great availability and his respect for the tight deadlines for proofreading the documents I sent to him. Finally, I was very sensitive to his good humor which made our collaboration very pleasant.*

In addition, I would like to cordially thank the following lab members who have been of assistance to me during my PhD in a wide variety of roles: ***Laurent Vandroux, Sylvain Maitrejean, Anne Roule, Lucile Roulet, Amelie Dussaigne, Pierre Ferret, Yann Mazel, Jérôme Richy*** *and* ***Matthieu Lafossas.***

I would also like to extend my gratitude to my closest friends who never wavered in their support: ***Rami Khazaka, Christelle Salameh, Salim Assaf, Rodaina Aboul Hosn, Halim Hanna, Roy Dagher, Tamara Oueidat, Houssein Dirani, Jessy Hasna, Elias Haber, Elio Asmar, Hassan Dirani, Georgio Zemar, Carole Pernel, Victor Yon, Rebecca Chahine, Samer Dagher, Loraine Youssef, Benjamin Samuel,*** *and* ***Sofia Boughaleb.*** *I will never forget the good times we shared together.*

My special thanks go then to my girlfriend ***Joyce Stephan,*** *definitely you were a source of inspiration and determination. You came at the perfect time. Thank you for motivating and filling me with affection during moments of doubt and weakness. Thank you for never giving up on me. My love, this thesis is ours, and its end heralds a new step for both of us. I can't wait to find out what awaits us!*

Last but not least, and with great affection, I would like to thank every member of my family for their unconditional and unlimited support. Particularly, I would like to thank my beloved parents, Bayeh ***Georges Mrad*** *and Emmeh* ***Samira Mrad,*** *to whom this PhD is dedicated. Bayeh, Emmeh, I can never express to you how proud I am to have you as parents. Thank you for being my first fans, and for giving me exceptional attention and confidence since the first second of my life. I will never forget the nights you spent watching over my morals, my health and my studies. Thank you for your sacrifice, love, comfort and unconditional support. Without you, I could never have done all this! I would also like to thank my beloved sisters* ***Marguerite Mrad*** *and* ***Christine Mrad*** *and my brother* ***Elie Mrad.*** *It is a blessing to have someone to count on. All these years, you have always been my rock and my shield. You kept me away from harm and guided me with your advices. I would not be who I am now if not for you. Thank you! Your endless love, support and invaluable help made it all possible and brought this work to a happy end.*

Mrad Mrad
10th of April 2020

GENERAL TABLE OF CONTENTS

LIST OF FIGURES

LIST OF TABLES

General introduction

The optical, electrical, mechanical, and thermal properties of the group III-N semiconductors make them excellent materials for many electronic and optoelectronic applications. In particular, the high breakdown field, high electron mobility and high thermal conductivity favor their use for high power transistors and diodes, and for radio-frequency transistors. The work of this thesis is mainly focused on the metal organic vapor phase epitaxy (MOVPE) growth of III-N materials, in particular InAlN/GaN structures on 200 mm silicon substrates for high power performance high electron mobility transistors (HEMTs).

Currently, CEA-LETI produces GaN based HEMTs on Si(111) wafers using AlGaN/GaN heterostructures. However, the growth of InAlN barriers on GaN buffers has demonstrated the possibility to surpass AlGaN on GaN performance. On the other hand, growing high quality InAlN/GaN HEMTs is in general more difficult than growing its AlGaN/GaN counterparts. This issue comes from the strong immiscibility effect between InN and AlN, resulting from their big lattice parameter difference. Another challenge is the big difference in growth parameters of its two binaries InN and AlN which makes it difficult to optimize the growth conditions. Finally, a serious problem in Close Coupled Showerhead (CCS) MOVPE growth chambers for the growth of pure InAlN barriers is the non-intentional incorporation of Ga. Gallium pollution affects the control and the reproducibility of the desired growth recipes of InAlN barriers. This therefore also affects the structural and electrical properties of these ternary epilayers. The objectives of this work are to firstly understand and control the gallium contamination in CCS reactors, and later to find a solution to avoid this contamination through the understanding of the main parameters affecting it. Achieving these two main objectives would enable us to grow well controlled and pure InAlN barriers.

In the first chapter of this work, after highlighting the key historical events of the III-Ns developments, we will detail their general properties. We will deal with the different substrates that allow GaN crystalline growth and detail the different crystalline structures that can be grown. Then we will investigate III-N intrinsic material properties with a focus

on the polarization effects. Later, we will discuss the use of the III-N elements for electronic applications, mainly in the fields of power and high frequency electronics, with a focus on InAlN/GaN/Si HEMT where we present the state of the art of Rsheet values.

The second chapter combines experimental and theoretical details. In a first part we will examine the different epitaxial techniques used for the growth of III-N semiconductor materials, with a focus on MOVPE, the method we used for the growth of our III-N samples. Next, we will detail the AIXTRON growth equipment and its different parts, which are critical for the good control of the MOVPE growth epitaxy of III-N layers. In a second part, we will discuss the different physical and chemical characterizations techniques we frequently performed during this work: Atomic Force Microscopy (AFM) for morphological characterization, Low-Temperature Photo-Luminescence spectroscopy (LT-PL) and Wavelength Dispersive X-Ray Fluorescence (WDXRF) for optical characterization, High Resolution X-Ray Diffraction (HR-XRD) and X-Ray Reflectivity (XRR) for structural characterization, Secondary Ion Mass Spectrometry (SIMS) and Plasma Profiling Time of Flight Mass Spectrometry (PP-TOFMS) for chemical characterization and finally Four-Point Probe (4PP) for electrical characterization.

In the third chapter, we will be focusing on understanding and quantifying the gallium contamination problem in the AIXTRON CCS chamber architecture on the MOVPE growth of InAlN barrier layers. We show reduced indium incorporation and increased gallium non-intentional incorporation in the InAlN barrier layers along with an increase in the thickness of these layers as the gallium contamination increases. Here, we propose a quantitative model for these observations where we suggest that the TMIn precursor reacts with gallium on the showerhead shield surface to release TMGa, which is then incorporated as Ga into the layers. We showed the possibility of avoiding gallium pollution by growing the barrier layers directly on a GaN template after removing the samples from the chamber and cleaning the chamber. However, this increased the resulting sheet resistance, likely due to oxidation and contamination when the wafers were outside the growth tool. We then introduced hydrogen and chlorine etching of the GaN surface and solved this issue while avoiding any Ga pollution in the InAlN layers.

In the fourth chapter, we investigate the effect of Ga pollution on the growth of InGaN layers, as this ternary is interesting for optoelectronic applications. We show that there is a

strong effect of the gallium pollution on the MOVPE growth of InGaN layers. The effect is more pronounced both for increased GaN regrowth thicknesses after growth interruption and for higher TMIn flows. We show in particular that when working under typical MQW growth conditions, gallium pollution has very strong effects on the thickness of InGaN layers, with an increase of a factor of two due to the gallium pollution. Performing the InGaN growth in a clean chamber shows more easily interpretable results, and more predictable growth behavior, with no change in thickness or composition of InGaN layers when changing the TMIn flows.

In the fifth and final chapter, we discuss the possibility of overcoming gallium pollution in CCS reactors through the understanding of the main parameters affecting it. We firstly show that by changing the growth conditions of GaN buffer layers to reduce Ga desorption, we can reduce the gallium pollution in InAlN layers, but only by a factor of around two. Using AlGaN buffer layers, the gallium pollution is well suppressed, but this is not a solution for electrical devices. Later, we show for the first time the strong link between the temperature of a deposition shield mounted on the front side of the showerhead during the growth of GaN buffer layers and gallium contamination in InAlN layers. Increasing the shield temperature during GaN buffer growth allowed us to significantly reduce the gallium pollution in our layers. We have found in particular a linear relationship between the increase of shield temperature and the decrease of the Ga% into very low values in InAlN layers when GaN were grown beforehand using H_2 as a carrier gas. Also, when GaN was grown using N_2 as a carrier gas, the shield temperature was increased by 90 °C higher than for the reference sample (where we used H_2 as a carrier gas), thanks to the low thermal conductivity of N_2 versus H_2. In addition to the reduced desorption of GaN during growth under N_2, this resulted in very low nonintentional incorporation of around 2% into the InAlN barrier. This led us to heterostructures with no gallium pollution and a very low Rsheet value of 201 Ohm/sq. These results are very interesting for the replacements of conventional AlGaN/GaN barriers by InAlN/GaN, with well controlled, pure and higher performance InAlN/GaN barriers for power and RF applications.

We will end the manuscript with a big conclusion where we highlight the most significant results of this work, then we will consider the work perspectives based on these results. At the end we will expose the scientific publications resulted from this thesis.

Chapter I: Nitride semiconductors

I.1 Introduction

In this first chapter of the manuscript, we start with a brief introduction on III-Nitride materials followed by some key historical events on their development. Then, we will discuss the typical substrates used for the crystalline growth of GaN. Next, we will discuss III-Nitride properties, with a main focus on the different crystalline structures that can be grown. Additionally, we will investigate III-N intrinsic material properties with a focus on the polarization effects. Later we will discuss the specificities of the III-N elements for electronic applications. We will also discuss III-N based applications mainly in the fields of power and high frequency electronics, such as on InAlN/GaN/Si HEMT where we present the state of the art of Rsheet values. We finish this chapter with the general objective of this research.

I.2 III-Nitride and historical key events

The optical, electrical, mechanical, and thermal properties of the group III-nitride (III-N) semiconductors, which include a range of materials such as gallium nitride (GaN), aluminum nitride (AlN), indium nitride (InN), and their ternary (InAlN, InGaN, AlGaN) and quaternary (InAlGaN) alloys, make them excellent materials for many applications. In particular, their direct band gap energy ranges from 0.7 (for InN) [1] to 3.39 (for GaN) [2] up to 6.2 eV (for AlN) [3] covers a broad spectral range, from 200 up to 1800 nm.

Their overall properties allow several uses in optoelectronics, power electronic components, light-emitting diodes (LEDs), laser diodes (LDs) and photodetectors [4, 5, 6, 7]. Other interesting properties of these materials are high breakdown field, high electron mobility and high thermal conductivity, shown in Table 2 and Table 3. These properties favor high frequency and high power applications such as power transistors [4, 8], high electron mobility transistors (HEMTs) [9] and microwave power switches [4].

Nitride materials have been extensively studied. Their discovery was initiated over a century ago in 1907 when Fichter et al. [10] successfully synthesized AlN and InN materials [11], this was followed by the successful synthesis of the third crucial III-N binary, GaN, in the 1930s by Johnson et al. [12] and Juza et al. [13]. The synthesis of GaN was performed by passing ammonia (NH_3) over liquid gallium at elevated temperatures.

For more than thirty years, there were no significant improvements in nitride materials and they did not attract much interest at that time, as they were made from polycrystalline materials.

Then, in 1969, Maruska and Titjen demonstrated that GaN can be grown on sapphire (Al_2O_3) using chemical vapor deposition (CVD) [14]. However, the late 1970s saw a drop in research in the GaN field due to the difficulties encountered with the growth of the high quality epilayers needed for device development.

Persistent problems were: the choice and the availability of a suitable substrate for the growth of good quality GaN, and the difficulties of obtaining a p-type GaN. In 1982, only a handful of articles were published worldwide on the GaN system.

It was not until 1986 that Amano et al. obtained a GaN layer with greatly improved morphological, optical and electrical properties. This layer was obtained by Metal Organic Chemical Vapor Deposition (MOCVD) also known as Metal Organic Vapor Phase Epitaxy (MOVPE) growth on sapphire substrate, via an AlN nucleation layer [15]. In 1989, the same team was the first to develop a p-type conductive GaN layer [16]. These discoveries led to the revival of GaN in the early 1990s.

In 1991, Khan et al. were the first to give proof of a two-dimensional electron gas (2DEG) formed by an $Al_xGa_{1-x}N$/GaN heterojunction on sapphire, giving a new perspective of actively using this material for electrical applications [17]. In 1993 and 1994 Khan et al. were the first to fabricate GaN HEMTs by MOCVD using sapphire substrates [18, 19]. At the same time in 1993, Nakamura et al. at Nichia grew the first GaN blue light emitting diode [20]; which was followed by their mass production in 1996 at Nichia.

After these initial steps, the research and commercialization of GaN-based devices has progressed a lot. Today, the production technologies, reproducibility and reliability of the epitaxial material are the key developments ongoing to continue to meet the great promise of GaN-based devices.

I.3 III-Nitride properties

I.3.1 Substrate of choice

Preferably, GaN growth would be performed on bulk GaN substrates [21]. Although the development and manufacture of bulk and freestanding GaN wafers has been demonstrated, GaN substrates are typically small in diameter and expensive, especially for industrial use. Consequently, the growth of GaN has been developed on many substitution substrates such as sapphire (Al_2O_3), silicon carbide (SiC), or silicon (Si) whose crystalline and thermal characteristics are listed in Table 1.

	GaN freestanding	Al_2O_3	SiC	Si(111)
In-plane lattice mismatch with GaN (%)	0	16	3.1	-17
GaN surface dislocation density range when grown on foreign substrate (cm^{-2})	~10^6	~10^8	~10^8	~10^8-10^9
Crystalline structure	Hexagonal	Hexagonal	Hexagonal	Cubic
Thermal expansion coefficients ($10^{-6}K^{-1}$)	5.6	7.5	4.4	2.6
Thermal conductivity (W/cm.K)	1.3	0.5	4.5	1.5
Melting point (°C)	2500	2030	2500	1410
Max wafer size (mm)	100	200	150	300
Wafer price	Very high	Medium	High	Low

Table 1: Most used bulk substrates for wurtzite GaN growth. [21]

The growth of good crystallographic quality GaN buffer layers on foreign substrates cited above (sapphire, SiC, Si) is a true challenge due to the lattice mismatch between the buffer and the substrate. This lattice mismatch gives rise to a high density of structural defects such as dislocations.

In particular, a major challenge in the growth of GaN on Si(111) is the large mismatch of the in-plane thermal expansion coefficient seen in Table 1. This leads to cracking in the GaN layer when cooling the heterostructure from the growth temperature to room temperature. To overcome this CTE mismatch, combinations of buffer layers have been implemented that make it possible to induce a large amount of compressive strain into the layers during growth, so that when cooling to room temperature the wafer becomes flat. One strategy is to progressively increase the lattice parameter from the AlN nucleation layer to the GaN channel. This allows the growth of crack-free nitride layers up to 6 or 7 µm thick.

Historically, sapphire was the first substrate used for GaN growth due to its reasonable cost, stability at very high temperature and transparency over the entire visible spectrum. However, for electronic applications, sapphire has strong competition from other substrates

such as SiC and Si, due to its low thermal conductivity, which limits the power density of the devices.

SiC is a good substrate for the growth of high quality GaN without the need to use complex buffer layers as in the case of GaN on silicon (111). With excellent thermal conductivity as seen in Table 1, SiC allows a better dissipation of the heat. Unfortunately, SiC is only available up to 150 mm diameter and its cost remains high. This is therefore only used when absolutely necessary for the components obtained.

Silicon is low cost, available and easy to develop. It has a better thermal conductivity than sapphire (1.5 W/cm.K against 0.5 W/cm.K for sapphire), in addition to its price which is much lower than SiC, and its availability in large wafer diameter (up to 300 mm). Moreover, the growth of GaN on silicon could allow the integration of III-N based devices with many technologies in the silicon industry.

Therefore, LETI has made the strategic choice to opt for silicon substrates because it already has a platform and a dedicated line for silicon (i.e. 200 mm and 300 mm compatible CMOS cleanroom). Moreover, despite the many technological challenges (lattice mismatch, structural defects, etc.) imposed by GaN deposition on silicon, this remains an attractive economic solution for industrial production of power devices.

I.3.2 Crystalline structures

The III-nitride materials, such as GaN, AlN, InN and their ternary and quaternary alloys share three distinctive crystal structures, which are rock-salt, zinc-blende and wurtzite. The rock-salt structure, pictured in Figure 1 a, can be obtained at very high pressure conditions, thanks to the reduction of the lattice dimensions, which causes inter-ionic coulomb interaction to favor ionicity over covalent nature [22]. However, the rock-salt structure is a non-compatible structure for industrial applications, as it cannot be obtained by any epitaxial growth. Another crystal structure for III-N materials is the zinc-blende structure, pictured in Figure 1 b, this structure is composed of two interpenetrating face-centered cubic sublattices displaced by one quarter of a body diagonal. However, this crystal structure is less thermodynamically stable under ambient conditions than the wurtzite structure, pictured in Figure 1 c, meaning that the wurtzite structure is typically preferred [23]. We note that for Al, Ga, and In elements, we have electronegativity values of 1.61,

1.81, and 1.78 respectively. On the other hand, for N atoms, we have a higher electronegativity value of 3.04, compared to the metal elements. [24]

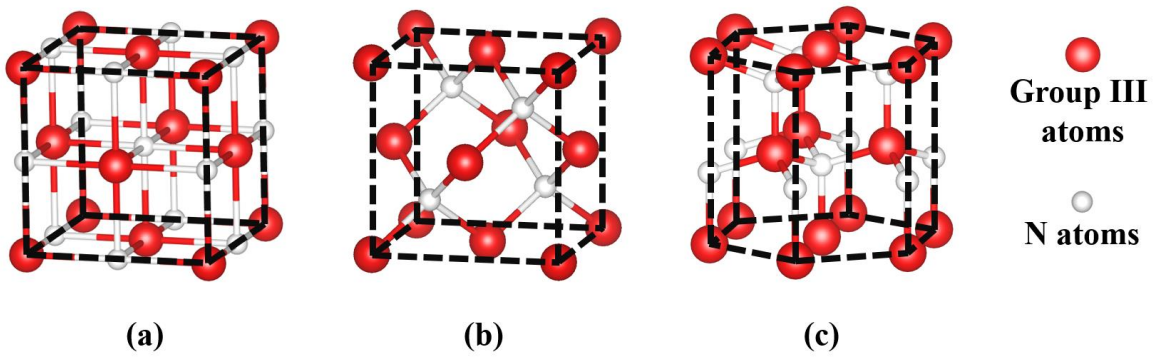

Figure 1: Illustration of a) rock-salt b) zinc-blende and c) wurtzite crystal structures.

The wurtzite crystalline structure consists of two interpenetrating hexagonal lattices, as shown in Figure 2a. One lattice containing group III atoms and the other N atoms, interpenetrated and shifted by u = 3/8.c along the c-axis, with respect to each other. u is the length of the anion-cation bond and c is the height of the elementary lattice.

We can notice from this figure that the wurtzite crystal structure shows non-symmetry along the c-axis, e.g. the [0001] direction. Thus, [0001] and $[000\bar{1}]$ directions are not equivalent. Therefore, this leads to two different faces of GaN.

The Ga-face (in the [0001] direction) and the N-face (in the $[000\bar{1}]$ direction), shown in Figure 2b and 2c, which corresponds to gallium polarity and nitrogen polarity, respectively.

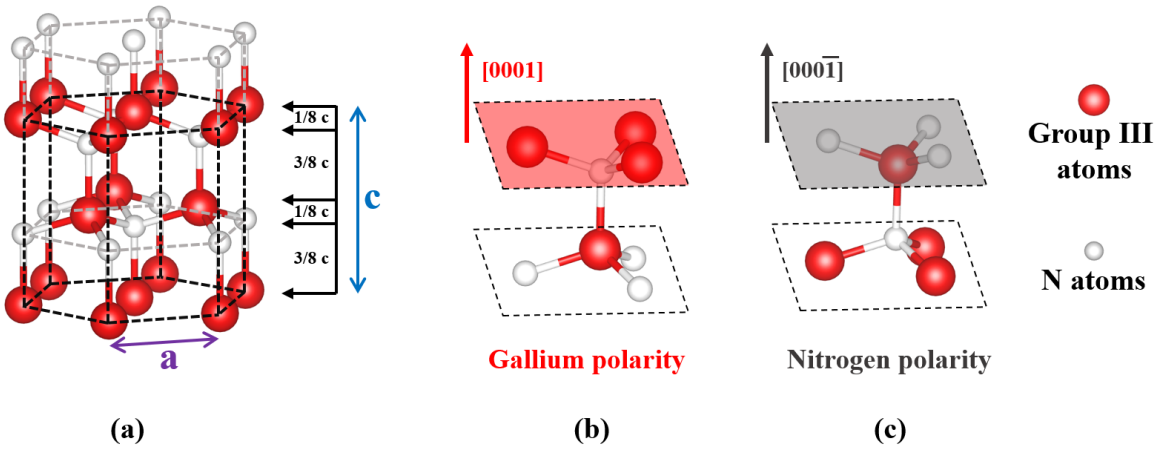

Figure 2: a) III-N wurtzite crystal structure showing the two interpenetrating hexagonal lattices. b) crystallographic orientation [0001] and c) [000$\bar{1}$] as a function of gallium and nitrogen polarity.

It is important to note that surface polarity strongly affects the final chemical, morphological, and electrical properties of the grown GaN surface templates. We note that these two different surface polarities can be obtained using specific growth conditions.

A gallium surface polarity results in a smooth GaN surface morphology in typical growth conditions for MOVPE, while nitrogen surface polarity tends to a higher surface roughness. This is one of the main reasons for the initial development of LEDs, LDs, and HEMT devices on Ga-polar GaN templates.

However, recently, N-polar GaN templates have shown an increased attention, thanks to alternative device geometries which can be obtained from the flipped spontaneous and piezoelectric polarizations.

In the next paragraphs, we will discuss the different type of polarizations presented within the wurtzite crystalline structure and their origin.

I.3.3 Spontaneous polarization

As previously discussed, GaN material grown in the wurtzite structure is asymmetric along the c-axis, and, as mentioned, nitrogen electronegativity is high compared to that of group III atoms [24]. Together these properties lead to the creation of an electric dipole

moment directed towards the metal atom along the tetrahedron bonds of the wurtzite structure as pictured in Figure 3a.

Each tetrahedron has an elementary dipole created by the non-superposition of the barycenter of the negative charges with that of the positive charges. These dipoles are added up to produce a macroscopic spontaneous polarization directed along the growth axis of the material, as can be seen from Figure 3b. This effect is called spontaneous polarization (Psp) as it occurs at equilibrium stage independently of the material stress state.

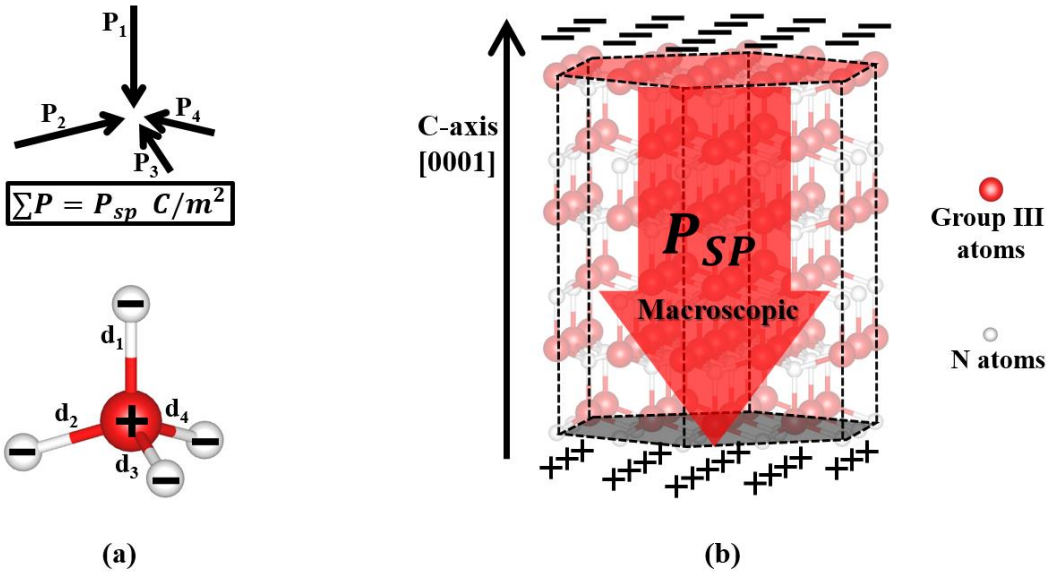

Figure 3: a) Tetrahedron bonding showing dipolar moments and spontaneous polarizations. b) Macroscopic spontaneous polarization and charge repartition at the interfaces of c-axis metal-face of III-N structure.

The spontaneous polarization values of GaN, AlN, and InN are respectively -0.029 $C.m^{-2}$, -0.081 $C.m^{-2}$, and -0.032 $C.m^{-2}$ [25]. The negative P_{sp} sign indicates that the polarization vector is oriented in the opposite direction to the direction of growth [0001].

According to Vegard's law, the spontaneous polarization in a $A_XB_{1-X}D$ ternary and $A_XB_XC_{1-X-Y}D$ quaternary alloys can be determined as follows:

$$P_{sp,A_XB_{1-X}D}(X) = P_{sp,AD}X + (1-X)P_{sp,BD} \qquad \textit{Eq. 1}$$

$$P_{sp,A_XB_YC_{1-X-Y}D}(X,Y) = P_{sp,AD}X + P_{sp,BD}Y + P_{sp,CD}(1-X-Y) \quad \textit{Eq. 2}$$

Thus, the spontaneous polarization in $Al_xGa_{1-x}N$ and $Al_xIn_{1-x}N$ ternary alloys, is obtained as the following:

$$P_{sp,Al_XGa_{1-X}N}(X) = -0.052X - 0.029 \ C.m^{-2} \quad \textit{Eq. 3}$$

$$P_{sp,Al_XIn_{1-X}N}(X) = -0.049X - 0.032 \ C.m^{-2} \quad \textit{Eq. 4}$$

Figure 4a shows a visualization of equations number 3 and 4, and we note that the spontaneous polarization of $Al_xGa_{1-x}N$ and $Al_xIn_{1-x}N$ ternary alloys is always higher than that for a pure GaN layer.

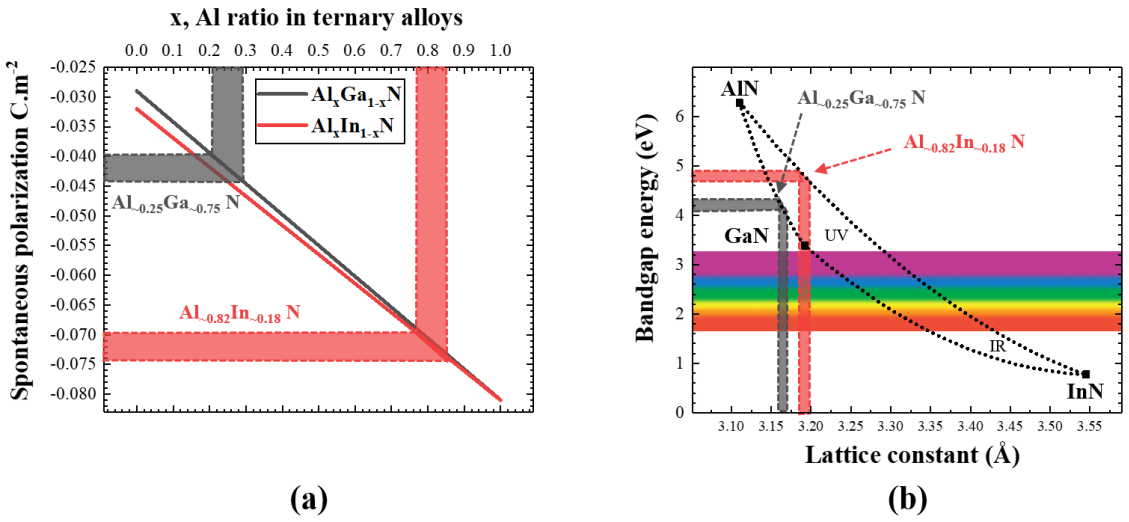

Figure 4: a) Spontaneous polarization as a function of Al ratio in wurtzite III-N ternary alloys. b) Evolution of the band gap energy of III-N alloys depending on the lattice parameter.

I.3.4 Piezoelectric polarization

Another component adding to the total polarization within the III-N heterostructure is the piezoelectric polarization (P_{pe}). In hetero-structures, such as InGaN, AlGaN or InAlN on GaN, the piezoelectric polarization arises from the strain associated with the lattice mismatch between the top layer and the buffer layer which will form the channel. Strain can be either tensile or compressive, as can be seen from Figure 5a and b.

When the top layer has a smaller in-plane lattice parameter than the buffer layer, the strain is tensile; and vice versa for the compressive strain. III-N binaries lattice parameter values are shown in Table 2.

Lattice parameter values, for ternary $A_xB_{1-x}N$ alloys such as InAlN, AlGaN and InGaN, can be calculated as follows:

$$a_{A_XB_{1-X}N}(X) = a_{AN}X + (1-X)a_{BN} \qquad \textit{Eq. 5}$$

$$c_{A_XB_{1-X}N}(X) = c_{AN}X + (1-X)c_{BN} \qquad \textit{Eq. 6}$$

We note that AlGaN barriers, when grown under critical thickness, will always be in tensile strain state on GaN buffers. However, this is not the case for InAlN alloys, where the strain state can go from tensile when In% is lower than ~18%, to compressive when In% is higher than ~18%, as shown in Figure 5c and d respectively, and almost null when In% is around 18%, means when InAlN is lattice matched to GaN buffer.

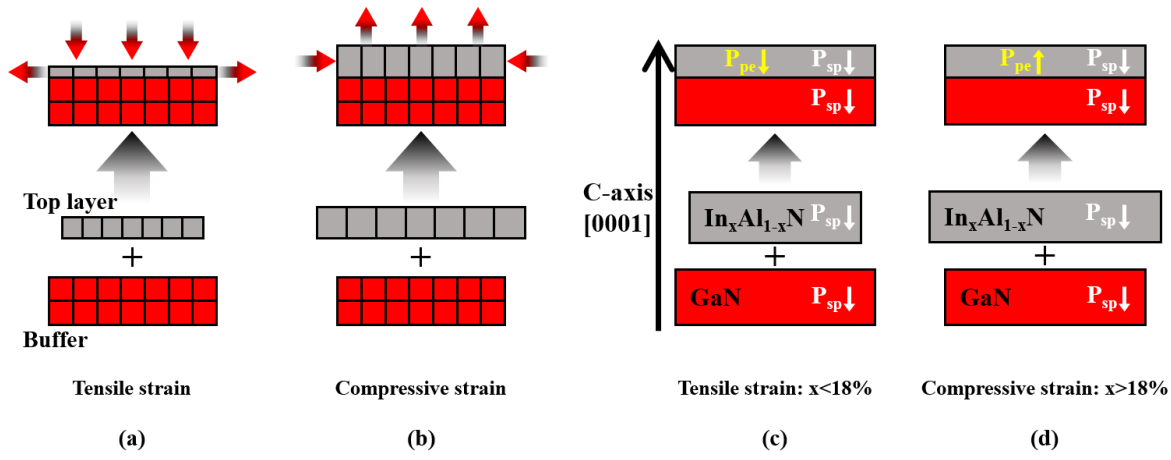

Figure 5: Illustration of a) tensile and b) compressive strains. c) InAlN/GaN strained heterostructure and d) compressed heterostructure.

This piezoelectric polarization is defined in the three dimensional Cartesian coordinate system as a function of the piezoelectric constants e_{ij} and the strain field components ε_j:

$$P_{pe} = \sum e_{ij}\varepsilon_j \qquad \text{Eq. } 7$$

Due to crystal symmetry in wurtzite crystal structure, there are only three independent piezoelectric constants e_{15}, e_{31}, and e_{33}. Values are summarized in Table 2.

Thus, we have:

$$P_{pe} = \begin{pmatrix} 0 & 0 & 0 & 0 & e_{15} & 0 \\ 0 & 0 & 0 & e_{15} & 0 & 0 \\ e_{31} & e_{31} & e_{33} & 0 & 0 & 0 \end{pmatrix} * \begin{pmatrix} \varepsilon_1 \\ \varepsilon_2 \\ \varepsilon_3 \\ \varepsilon_4 \\ \varepsilon_5 \\ \varepsilon_6 \end{pmatrix} \qquad \textit{Eq. 8}$$

We note that the deformation along the C-axis is $\varepsilon_z = (c\text{-}c_0)/c_0$, and the deformation in the perpendicular plane to the C-axis is $\varepsilon_x = \varepsilon_y = (a\text{-}a_0)/a_0$, where c_0 and a_0 are respectively the in-plane and out-of-plane lattice parameters of a fully relaxed bulk material.

According to Hooke's law, i.e. for elastic deformation that is to say for small deformation, the stress σ_{ij} is related to the strain ε *by:*

$$\sigma_i = \sum C_{ij}\varepsilon_j \qquad \textit{Eq. 9}$$

Where C_{ij} is the elastic constant or stiffness tensor, which contains five independent coefficients. Values are summarized in Table 2.

Due to the hexagonal symmetry presented in the wurtzite crystal structure we have:

$$C_{ij} = \begin{pmatrix} C_{11} & C_{12} & C_{13} & 0 & 0 & 0 \\ C_{12} & C_{11} & C_{13} & 0 & 0 & 0 \\ C_{13} & C_{13} & C_{33} & 0 & 0 & 0 \\ 0 & 0 & 0 & C_{44} & 0 & 0 \\ 0 & 0 & 0 & 0 & C_{44} & 0 \\ 0 & 0 & 0 & 0 & 0 & \left(\frac{1}{2}(C_{11} - C_{12})\right) \end{pmatrix} \qquad \textit{Eq. 10}$$

Now, as we are growing in the C-axis direction, there is no stress along this axis, and the in-plane stress is uniform ($\sigma_x = \sigma_y$). Thus, in this biaxial stress configuration, Eq. 9 becomes:

$$\varepsilon_x = \varepsilon_y \; ; \; \varepsilon_z = -2\left(\frac{C_{13}}{C_{33}}\right)\varepsilon_x \qquad \textit{Eq. 11}$$

Combining Eq. 8 and Eq. 11, with the fact that $\varepsilon_z = (c-c_0)/c$ and $\varepsilon_x = \varepsilon_y = (a-a_0)/a_0$ we find that the strain-induced piezoelectric polarization magnitude value along the C-axis direction is as follows:

$$P_{pe} = 2\frac{a-a_0}{a_0}\left(e_{31} - e_{33}\left(\frac{C_{13}}{C_{33}}\right)\right) \qquad \textit{Eq. 12}$$

We note that, spontaneous and piezoelectric polarizations are in the same direction as each other for tensile strain and in opposite directions for compressive strain, as can be seen from Figure 5c and d.

Wurtzite	**AlN**	**GaN**	**InN**
Eg (eV)	6.2	3.39	0.7
a (Å)	3.111	3.189	3.545
c (Å)	4.979	5.178	5.703
P_{sp} (C.m^{-2})	-0.081	-0.029	-0.032
***e*$_{15}$ (C.m^{-2})**	-0.48	-0.30	
***e*$_{31}$ (C.m^{-2})**	-0.58	-0.33	-0.57
***e*$_{33}$ (C.m^{-2})**	1.55	0.65	0.97
***C*$_{11}$ (GPa)**	410	390	190
***C*$_{12}$ (GPa)**	149	145	104
***C*$_{13}$ (GPa)**	99	106	121
***C*$_{33}$ (GPa)**	389	398	182
***C*$_{44}$ (GPa)**	125	105	10

Table 2: Different properties of III-Nitride binaries wurtzite crystal: bandgap energy and lattice parameter at 300K, spontaneous, piezoelectric, and elastic parameters. [1, 2, 3, 25, 26, 27, 28, 29, 30, 31] [32]

Typically, AlGaN alloys with Al% around 25%, are used as barriers for GaN-based HEMT heterostructures. However, when growing AlGaN with Al% higher than 25-30%, which is desirable for increased spontaneous polarization, a larger lattice mismatch between AlGaN barrier and GaN buffer occurs, as can be seen from Figure 4b, and this will increase the risk of strain relaxation by cracking [33]. This relaxation results in degraded AlGaN barrier quality, leading to reduced carrier mobility. This relaxation can also raise concerns about the reliability of AlGaN/GaN devices [34].

As an alternative to AlGaN barriers, the implementation of InAlN barriers with In% around 18%, allows the strain to be controlled in the InAlN/GaN heterostructure, as InAlN barrier lattice parameter will be perfectly matched to that of GaN buffer layer, this can be seen from Figure 4b. Also, we can benefit from the stronger spontaneous polarization shown in Figure 4a. [35]

The realization of a strain-free heterostructures with InAlN/GaN heterostructure is actually an excellent choice since it will lead to a very low Rsheet value [36]. This is the main reason why in this thesis we are interested in growing such material.

I.3.5 Polarization induced charge and two-dimensional electron gas

The polarization can increase or decrease within a bilayer, followed by the generation of a fixed two-dimensional polarization charge density at the abrupt interface of the barrier/channel heterostructure. It is defined as follows: [37]

$$\sigma_{interface} = P(buffer) - P(barrier) = \{P_{sp}(buffer)+P_{pe}(buffer)\} - \{P_{sp}(barrier)+P_{pe}(barrier)\} \quad \textit{Eq. 13}$$

In addition, we have the following two-dimensional polarization charge density on the top layer surface:

$$\sigma_{Barrier\ surface} = P(barrier) = P_{sp}(barrier) + P_{pe}(barrier)\} \quad \textit{Eq. 14}$$

Respectively, the generated polarization induced sheet charge is denoted as σ/e, where e = 1.602x10^{-19} C is the elementary charge of an electron, and σ is the charge density.

In the case of a positive polarization induced bound charge density, e.g. $+\sigma/e$, free electrons will tend to compensate the charge, resulting in the formation of the two dimensional electron gas (2DEG) at the abrupt top/bottom interface, as shown in Figure 6a. By analogy, a negative sheet charge density, ($-\sigma/e$), can generate a two-dimensional hole gas (2DHG) if the valence band edge crosses the Fermi energy close to the interface. [38]

For AlGaN and InAlN (with Al% > 70%) barriers grown on a Ga-face GaN channel layer, the total polarization induced sheet charge is found to be positive, as can be seen from

Figure 6 b [38]. This leads as mentioned to the formation of a 2DEG at the barrier/channel interface. We note that, with a lattice matched $In_{0.18}Al_{0.82}N$ layer to GaN, sheet charge density is almost three times higher than for the conventionally grown $Al_{0.25}Ga_{0.75}N$ barriers on GaN channels, from which comes the interest of working with InAlN as barriers.

We should note that the 2DEG in III-N heterostructures is realized without any need of a modulation-doped barrier, unlike the 2DEG created in GaAs-based systems where doping is necessary. Yet, the doping in III-N systems can also be performed to enhance carrier density by adjusting the position of the Fermi level.

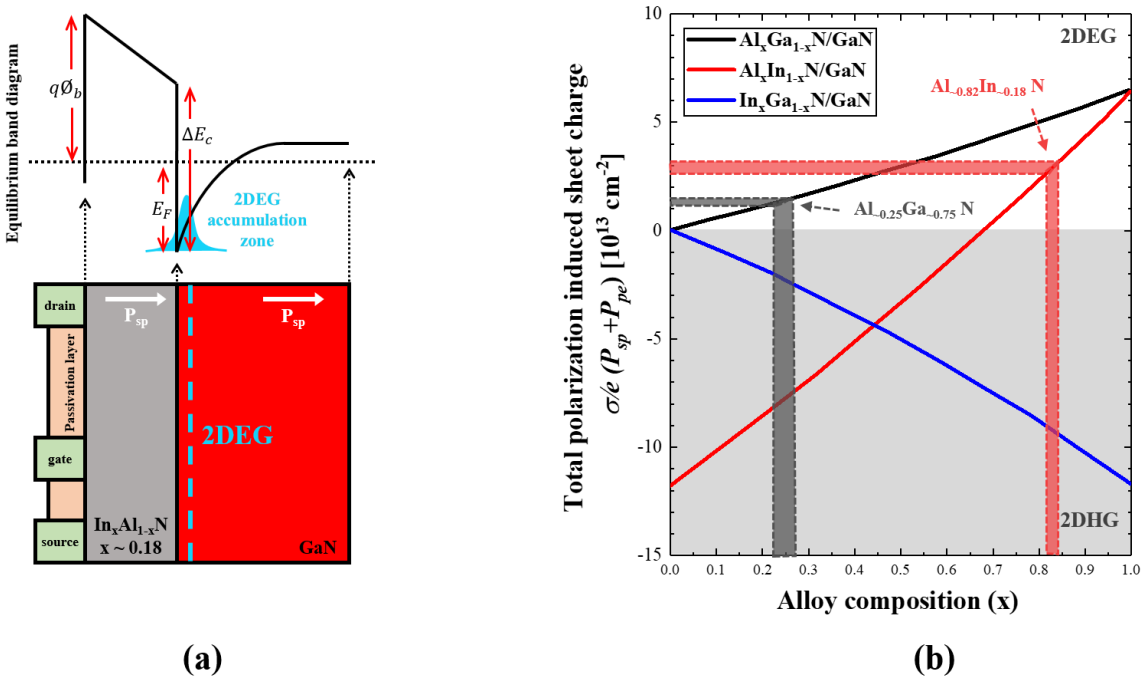

Figure 6: a) III-N HEMT heterostructure,with the equilibrium band diagram (V = 0 Volts) of the InAlN/GaN heterostructure above b) total polarization induced sheet charge σ/e (Psp+Ppe) bound at the interfaces of Ga-face AlGaN/GaN, AlInN/GaN and InGaN/GaN heterostructures, versus alloy composition of the top layer [38].

Following this quick theoretical explanation of the polarization-induced charge, now we can predict the sheet carrier concentration of the 2DEG and their dependence on alloy composition for AlGaN/GaN, and InAlN/ GaN (with Al% > 71%) heterostructures.

The sheet electron concentration, $n_s(x)$, for undoped pseudomorphic Ga-face AlGaN/GaN or InAlN/GaN HEMT structures, can be approximated by taking advantage of

the total bound sheet charge $\sigma_{interface}$ calculated above in Eq. 13, and the following equation: [38]

$$n_s = \frac{\sigma_{interface}}{q} - \left[\frac{\varepsilon_0 \varepsilon_r(x)}{t_{barrier} q^2}\right] [q\emptyset_b(x) + E_F(x) - \Delta E_c] \qquad \textit{Eq. 15}$$

Where $t_{barrier}$ is the thickness and ε_r is the dielectric constant of the barrier layer, q is the elementary charge of the electron. $\emptyset_b$ is the height of the Schottky barrier, $E_F(x)$ is the position of the Fermi level at the heterointerface with respect to its position in the GaN layer and ΔE_c is the discontinuity of the conduction band at the barrier / GaN interface.

Another intrinsic property of the 2DEG is the electron mobility, μ_e. As we have seen, the sheet electron concentration in the 2D gas depends mainly on the thickness of the barrier and its alloy composition. In fact, the mobility of electrons depends on numerous elastic and inelastic scattering mechanisms of the carriers on the defects of the structure, such as barrier/channel interface roughness, ionized impurities, threading dislocations, alloy disorder, acoustic and optic phonons. These mechanisms are more or less dominant depending on the temperature and the alloy composition. [39]

I.3.6 Specificities of the III-N elements for electronic applications

By comparing the basic properties of semiconductor materials, we can see the fields of application and the performances accessible by certain alloys. As can be seen in Figure 7, semiconductors differ essentially in the nature and energy of their bandgap. We find among them direct gap materials such as GaAs, InP and III-N alloys such as AlN, GaN and InN. The advantage of this type of bandgap is that the transitions of carriers (electrons or holes) between the energy levels is direct. In this case, radiative recombination or interband absorption is easily generated. These properties are essential in optoelectronic applications based on III-V semiconductors, in particular for the realization of semiconductor lasers.

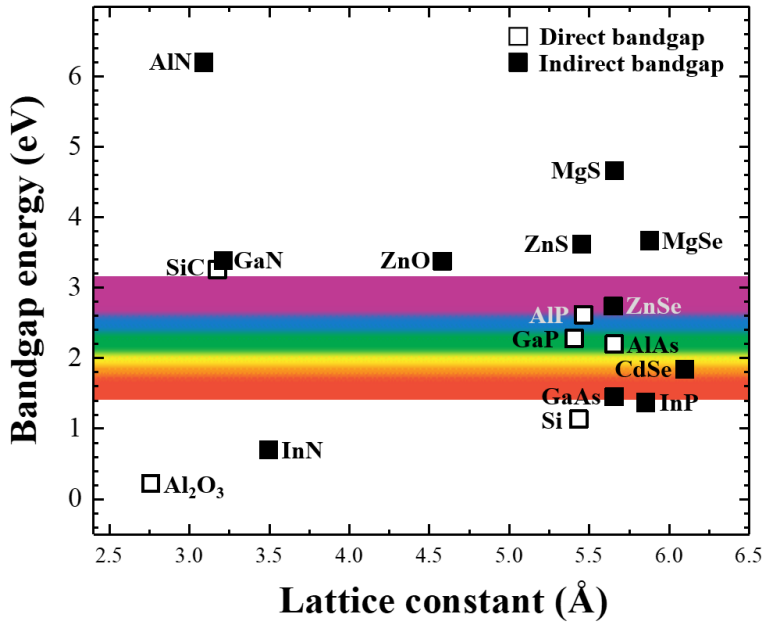

Figure 7: Bandgap energy of different semiconductors depending on the lattice parameter at 300 K.

The energy of the bandgap also plays an important role according to the intended application. Large gap semiconductors can achieve high breakdown voltages and high operating temperatures, making them suitable for use in high voltage supply devices. SiC and GaN have a gap two to three times larger than conventional semiconductors such as Si, GaAs or InP and therefore a breakdown field typically an order of magnitude greater.

Table 3 shows the fundamental properties at 300K of the most important semiconductors for the performance of electronic devices.

Properties	**AlN**	**GaN**	**InN**	**SiC**	**GaAs**	**InP**	**Si**
Bandgap (eV)	6.2	3.39	0.7	3.2	1.4	1.3	1.1
Breakdown field (MV/cm)	8.4	3.3	1.2	3.5	0.4	0.5	0.3
Saturation velocity (10^7cm/s)	2.1	2.5	1.8	2	1.2	1	1
Electron mobility (cm^2/V.s)	135	990	3.6	650	8500	5400	1500
Relative permittivity (ε_r)	9.14	9.5	15.3	10	11.5	12.5	11.8
Thermal conductivity (W/cm.K)	2.85	1.3	0.45	4.5	0.5	0.7	1.5

Table 3: Properties of different semiconductor materials at 300K. [40, 41, 42, 43]

In general, in order to achieve high current and high frequency operation, high electron mobility (μ) and high electron saturation velocity (v_{sat}) are required. In GaAs, the electron mobility is very high, around 8500 cm^2/ (V.s). This is the main reason that field effect transistors (FETs) made with this material have excellent high frequency performance. A major drawback in the fabrication of GaN and SiC-based transistors is the relatively low electron mobility values, which is 990 cm^2/ (V.s) for GaN bulk and 650 cm^2/ (V.s) for SiC. However, in GaN based HEMT heterostructures, the 2DEG mobility is high compared to the electron mobility in GaN bulk [44], up to 2000 cm^2/Vs. This is mainly due to the difference in the carrier diffusion mechanisms between both, HEMTs and bulk. Diffusion mechanisms such as: coulomb collisions, collisions with the crystal lattice, collisions on the surface roughness [45]. In fact, in a HEMT heterostructures, the insertion of AlN spacer reduces alloy disorder at the heterointerface and prevents the diffusion of carriers from the channel to the barrier, resulting in improved carriers mobility. However, these carriers mobility values are sufficient for transistors specifically designed for high power operation.

Another important parameter of semiconductor material is the thermal conductivity (κ). This parameter defines the capacity of heat dissipation by a component. Poor thermal conductivity leads to degraded operation of the device at high temperatures. In general, conventional semiconductors are poor thermal conductors, in particular GaAs and InP. Conversely, AlN, SiC and especially diamond are excellent thermal conductors. GaN is comparable with Si with both having intermediate values.

For a better comparison of the performances of the various semiconductor materials such as GaN, GaAs, Si, and 4H-SiC, several figures of merit have been proposed, as shown in Table 4. These figures combine the main properties of semiconductor materials to classify them according to their performance in power, frequency, and thermal limitation.

The Johnson's figure of merit (JFOM) is a measure of suitability of a semiconductor material for high frequency power transistor applications and requirements. It is the product of the charge carrier saturation velocity in the material and the electric breakdown field under the same conditions. JFOM is given by $(E_b.v_s/2\pi)^2$, where E_b is the semiconductor's electric breakdown field and v_s is the electron saturation velocity. [46]

Keyes's figure of merit (KFOM), considering thermal limitation, provides a thermal limitation to the switching behavior of transistors used in integrated circuits. It is given by $k(c.v_s/4\pi.\varepsilon_s)^{1/2}$, where k is the material thermal conductivity, c is light velocity in vacuum, and ε_s is the material dielectric constant. [47]

Baliga's figure of merit (BFOM) for power switching, is giving by $(\varepsilon_s.\mu.E_g^3)$. BOFM defines material parameters to minimize the conduction loss in low-frequency unipolar transistors. Here, μ is the mobility and E_g is the bandgap of the semiconductor. [48]

Baliga also derived a high-frequency figure of merit (BHFFOM) for unipolar switches, giving by $\mu.E_b^2.(V_G/4(V_B)^3)^{1/2}$. Here V_G is the gate drive voltage and V_B is the breakdown voltage. BHFFOM demonstrates the power loss reduction that can be achieved by a given material. [49]

	Si	**GaAs**	**4H-SiC**	**GaN**
Johnson's figure of merit JFOM ($E_b.\ v_s/2\pi)^2$	1	11	410	790
Keyes's figure of merit KFOM ($k(c.v_s/4\pi.\varepsilon_s)^{1/2}$)	1	0.45	5.1	1.8
Baliga's figure of merit BFOM ($\varepsilon_s.\mu.E_g^3$)	1	28	290	910
Baliga's figure of merit BHFFOM ($\mu.E_b^2.(V_G/4(V_B)^3)^{1/2}$)	1	16	34	100

Table 4: Comparison of normalized figures of merit of various semiconductors. [50] [46] [47] [48] [49]

As can be seen from Table 4, especially in figures of merit of JFOM, BFOM and BHFFOM, it is very clear that GaN is a one of the top choices semiconductors material for high frequency and high power applications compared to the conventional Si, GaAs and SiC materials.

I.4 GaN on Si based electronic applications

Nitride semiconductors have two main fields of application: optoelectronics and high power/ high frequency electronics. For optoelectronics, nitrides have a direct band gap, as already shown in Figure 7, which make them suitable for the realization of optical devices covering a wide range of applications from the near infrared through visible to deep ultraviolet emission and detection. We will not dwell upon this subject since our main center of interest concerns electronic applications.

Power electronics is the second and the main promising market for GaN-based technologies after LEDs. In particular, GaN is widely used in high frequency devices, and is being developed to replace silicon for high power devices. A comparison of key properties of GaN, GaAs, SiC and silicon is shown in Figure 8. Silicon based devices are limited by an operation frequency of less than 3.5 GHz, as can be seen from Figure 9. In this context, GaAs-based components represented a good alternative to replace silicon technology thanks to their frequency performance. Nevertheless, GaAs technology is penalized in power density because of its weak breakdown field.

Therefore, the development of material-based transistors combining a large gap, a strong breakdown field and a high density of electrons was needed. GaN has a high breakdown field with good thermal conductivity together with the possibility of achieving high mobilities and electronic densities.

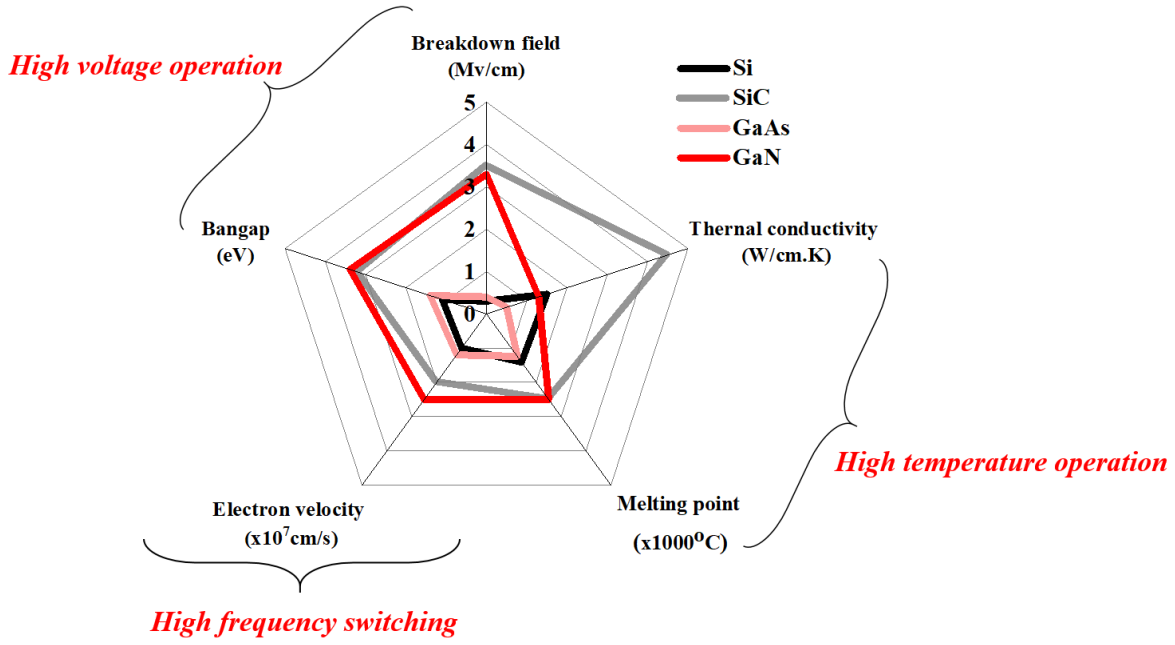

Figure 8: Si, SiC, GaAs, GaN capability comparison for electronic applications. [data from Table 3 and Table 1]

Following the early growth of GaN on Si layers of good crystalline quality, the growth of the first high electron mobility transistors (HEMTs) on silicon was demonstrated in the early 2000s [51] [52]. Here again, the main problems come from defects and cracks in the material inducing current leakage and limiting the performance of devices. Techniques for

stress management and for reducing the density of defects were developed in this area in order to have a better material quality and lower strain, as previously discussed.

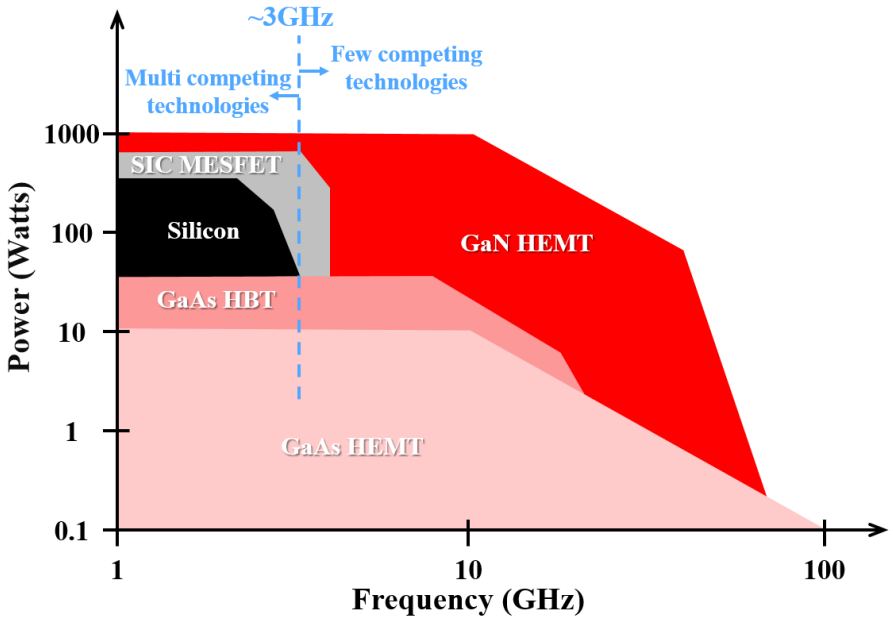

Figure 9: Frequency-accessible power ranges for different semiconductor materials reproduced from [53].

Currently, Infineon, Epigan, Macom, ST Mircoelectronics and many other companies are commercializing GaN on Si based devices for high power and high frequency electronics, as they cover a wide range of applications requirements, see Figure 9. Similarly, in 2014 in Grenoble, a young startup, Exagan, started commercializing in this field based on the expertise of CEA-LETI and Soitec.

I.4.1 InAlN/GaN HEMT

Following more than 25 years of development, AlGaN/GaN HEMTs have become the most technologically mature form of GaN-based HEMTs. However, as mentioned in the previous sections, the total strain formed in such heterostructure can create cracks within the material structure, which may limit the device reliability and performance. Another device limitation imposed on AlGaN/GaN based HEMT structures for high frequency performance is the barrier thickness. There is a requirement for thinner top barriers to maintain a favorable channel aspect ratio so as to minimize short-channel effects and enable higher cutoff frequencies. In fact, when AlGaN barrier thickness is below 15 nm, the two-dimensional

electron gas (2DEG) in such heterostructure is subjected to surface depletion effects [54]. Some researchers tried to remedy this problem by using AlN thin top barriers, which can boost sheet densities within the channel [55]. However, the impact when growing such structure on the strain-related device degradation modes was not clear.

As an alternative to AlGaN and AlN barriers, in 2001, Kuzmík suggested the growth of InAlN material with 18% indium, a lattice matched barrier for GaN-based HEMTs [56]. InAlN material offers a solution to some of the strain-related device reliability concerns associated with conventional lattice-mismatched AlGaN/GaN heterostructures [57]. In addition, surface depletion effects should be far weaker for the InAlN/GaN compared to AlGaN/GaN [56]. This enables the growth of thin barriers for GaN-HEMTs, and then respecting the excellent channel aspect ratio, down to very short gate lengths. In 2008, Medjdoub et al. demonstrated the feasibility of growing an ultrathin 3 nm InAlN barrier on GaN [58] . Later, the same team has also shown that InAlN/GaN can be stable up to 1000°C [59]. Finally yet importantly, InAlN based HEMTs are predicted to have high transconductance values and current densities [56].

I.4.2 State of the art: InAlN/GaN HEMTs Rsheet, n_s, µ

One of the most important parameters that describes the electrical performance of a HEMT device is the 2DEG sheet resistance. It is the combination of the 2DEG carrier density n_s and mobility μ. The lower the sheet resistance value, the better the device high frequency performance. Many studies have been performed to improve HEMTs performance by reducing the sheet resistance value, such as working on a good passivation layer, the optimization of InAlN barrier quality, thickness and composition, the optimization of AlN spacer quality and thickness, and GaN surface quality and roughness, etc.

In this section, we present the best sheet resistance results that we found after the first developments of InAlN/GaN HEMT, starting from 2004 up to 2019. As discussed before, InAlN/GaN HEMTs are typically grown on foreign substrates, thus we mainly considered this in our bibliographic research. As shown in Figure 10, the best sheet resistance results for InAlN/GaN HEMTs are 163 ohms/□ [60], for Al_2O_3 substrate; 185 ohms/□ [61], for SiC substrate; 167 ohms/□ [62], for Si substrate; and 145 ohms/□ [63], for GaN Free Standing

substrate. Also, for comparison purpose, in this figure we drew a dashed line to present the typical Rsheet values found for AlGaN/GaN HEMTs, which is around 300 Ohms/sq.

We note that despite the variety of substrates used and the different dislocation density for each ($<10^9$ or $<10^{10}$), we are getting similar Rsheet results, means that the electrical performance has a low sensitivity to dislocations at room temperature.

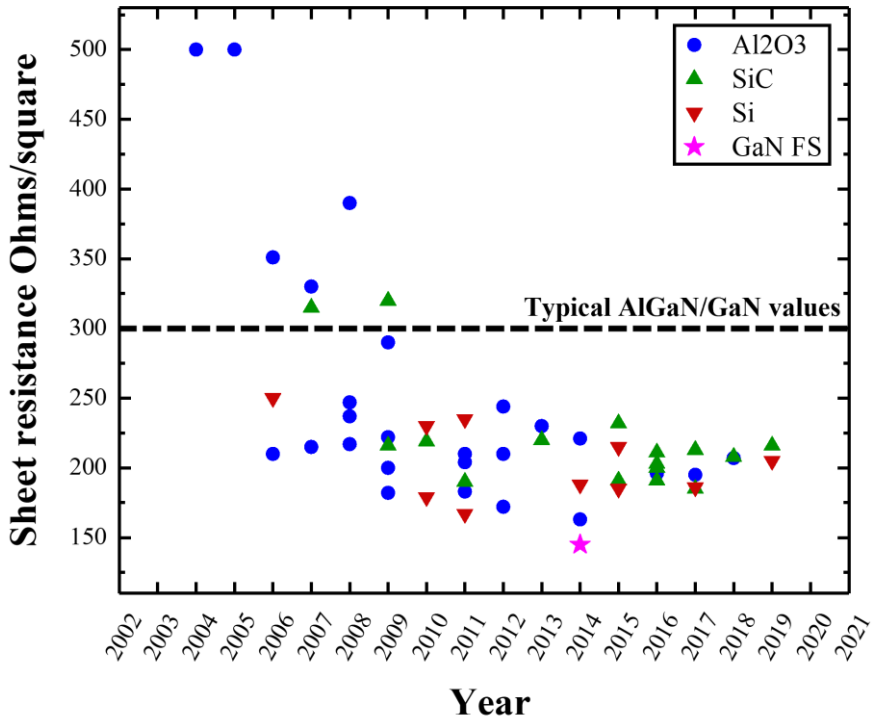

Figure 10: InAlN/GaN sheet resistance values for different substrates in function of years of development, and black dashed line present typical AlGaN/ GaN Rsheet values. [64, 65, 66, 67, 68, 69, 70, 71, 72, 73] [74, 75, 76, 77, 78, 79, 80, 81, 82, 83] [84, 85, 86, 87, 88, 62, 89, 90, 91, 92] [93, 94, 95, 63, 96, 60, 97, 98, 99, 100] [101, 102, 103, 104, 105, 106, 61, 107, 108, 109] [110, 111, 112]

Along these lines, in this PhD work, our first aim was to understand and optimize the epitaxial processes to try to achieve the best sheet resistance performance of InAlN/GaN HEMT when grown on Si. We will present our results in the following chapters.

I.5 Objective of this research

It is clear that InAlN, as an alternative barrier for GaN based HEMTs, is still less mature compared to AlGaN, yet it is expected to be a strong competitor. On the other hand, growing high quality InAlN/GaN HEMTs is in general more difficult than growing its

AlGaN/GaN counterparts. This issue comes from the strong immiscibility effect between InN and AlN, resulting from the big difference in the lattice parameter values of both, see Table 2. The immiscibility effect tends to induce alloy fluctuation and rough interfaces near the 2DEG channel which can deteriorate electron mobility. Another challenge is the big difference in growth parameters of its two binaries InN and AlN. The ideal growth temperature of InN is around 600°C, which is very low compared to the growth temperature of AlN of around 1100°C.

Metal-Organic Vapor Phase Epitaxy (MOVPE) growth of pure InAlN faces another problem: the non-intentional incorporation of Ga into the InAlN barrier. This problem comes from the Close Coupled Showerhead (CCS) chamber architecture. [113, 114, 115, 116, 117]

The gallium contamination problem in CCS reactors is a serious obstacle for the growth of InAlN pure materials. It affects the control and the reproducibility of the desired growth recipes, and results in reduced indium incorporation [118] and reduced barrier polarization as pictured in Figure 11. Besides affecting the structural and electrical properties of InAlN epilayers.

In this work, we will focus on understanding and quantifying gallium contamination problem in such chamber architecture on InAlN and, by extension, on InGaN MOVPE growth. Later we will bring some chamber architecture related solutions that help in remedying this problem, and eventually avoid it.

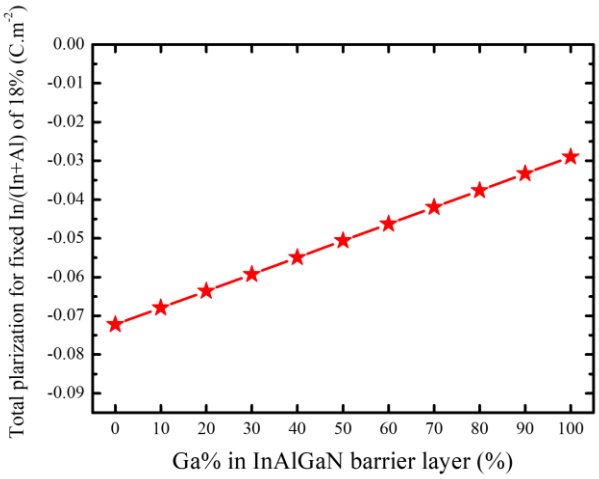

Figure 11: Total polarization in InAlGaN barriers for increased Ga% and fixed In/(In+Al) ratio of 18%.

Chapter II: III-N MOVPE growth and characterization methods

II.1 Introduction

In this second chapter of the manuscript, we will firstly examine the different growth techniques used for the growth of semiconductor materials, with a focus on MOVPE, the growth technique which we used for the growth of III-N samples. Later, we will detail the AIXTRON growth equipment and its different parts, which are critical for the good control of the MOVPE growth epitaxy of III-N layers. In the third part, we will discuss the different physical and chemical characterizations techniques that were performed on our samples.

II.2 The different epitaxial growth techniques of GaN

The word "epitaxy" is originally a Greek word, where "epi" means above and "taxy" means order. It was proposed in 1928 by the French mineralogist Royer to designate the regular juxtaposition of two crystalline species.

Currently, the term epitaxy is used for any monocrystalline layer deposited whose orientation is fixed by a substrate. If this substrate is of the same nature as the deposit layer, we speak of homoepitaxy; if it is of a different nature, the term of heteroepitaxy is used.

Several epitaxial techniques exist for the growth of semiconductor materials. The main techniques used for the epitaxial growth of III-N semiconductors are Metal Organic Vapor Phase Epitaxy (MOVPE), Molecular Beam Epitaxy (MBE), and Hydride Vapor Phase Epitaxy (HVPE). Each technique has its strengths and weaknesses, summarized in Table 5.

Properties	**MBE**	**MOVPE**	**HVPE**
Growth temperature (°C)	500-900	700-1100	900-1100
Growth pressure (mbar)	10^{-8}	50-800	500-1000
Growth rate (µm/h)	0.1 to 1	0.1 to 10	10 to 300
Strengths	• Good control of interfaces, thicknesses and compositions • Detailed in-situ growth monitoring	• Good control of interfaces, thicknesses and compositions • Most flexible • Rapid growth • Growth possible on several substrates and / or large substrates	• Very rapid growth of thick layers
Weaknesses	• Ultra-high vacuum environment • Low growth rate • Limited size of growth chambers	• Less good in situ monitoring than the MBE	• Poor control of interfaces • Complex process/reactor

Table 5: Comparative of epitaxial growth techniques of III-N semiconductors. [119] [120]

II.3 MOVPE growth technique

In this work, only MOVPE was used, and although as discussed in Table 5 this technique has many advantages, the existence of a large number of parameters that can be controlled during the epitaxial growth can make it difficult to optimize. These parameters lead to great complexity, which in turn can bring problems with reproducibility and understanding. For instance, the reactor pressure, temperature, the flow of injected gas, the bubblers temperature and pressure, etc. all these parameters influence the layer growth rate, their crystalline quality and surface, the rate of incorporation of certain component elements, the generation of parasitic reactions in the growth chamber, the homogeneity of the layers, and reproducibility. However, with modern chambers, and chamber preparation, these difficulties have mainly been overcome, although some details are still being worked on, in particular for growth of InAlN in showerhead reactors, as this PhD will discuss.

II.3.1 MOVPE basics

MOVPE epitaxial growth occurs through gas delivery of group III and V elements on a substrate. The precursors used for group III elements combine an organic compound (C-H) and a metal such as gallium, aluminum, and indium. In this work, we have used tri-methylindium (TMIn), tri-methylaluminum (TMAl), and tri-methylgallium (TMGa) as precursors for indium, aluminum and gallium respectively. The precursor used for nitrogen is ammonia (NH_3).

In MOVPE epitaxy, our aim is to grow a single crystal of a specific material combining one or more elements. This is started from a monocrystalline mechanical support (the substrate) and the atoms of the material we want to grow will be able to rely on this perfectly oriented structure to form a material of the given crystalline symmetry.

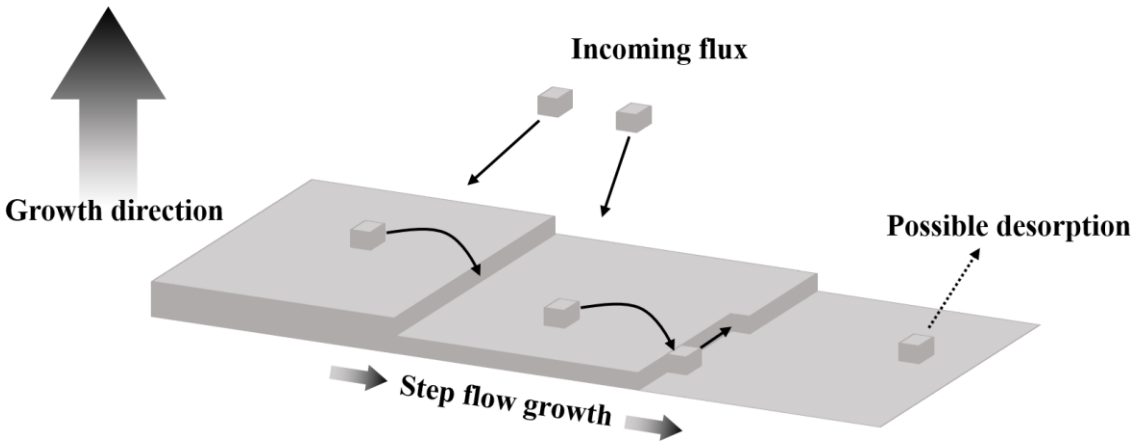

Figure 12: Simple illustration of the epitaxy process.

Figure 12 shows a simple illustration of the epitaxy process. Small cubes represent the chemical elements that are sent to the growth chamber during the epitaxial growth. In this model, each cube face presents a chemical bond. It is clear that the incorporation of cubes, e.g. elements, is more favorable at an angle where at least three other chemical bond are available than on the surface where the cube is attached by only one chemical bond. This leads to the 2-dimensional step flow growth shown in the figure. We note that a cube at the surface is more easily desorbed than one already integrated into it.

The single crystal growth during the MOVPE process takes place at the interface between the gas phase (the reactants) and the substrate. In general, gases are introduced into the growth chamber in a carefully controlled manner. Then, close to the substrate, gas molecules undergo a pyrolysis process, e.g. a thermal decomposition, before they diffuse on the substrate surface. In Figure 13, we show the physical and the chemical processes that take place during epitaxy, for the example of TMGa and NH_3 precursors leading to the deposition of III-N compound on the wafer surface. This figure is simplified and does not take into account the complex chemical reactions that occur in the gas phase and on the wafer surface.

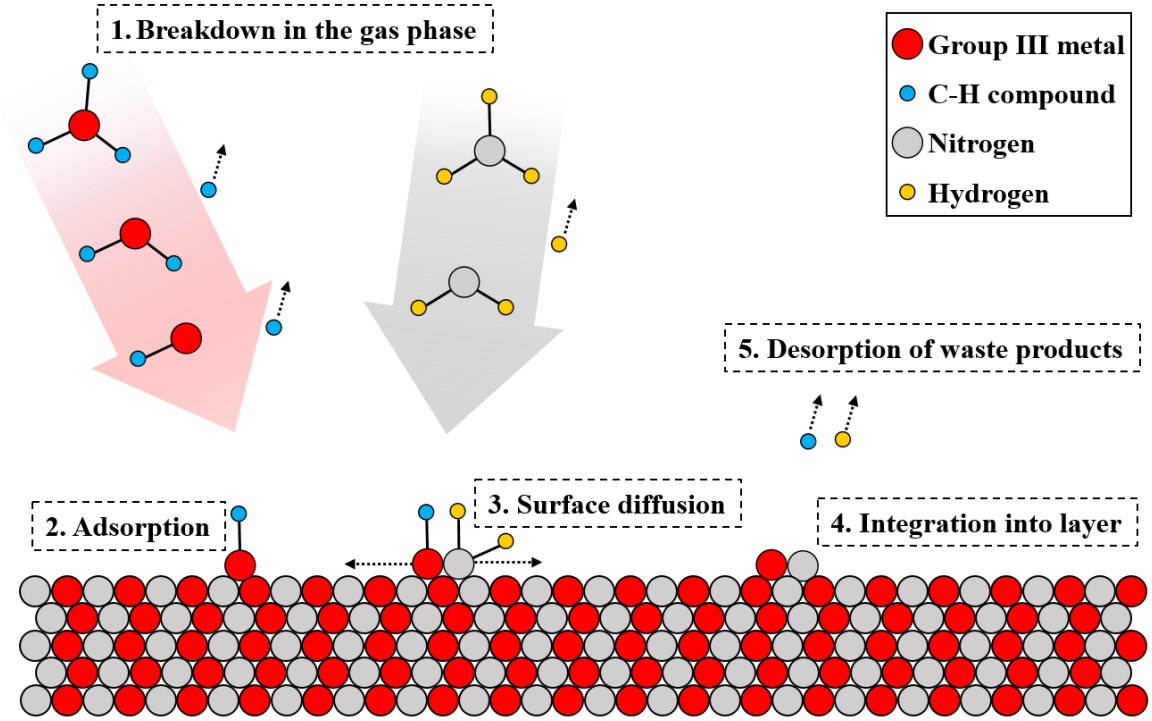

Figure 13: MOVPE chemical processes in parallel with physical processes.

II.3.2 MOVPE growth analysis

MOVPE growth was initiated in the late 1960s. It enjoyed a growing success during the years 1980-1990. Due to its extreme complexity, the total MOVPE process has often been treated as a "black box". This means that the growth of a desired material can be attained only by turning machine knobs in a systematic fashion, with device performance the typical measure of success. [120]

Although there have been a great many studies to understand MOVPE growth, starting with examination of InP and GaAs growth in the 1980s, it would be inaccurate to claim that all aspects of the MOVPE process are perfectly understood. There are still lots of detailed interactions which are yet to be fully mastered. However, thanks to the introduction of optical techniques for the in-situ monitoring and control of the MOVPE growth process, and advanced characterization of layers, there is generally a good control of the final epitaxial growth.

The ability to control the MOVPE growth process for III-V materials for advanced electronic and optoelectronic devices requires a detailed understanding of the processes occurring during growth.

In general, there are several important phenomena / concepts involved in the understanding of the MOVPE growth process. These concepts are subdivided as follows:

- Thermodynamics
- Kinetics
- Hydrodynamics and mass transport

For the sake of simplicity, we will use the MOVPE growth of GaAs using tri-methylgallium (TMGa) and Arsine (AsH_3) as an example to clarify these three concepts. This is a system which has been studied in great detail, and which has few pre-reactions in the gas phase which can complicate the analysis.

A collection of typical results on growth efficiency (growth rate/TMGa molar flow rate) of GaAs versus reciprocal temperature allows an extraction of the different growth regimes, as shown in Figure 14.

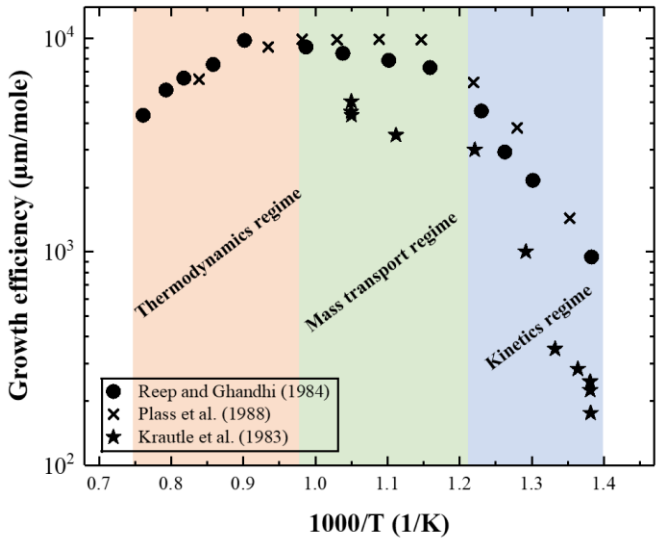

Figure 14: Growth efficiency of GaAs as a function of the reciprocal growth temperature. [120] [121] [122] [123]

At high growth temperatures, above 750°C, we are considered to be working under thermodynamically limited regime, in which there is a decrease in growth rate, due to factors such as desorption / evaporation of material. [120] [124]

Conversely, if the temperature is lower than 550°C, we are considered to be working under another regime, the kinetically limited growth regime. GaAs growth rate also decreases at this stage, but this time is due to limitations of the speed of certain reactions, such as the lower MO molecules break down rate on the material surface. This regime gives a strong dependence of the growth rate on the growth temperature [120]. In particular, the growth rate increases with temperature in the following form:

$$V_{growth} \propto exp\frac{-\Delta E}{RT} \qquad Eq.\ 16$$

Where ΔE is the Arrhenius activation energy of the MO molecule decomposition, R is the ideal gas constant and T is the temperature.

We note that, in this growth regime, wafer growth orientation has also an influence on the GaAs growth rate.

Lastly, when the growth temperature is between 550°C and 750°C we are considered to be working in mass transport regime. In this regime, GaAs growth rate is relatively constant, despite the variation in temperature and we are dependent only on mass transport. The gas molecules breakdown quickly on the substrate surface, and the growth rate is limited by the delivery of molecules to the substrate surface This makes the growth more controllable, in particular with the growth of alloys, as different precursors behave differently in the kinetic regime, and so their incorporation ratio changes with the temperature. This is therefore typically the preferred regime for the epitaxial growth of compound semiconductors.

In this thesis, the standard GaN MOVPE growth temperature used is around 1040°C, which corresponds to an overlap of the thermodynamics and mass transport regimes as we can see from Figure 15 (a). This work was performed during the PhD where we see that for growth temperatures ranging from 870 °C to 1040 °C we have a constant GaN growth rate with slight desorption. S. Fujieda et Al. performed the growth of GaN under NH_3 at lower

temperatures (from 450 °C to 850 °C). Data are presented in Figure 15 (b) where we see clearly the mass transport and the kinetics regimes [125].

Thus, the growth rate of GaN is defined as mass transport growth rate minus the desorption rate. In particular, the desorption rate is mostly controlled by reactor pressure, temperature and atmosphere. In general, as a carrier gas, H_2 causes a much higher desorption / etching rate compared to NH_3 or N_2. We also note that there are more parasitic reactions, that is to say pre-reactions between metal organic precursors and NH3, with higher pressure and higher temperature in the Al-content growth which can also reduce the growth rate in this regime.

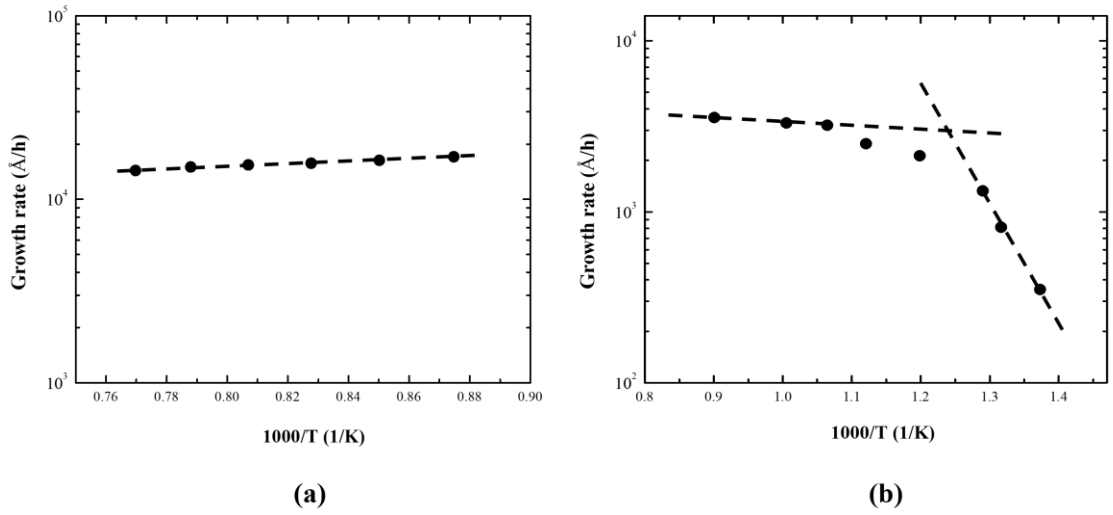

Figure 15: (a) PhD experiments on GaN growth rate under NH_3 for temperatures ranging from 870 °C to 1040 °C. (b) Work of S. Fujieda et Al. [125] on GaN growth rate under NH_3 for temperatures ranging from 450 °C to 850 °C.

We typically grew all our III-N ternary and quaternary alloys in the mass transport regime. This has two benefits; firstly, the growth rate is linearly dependent on the MO flow sent to the growth chamber and thus III-N layers thickness is easily predicted; secondly, alloy composition is also easier to control. [126]

II.3.3 Important quantities and concepts of MOVPE

II.3.3.1 Diffusion across boundary layer and maximum growth rate

As previously mentioned, during mass transport regime, chamber reactions are limited by the gas phase transport that limits the flux of input precursors.

The gas phase diffusion is roughly a temperature independent process in the simple case of diffusion through a mass transport boundary layer. The group III flux is expressed as follows:

$$J_{III} = \frac{D(P^*_{III} - P^i_{III})}{RT\delta_0} \qquad \textit{Eq. 17}$$

Where P^*_{III} is the input partial pressure of the group III source and P^i_{III} is the group III partial pressure at the growth interface. T is the growth temperature, D is the diffusion coefficient of the group III element; R is the ideal gas constant, and δ_0 is the thickness of a laminar-low boundary layer defined as the distance from the precursor maximum concentration in gas phase to growing surface. Figure 16 shows an illustration of δ_0.

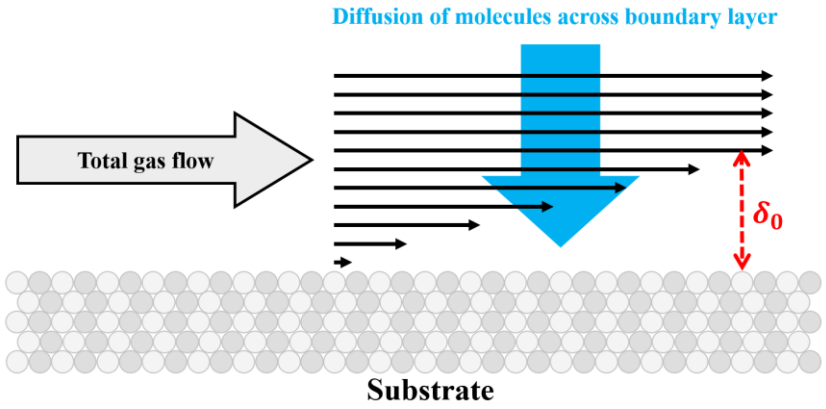

Figure 16: Illustration of the boundary layer δ_0 close the growing surface.

In the typical case of III-N growth, $P^*_V >> P^*_{III}$, thus the growth rate is independent of group V flow rate. This leads to a proportionality of the growth rate on the group III flux J as follows:

$$V_{growth} \propto J \qquad \textit{Eq. 18}$$

This formula shows that to increase the growth rate in mass transport limited regime we must increase the input flux of group III precursor in the gas phase.

We note that the boundary layer thickness can be changed through a variety of growth system modifications, such as varying the substrate rotation speed, changing the carrier gas composition, changing the total gas flow velocity and reactor pressure, etc.

This work has taken place using a close-coupled showerhead system, which has the advantage of uniform growth across the substrate, with uniform V/III ratio. The growth rate is also in principle independent of substrate rotation when less than 500 rpm and reactor pressure [120], although parasitic reactions can still be changed by reactor pressure.

II.3.3.2 The source molecules for III-N MOVPE growth

- **Group III molecules and their pyrolysis**

In general, two types of metal-organic molecules are used for the growth of III-N alloys; the trimethyl (TM) in which we find $3CH_3$ alkyls and the triethyl (TE) in which we find $3(CH_2CH_3)$ alkyls, each linked to a group III metallic atom (Al, Ga, In) as illustrated schematically in Figure 17. In our experiments, we only used TMGa, TEGa, TMAl and TMIn as precursors for group III molecules.

TMs are known to be more stable than TEs and so they are less likely to be involved in parasitic reactions. In addition, ethyl group molecules have a lower vapor pressure, than those with methyl groups. This makes methyl groups more frequently used in MOVPE.

On the other hand, TE are useful for the low-pressure MOVPE growth, as their usage reduces significantly the incorporation of carbon in III-N layers. Thanks to the pyrolysis process, all the organic groups are separated from the gallium in the gas phase. This removes the main source of carbon incorporation into III-N epitaxied layers.

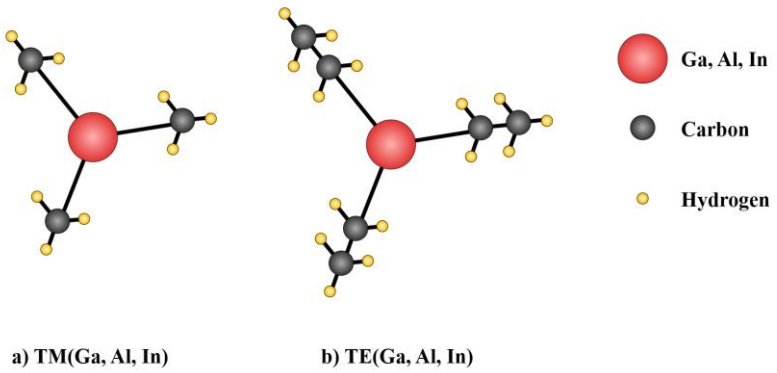

Figure 17: Illustration of III-N MOVPE precursor molecules: (a) trimethyl(Ga, Al, In) (b) triethyl(Ga, Al, In)

During the thermal decomposition process of group III molecules at elevated temperatures in an inert atmosphere, there are three main successive reactions that happen before the release of group III metal as shown in Table 6:

Reaction	$\Delta_{dissociation}$ (kJ/mol)
$Ga(CH_3)_3 \rightarrow Ga(CH_3)_2 + CH_3$	293
$Ga(CH_3)_2 \rightarrow Ga(CH_3) + CH_3$	72
$Ga(CH_3) \rightarrow Ga + CH_3$	164
$In(CH_3)_3 \rightarrow In(CH_3)_2 + CH_3$	267
$In(CH_3)_2 \rightarrow In(CH_3) + CH_3$	72
$In(CH_3) \rightarrow In + CH_3$	151

Table 6: TM precursors dissociation reactions & their free Gibbs energy change for the dissociation. [127]

We note that each chemical reaction has its own reaction rate and temperature at which is occurs.

- **Group V molecules**

The nitrogen (N) precursor used for the MOVPE growth of III-N materials is ammonia (NH_3), which requires high temperature to be decomposed. However, due to the high nitrogen's volatility combined with the requirement for high growth temperature for GaN MOVPE growth, it becomes relatively difficult to produce high quality minority carrier devices with low N-vacancy level. This leads to the high n dopant residual concentration in the GaN grown materials. [128]

Reducing the N vacancies concentration in the 2D growth can be achieved through the usage of high NH_3 partial pressures, e.g. large V/III ratio. This has the additional advantage of reducing carbon incorporation.

II.3.3.3 Parasitic gas phase reactions

At high growth temperatures and pressures, a decrease in growth rate can happen due to parasitic gas phase reactions. These are reactions between MO precursors and ammonia

which occur in the gas phase and which consume these molecules before they can be incorporated into the desired layers. These parasitic reactions can also result in changes in solid stoichiometry or even non-growth. Typically, high reactor pressures, high growth temperatures or a poor gas separation in the reactor lead to such phenomenon, and the most reactive precursors are those with aluminum or with ethyl groups which will lead to pre-reactions.

II.3.3.4 V/III ratio and partial pressures

The V/III ratio corresponds to the molar ratio of group V (NH_3) and group III (TMGa, TMAl, or TMIn) precursor flow. As mentioned before, due to the high volatility of N atoms, a high V/III ratio over 1000 is typically maintained for the MOVPE growth of 2D GaN.

A high V/III ratio means that the group III element is nearly completely consumed at the interface, and so we have:

$$p_{III}^{i} \ll p_{III}^{*} \qquad \textit{Eq. 19}$$

Where p_{III}^{i} and p_{III}^{*} are the partial pressures of group III element at the growth interface and in the gas phase, respectively.

Yet, the group V element is hardly diminished, and so:

$$p_{V}^{i} \approx p_{V}^{*} \qquad \textit{Eq. 20}$$

Where p_{V}^{i} and p_{V}^{*} are the partial pressures of group V element at the growth interface and in the gas phase, respectively.

We are interested in the real V/III ratio at the interface as this is where the growth occurs, i.e. $\frac{p_{V}^{i}}{p_{III}^{i}}$.

The equilibrium constant $K_{III/V}$ for the reaction of elemental III plus V elements to form solid III-N can be expressed by:

$$K_{III/V} = \frac{a_{III/V}}{p_{III}^{i} p_{V}^{i}} = \frac{a_{III/V}}{p_{III}^{i} p_{V}^{*}} \qquad \textit{Eq. 21}$$

Where $a_{III/V}$ is the activity at equilibrium. [120]

Thus, the real V/III ratio at the interface may be written as follows,

$$\frac{p_V^i}{p_{III}^i} = \frac{K_{III/V}}{a_{III/V}} p_V^{*2} \qquad \textit{Eq. 22}$$

Eq. 22 shows that the V/III ratio at the growth surface of the III-N material is proportional to the square of the partial pressure of the group V element, and so it is not related to the partial pressure of group III, which only controls the growth rate as already seen in Eq. 18. Thus, it is often preferable to compare group V partial pressures, rather than V/III ratios.

II.4MOVPE growth equipment: AIXTRON CCS

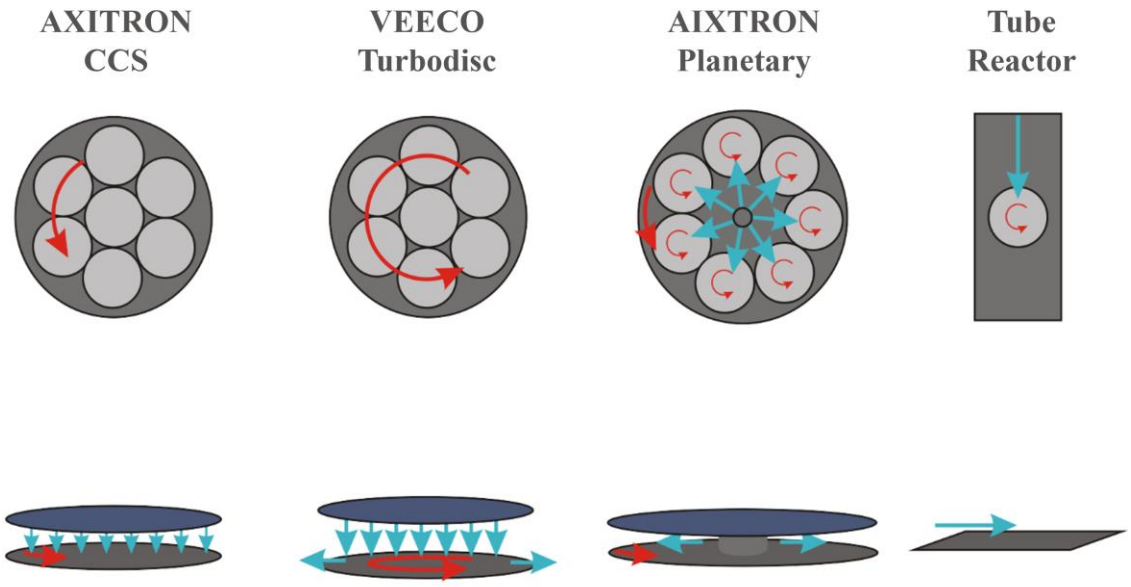

Figure 18: The different geometries of III-N growth equipments.

An AIXTRON CCS system consists of a showerhead very close to the wafer (typically 11 mm), ensuring intrinsic uniformity and few parasitic reactions. The VEECO Turbodisc appears similar, in that there is a uniform gas delivery (by "flow-flange"). However, the gas delivery is a lot further away, >50 mm, and the susceptor rotates very quickly, typically around 1000 rpm. This causes a turbo pump effect, which pulls the gases down on to the susceptor, and so leads to uniform growth if properly managed. The AIXTRON planetary system and the tube reactor are actually relatively similar geometries. The tube reactor consists of a single wafer which rotates while gas arrives from one side and evacuated from the other. A planetary system is effectively many tube reactors in one, where the gas is injected from the center of the chamber, passes across individually rotating wafers, and then

is evacuated from the edge. In this case, the whole susceptor carrying the wafers also rotates, to ensure the same growth on each wafer.

II.4.1 Overall tool setup

In this PhD work, a fully automated AIXTRON CRIUS R200 Closed Coupled Showerhead (CCS) reactor was used to perform the MOVPE growth of our III-N samples. A single 200 mm diameter silicon substrate is loaded for each growth. The showerhead architecture assures a good growth homogeneity, thanks to the homogeneously distributed gas across the wafer. The tool is pictured in Figure 19.

In this configuration the showerhead has a silicon carbide coated graphite shield clamped to the front side to enable in-situ chlorine cleaning. We also have a pyrometer which reads the backside of the shield to monitor its temperature. In this manuscript when we refer to the showerhead this means the showerhead plus the shield, except when explicitly mentioned.

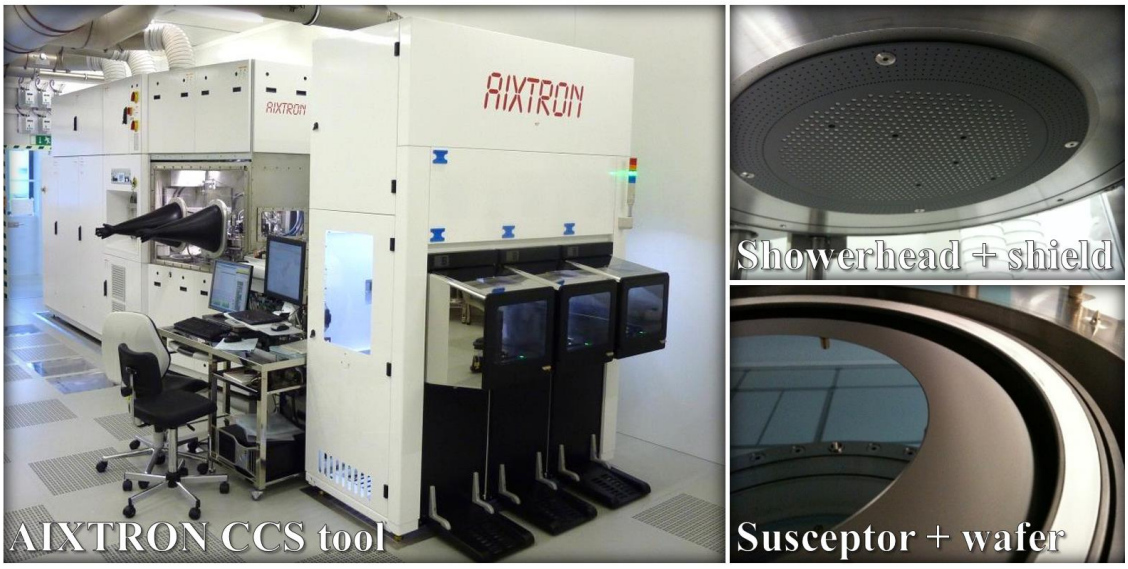

Figure 19: On the left, photo of the AIXTRON CRIUS R200 tool. Bottom right a view of the SiC coated graphite susceptor with the 200 mm diameter Si wafer. Top right a view of the showerhead with the shield.

As shown in Figure 20 the tool configuration carries the various reactants into the growth chamber using a carrier gas. Downstream, a scrubber treats the waste gases produced during the growth of III-N samples. The hydrogen and ammonia are burned for safety

reasons, and metal-organic molecules are also trapped due to some strict environmental rules.

For the growth of III-N samples, carrier gases such as nitrogen, hydrogen or a mix of both are used to push the main reactants, namely ammonia and MO, into the growth chamber and to ensure a constant total flow.

Mass flow controllers control the flow of each of the gases entering the growth chamber. This simplify growth calculation and control. A dilution step is also possible in such a system to allow the injection of very low flows.

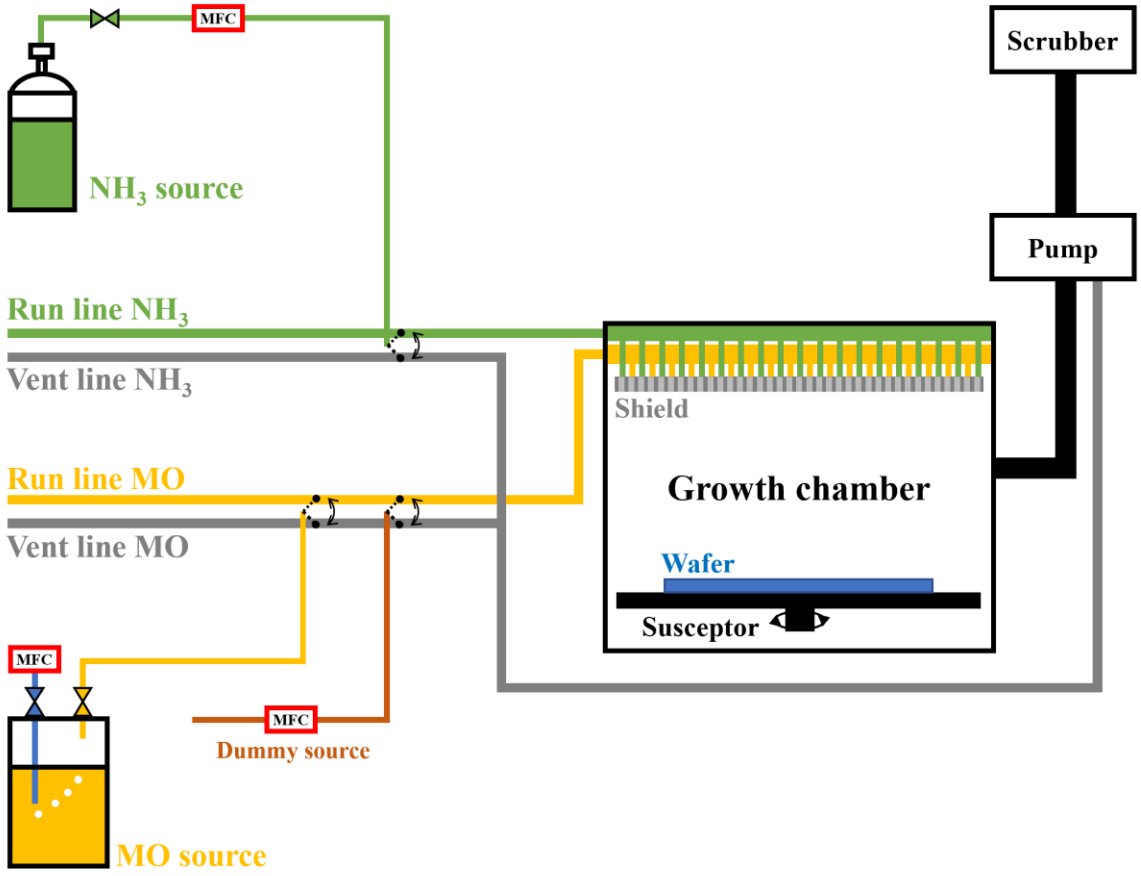

Figure 20: Simplified gas lines in AIXTRON CRIUS R200 tool.

In order to avoid gas pre-reactions and to accurately control the gas mixture in the growth chamber, the MO and the NH_3 sources are separated as shown in Figure 20 until they exit the showerhead into the chamber. For each of these, two lines are used for the reactants, the vent line and the run line. Each reactant gas can switch between these lines during the

MOVPE growth. The run line is linked directly to the growth chamber, while the vent line bypasses the reactor and sent to the scrubber.

The pressure in the vent and run lines is maintained at the same value, to reduce gas pulsing effects, which could affect the interfaces quality between the two grown layers. A dummy source is also used to this end, where a flow equivalent to the MO flow to be introduced is used. The dummy is initially going to the chamber, and then when the MO is switched to the chamber, the dummy switches to the vent at the same time.

Inside the growth chamber, samples are loaded by the transfer robot onto a SiC coated graphite susceptor: a circular horizontal disk. The SiC coating is used to avoid NH_3 reaction with the graphite, allowing us to perform high temperature material growth.

Below the susceptor, we have the heater; a planar coil, which is divided into three separately controlled zones as illustrated in Figure 21. The existence of the three zones of heating is very important. They are the key for the uniform temperature distribution across the substrate, especially in the case of wafer bow. We manage the three zones temperature in a way to keep the temperature uniform on the wafer surface, and thus ensuring a good growth temperature homogeneity.

Figure 21: a) SiC coated graphite susceptor, b) the heater coils, and c) the three zones of heating.

The standard distance used between the susceptor and the showerhead is 11 mm. This small distance prevents many parasitic chemical gas reactions, which could happen far from the substrate in the case of large showerhead – susceptor distance.

II.4.2 Bubbler operation

In such growth equipment, the MO precursors are stored in stainless-steel cylinders called bubblers. Source materials are in either solid or liquid state depending mainly on the temperature of the bubbler and source material.

As previously illustrated in Figure 20, during the MOVPE growth, the carrier gas (H_2 or N_2) defined by the MFC at the entrance to the bubbler, passes through the MO liquid precursor in the bubbler, and then leaves it directly to the run/vent valves, now saturated with MO.

Bubbler operation is a crucial part for the MOVPE growth comprehension and control, as this defines the exact amount of MO precursor sent to the growth chamber, and thus as described above it is directly related to the growth rates of layers.

The flow of metalorganic molecules F_{MO} sent to the growth chamber is described as follows:

$$\frac{F_{MO}}{F_{H_2}} = \frac{P_{MO}}{P_{H_2}} = \frac{P_{MO}}{P_{Bubbler} - P_{MO}} \qquad \textit{Eq. 23}$$

Thus:

$$F_{MO} = F_{H_2} * \frac{P_{MO}}{P_{Bubbler} - P_{MO}} \qquad \textit{Eq. 24}$$

Where F_{H_2} is the hydrogen carrier gas flow, $P_{Bubbler}$ is the bubbler pressure, and P_{MO} is the MO vapor pressure calculated as follows:

$$P_{MO} = 10^{b - \frac{a}{T}} \qquad \textit{Eq. 25}$$

Where T is the MO source temperature in unit of Kelvin, a and b are constant values, listed in Table 7, for the calculation of saturated vapor pressure for the precursor depending on temperature. The bubblers are kept in thermostatically controlled baths to ensure that their temperature stays constant, and thus that their partial pressure also stays constant. As a result, the molar flow of the precursor into the chamber is linked linearly to the gas flow injected into the bubbler.

Precursor	Melting point (°C)	Boiling point (°C)	a	b (K)
TMGa	-15.8	55.8	8.07	1703
TMAl	15.4	127	8.22	2134
TMIn	88.4	133.8	10.52	3014
TEGa	-82.3	143	8.08	2162
TEAl	-52.5	186	10.78	3625
TEIn	-32	184	8.93	2815

Table 7: Chemical properties of group III organometallic precursors, and constants for calculating the vapor pressure in Torr. [120]

II.4.3 In-situ characterizations

Inside the growth chamber, there are several detection systems to help us visualize different parts of the MOVPE growth. In particular, our tool is equipped with an EpiCurve®TT system from LayTec, which combines wafer curvature measurements, emissivity-corrected pyrometry and two-wavelength reflectance.

II.4.3.1 Wafer curvature measurements

For the measurement of wafer bow, we send two parallel laser beams from a small hole in the showerhead, called view-port, onto the wafer surface and after they are reflected and caught on a 2D CCD camera.

If the wafer has no bow, the distance between the detected beam points would be the same distance used as when they started at the source. If the distance is higher, this means the wafer is convex and vice versa for the concave case, as illustrated in Figure 22.

Once we have used this to calculate the radius of curvature, we can use a simple geometric calculation shown in Figure 23 to find the bow of the wafer with this formula:

$$b = R * \left(1 - \cos\left(\frac{r}{R}\right)\right) \qquad \textit{Eq. 26}$$

Where b is the bow, r is wafer radius and R is curvature radius.

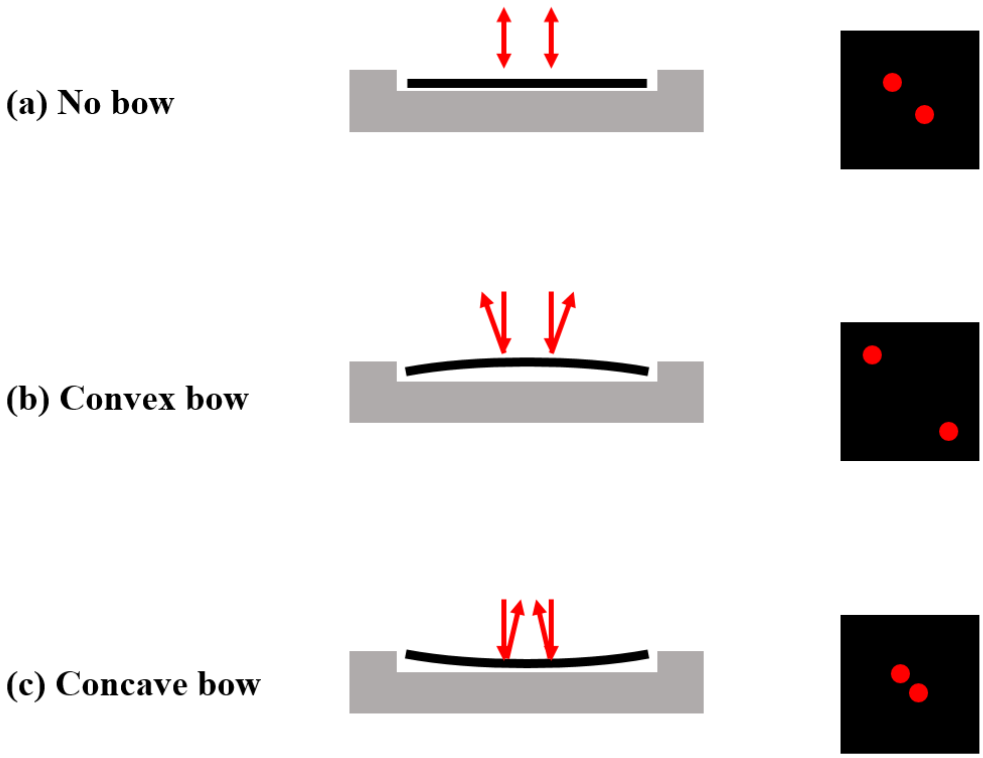

Figure 22: Wafer bow detection with two LASER beams and the associated 2D CCD camera observations.

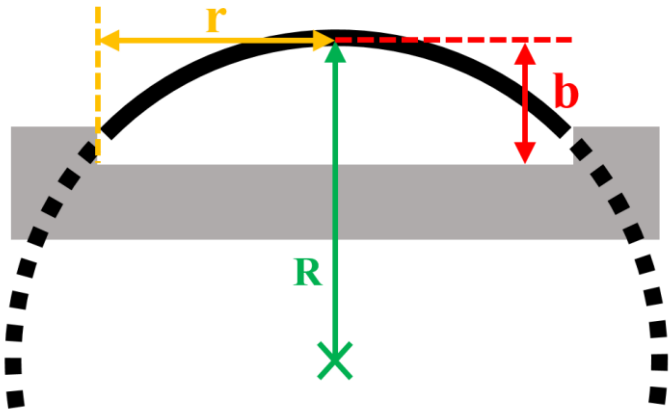

Figure 23: Geometric parameters that define wafer bow.

During the MOVPE growth of different III-N layers, the thermal mismatch, lattice mismatch and other limitations between layers can generate stress across the heterostructure.

This stress leads to strong wafer bow, which could induce temperature and composition inhomogeneities in the wafer along the diameter. In addition, it can generate wafer cracks and probably breaking the wafer inside the growth chamber.

Wafer bow is attributed to three factors:

- **Temperature gradient**

Coming from the large difference in temperature between the susceptor heated to over 1000°C, where the wafer is placed, and the showerhead, which is cooled down at a temperature of 50°C. This leads to a difference in temperature between the front and back side of the wafer, and thus to a concave bow of the wafer. This is reversed on cooling the wafer back to room temperature.

- **Lattice mismatch**

Coming from the growth of a material on a substrate with a different lattice parameter. If the top layer has a higher in plane lattice parameter than the substrate, the wafer becomes convex, and vice versa for the concave case. In the case of growth of GaN on silicon, this effect is used to create compression in the layers, and a convex wafer during growth as shown in Figure 24. This ensures that the wafer is flat when cooled back to room temperature.

- **CTE difference**

Coming from the difference in thermal expansion coefficients (CTE) between the top layer and the substrate, even if they have the same lattice parameters. If the top layer has higher CTE than the substrate, the wafer becomes concave as the temperature is reduced, and vice versa for the convex case.

The three causes of wafer bowing are illustrated in Figure 25.

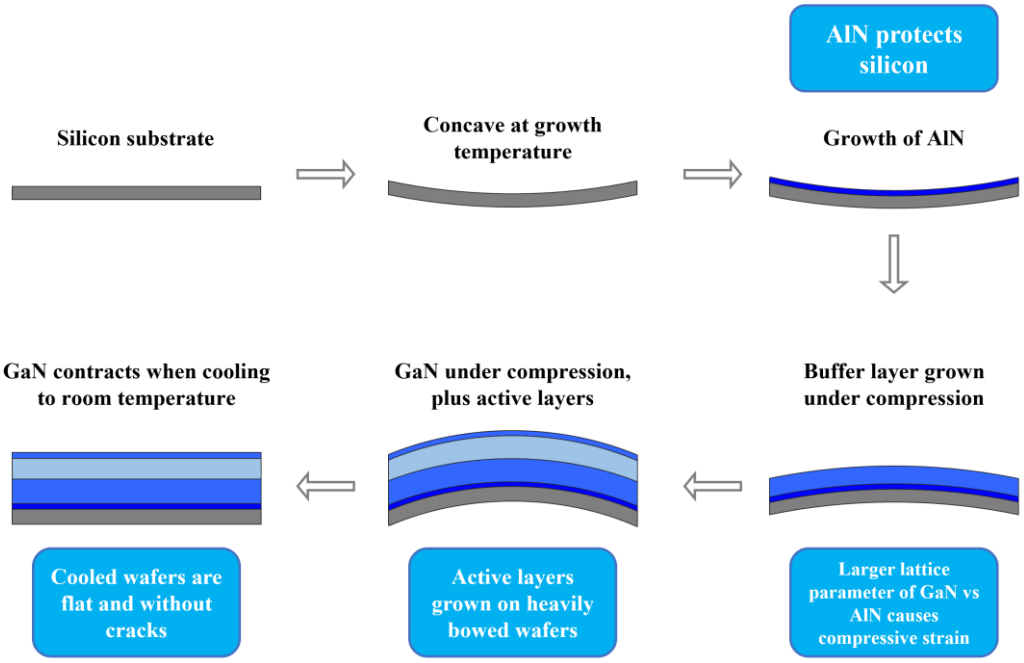

Figure 24: Basics of GaN on silicon growth.

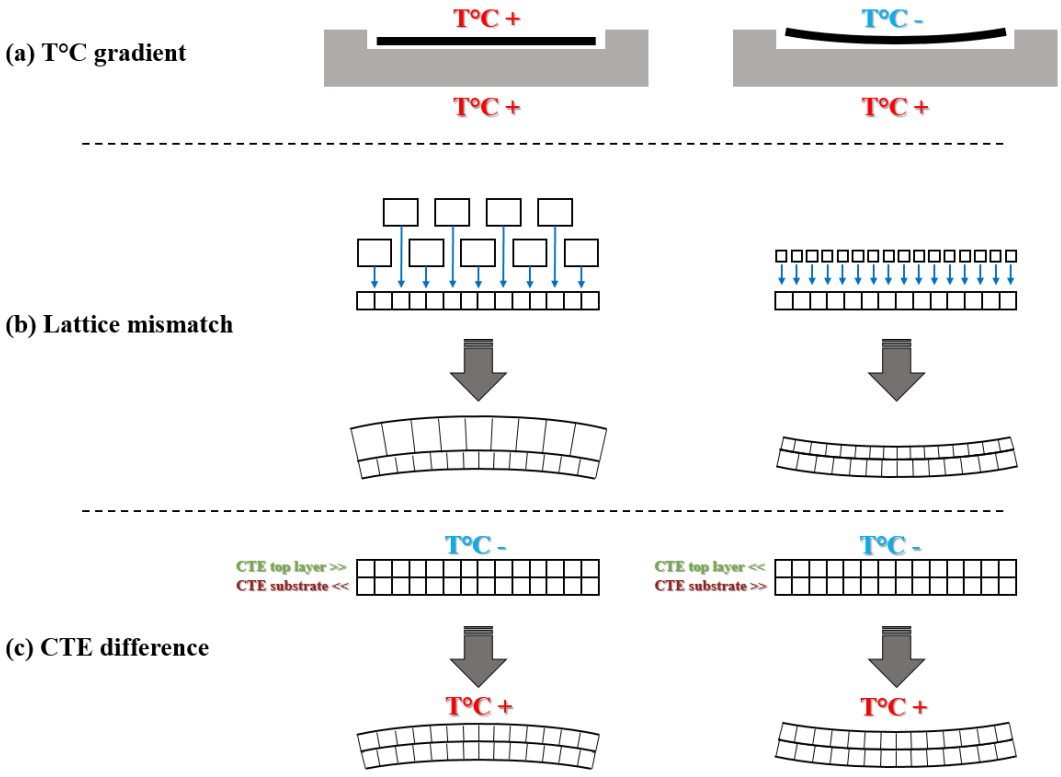

Figure 25: The reasons for wafer bow: a) temperature gradient, b) lattice mismatch, and c) CTE difference.

II.4.3.2 Emissivity-corrected pyrometry

Another important quantity that is measured during the MOVPE growth is the wafer temperature. This parameter influences alloy composition, crystal quality, sample roughness, layer thickness and many other material properties.

The pyrometry module combines a pyrometer and a reflectance measurement that give us an emissivity corrected temperature at two points on the wafer; at the middle, and edge of the 200 mm wafer.

The temperature measurement is based on blackbody theory, which specifies that a heated material that absorbs 100% of the incident electromagnetic radiation, regardless of frequency or angle of incidence, emits a thermal radiation. The thermal intensity radiation increases with the increase of blackbody temperature, followed by a shift of the thermal radiation peak toward lower wavelengths, as shown in Figure 26.

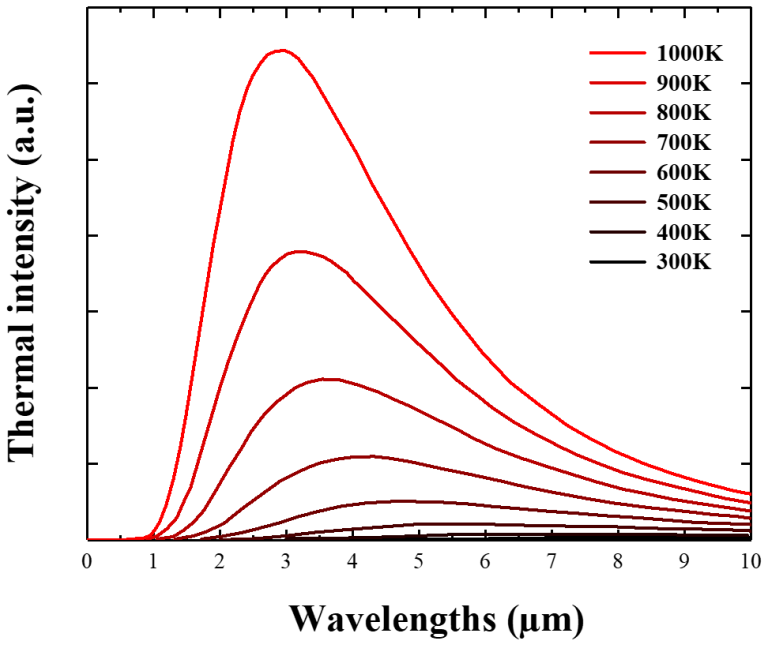

Figure 26: Black-body spectrum for temperatures between 300 K and 1000 K in a linear diagram.

Therefore, at a fixed temperature, the blackbody thermal intensity is a function of the emission wavelength, and its temperature dependence follows Planck's law. On the other hand, at a fixed wavelength, increasing the temperature leads to an increase in the intensity measured.

Thus, knowing the blackbody thermal intensity and the emission wavelength, we can determine the actual blackbody's temperature.

However, our material is not a true black body as it does not absorb 100% of the incident electromagnetic radiation, and it does not emit a radiation that fully corresponds to its temperature.

Thus, determining the temperature using Planck's law requires correction.

We used the following material emissivity to correct Planck's law:

$$\in(\lambda, T) = \frac{P}{P_s} \qquad \textit{Eq. 27}$$

Where P and P_s are respectively the emission of a real and a blackbody material.

Therefore, the corrected Planck's law that gives us access to the theoretical material thermal intensity becomes as follows:

$$dP = \in * dP_s = \in * \frac{2}{h^4 c^3} * \frac{(\hbar\omega)^5}{e^{\frac{\hbar\omega}{k_B T - 1}}} * d\lambda \qquad \textit{Eq. 28}$$

Where $\omega = \frac{2\pi}{c}$ and $\hbar = \frac{h}{2\pi}$.

h and k_B are Planck's and Boltzmann's constants respectively. c is the light speed, λ is the emission wavelength, and T is the material temperature.

In addition, and according to Kirchhoff's law, the emissivity $\in$ of a material is equal to its absorption α. Thus,

$$\in(\lambda, T) = \alpha\,(\lambda, T) \qquad \textit{Eq. 29}$$

Where,

$$\alpha + T + R = 1 \qquad \textit{Eq. 30}$$

T and R are respectively, the material transmission and reflection electromagnetic parameters.

Now using all the equations described above, we will be able to estimate the wafer temperature before growth. Finally, in order to correct the temperature during growth of transparent layers, we also have to examine the reflectivity.

II.4.3.3 Two-wavelength reflectance

The pyrometry module also performs a reflectance measurement, with which we can calculate the grown layer thickness, e.g. the growth rate, and the surface quality. Reflectance measurements are usually performed with either 405 nm or 950 nm LED wavelengths. The light beams are sent through the view-port into the sample surface with a normal incidence angle, and then the signal reflects back to the detector.

More precisely, the incident beam hits the surface and undergoes reflection and refraction as illustrated schematically in Figure 27. The reflected part goes directly into the detector and the other refracted part continues its way into the interface between the growing top layer and the substrate, and then it gets reflected again. The two major reflected beams meet on the detector, and they interfere. As the growth progresses, this interference passes from constructive to destructive, resulting in oscillations.

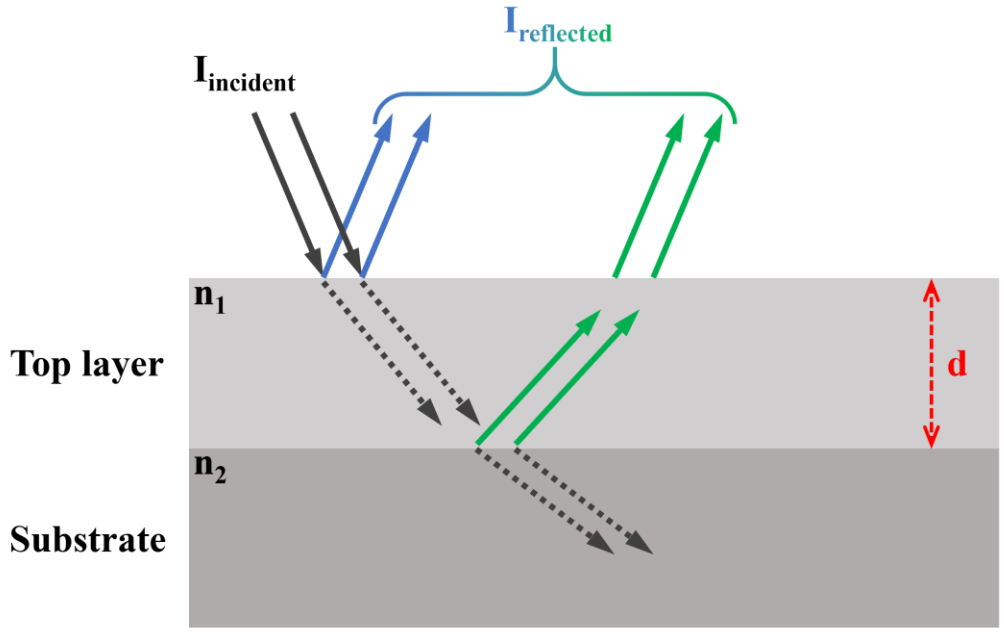

Figure 27: Schematic of the optical configuration of a light beam reflectance measurement.

Using the time between the start and the end of an oscillation, we can deduce the thickness of the grown layer and the growth rate of each layer. The distance between two maxima or minima of an oscillation corresponds to a layer thickness d as follows:

$$d = \frac{\lambda}{2n} \qquad \textit{Eq. 31}$$

Where λ is the reflectance wavelength used, either 405 nm or 950 nm in our case, and n is the refractive index of the growing layer. For GaN and AlN, n is 2.35 and 2.15 respectively.

Using these numbers, we can deduce that the distance between two maxima or two minima during the growth of pure GaN material, is equivalent to a GaN layer thickness of 86 nm and 202 nm for a reflectance measurement with 405 nm and 950 nm respectively. Thus, we can deduce the total GaN layer thickness based on the total oscillation length.

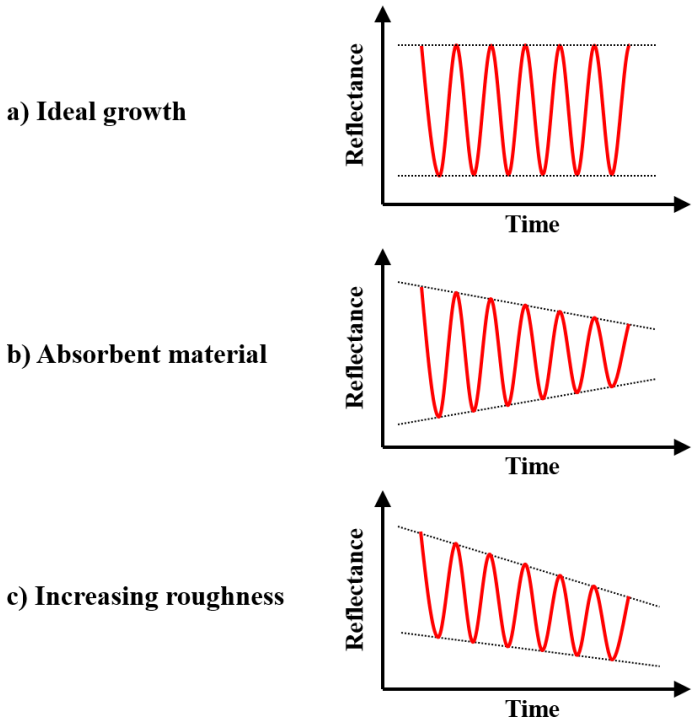

Figure 28: Fabry-Pérot oscillations cases, in a) an ideal growth case where the top layer is transparent and it has a very smooth surface, b) an absorbent material case, and in c) a case of a roughening surface.

In addition to the layer thickness, the reflectance intensity can also provide us with information on the surface/material quality. In an ideal growth case, where the growing top layer is very smooth and transparent to the laser beam, the oscillation of the reflectance measurement has a constant amplitude, as illustrated in Figure 28. In another case, the growing material could present a certain absorbance at a given wavelength. The amplitude starts to decrease with the increase of the growing top layer thickness. This case can also be attributed to a change of the layer refractive index due to some alloy fluctuation during the

growth. The third case is where we see an overall decrease of the oscillation's intensity, which indicates a surface roughening during the growth.

II.5 Standard HEMT buffer epitaxial heterostructure

As already mentioned in the first chapter, the major purpose of this PhD work is to grow pure InAlN barrier layers on GaN on silicon substrates for HEMT applications.

A set of buffer layers is used to compensate the high lattice mismatch and the large CTE difference between the silicon substrate and the thick GaN layer. The aim of these buffer layers is to ensure good quality crack free GaN and a flat wafer after growth.

A typical HEMT epitaxial structure consists of (from bottom to top, cf. Figure 29) the following layers:

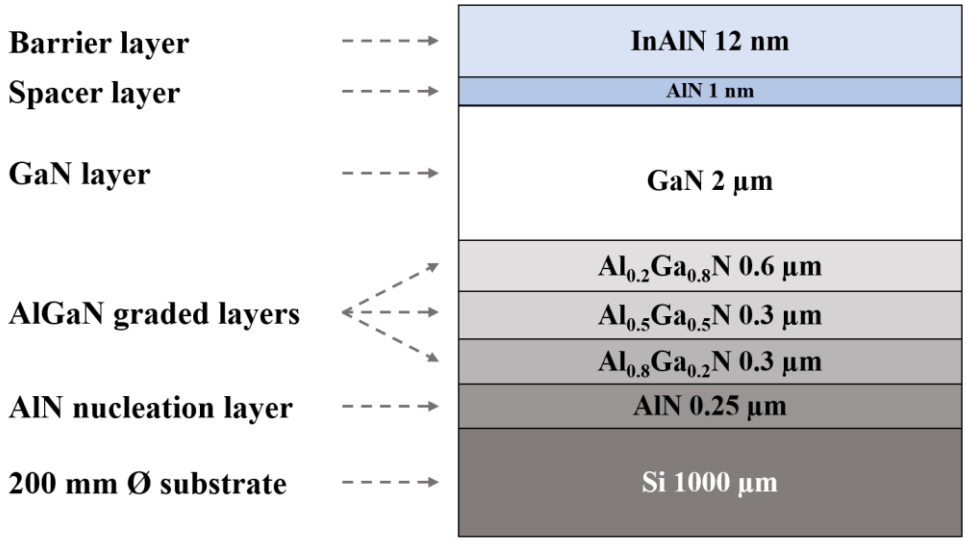

Figure 29: Schematic of HEMT growth structures.

Substrate*:* Due to the high cost of growing GaN on a native substrate, GaN epitaxy is performed on a non-native material substrate such as sapphire (Al_2O_3), silicon carbide (SiC), and silicon (Si(111)).

As already mentioned in chapter 1, despite the high lattice mismatch of 17% and the large CTE difference with GaN, silicon remains the most attractive economic solution for

mass production of GaN based power devices. We therefore used it as a substrate for the MOVPE growth of GaN.

Nucleation layer: To overcome the high lattice mismatch and the large CTE difference between silicon and GaN, a combination of buffer layers has been implemented without which the GaN layer would be left under a tensile stress, with the formation of cracks.

We firstly anneal the silicon to desorb all the oxide and rearrange silicon surface atoms. Then we grow 30 nm of AlN nucleation layer at 1000°C to initiate the growth and correctly wet the substrate. We use the nucleation temperature to control the final bow of the wafer as explained in this reference [129]. This is followed by a 220 nm AlN nucleation layer growth at 1100°C to improve the crystal quality. The AlN layer also protects the silicon from gallium, which reacts very strongly with silicon, leading to rapid degradation of the GaN layer known as "melt-back etching", as observed for direct growth of GaN on Si.

Graded AlGaN buffer layers: After the growth of AlN nucleation layer, three AlGaN graded layers with 80%, 50% and 20% of Al composition are grown successively in order to gradually reach the lattice parameter of GaN. This is also intended to induce residual compressive strain in the layers, which compensates in advance for the tensile strain that will be present upon cooling down from the growth temperature. The temperature used for the growth of AlGaN layers is 1080°C.

GaN layer: A 2 µm thick GaN buffer layer is grown after the growth of AlGaN graded layers, and this layer is also under compressive strain to compensate for the difference in CTE between GaN and silicon during the cool down, as previously discussed in Figure 24. The temperature used for the growth of such layer is 1050 °C. In the last few hundred nanometers from the surface we ensure a lower incorporation of carbon atoms, through a lower growth rate, higher temperature, higher pressure and higher NH_3 flow. Carbon impurities tend to increase GaN electrical resistance and scattering effects, resulting in lower 2DEG HEMT mobilities, and so a poor HEMT performance.

Spacer layer: The 2DEG formed at the pseudo-substrate/barrier interface is a critical part to tune the characteristic of GaN based HEMT devices. The AlN spacer increases the discontinuity of the conduction band at the heterojunction interface, thanks to its larger band

gap, which plays a dominant role for the significant increase of 2DEG concentration. Additionally, the AlN spacer helps in reducing alloy scattering, which increases the mobility of the device [130]. We use a thickness of 1 nm which leads to a good compromise in terms of N_s and μ_s.

Barrier layer: This layer is the most critical layer in the HEMT heterostructure. It has a wider bandgap than the GaN channel layer, which make it possible to form the 2DEG. We generally use AlGaN material as a barrier for GaN-based HEMTs, whereas in this work we will be working on InAlN barriers with thickness around 12 nm.

II.6 Characterization techniques

Following the MOVPE growth of III-N samples, several measurements can be carried out on the epitaxial wafer to analyze the structure. Figure 30 summarizes the techniques used to characterize the different elements of our HEMT epitaxial structures. These are primarily: Atomic Force Microscopy (AFM), Low-Temperature Photo-Luminescence (LT-PL), Wavelength Dispersive X-ray Fluorescence (WDXRF), X-Ray Reflectivity (XRR), High-Resolution X-Ray Diffraction (HRXRD), Secondary-Ion Mass Spectrometry (SIMS), Plasma Profiling Time of Flight Mass Spectrometry (PP-TOFMS), and Four-Point Probe (4PP).

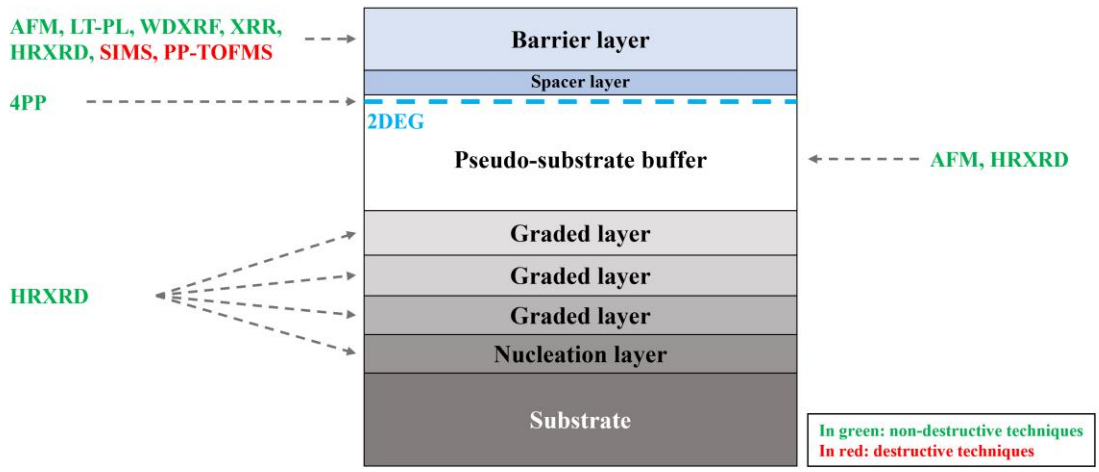

Figure 30: The main techniques used for HEMT structure characterization.

II.6.1 Morphological characterization

II.6.1.1 Atomic Force Microscopy

Atomic Force Microscopy (AFM) is a non-destructive characterization technique that allows us to examine the morphology of the sample surface going from 30x30 μm^2 down to nearly 0.5x0.5 μm^2. We used a Bruker FastScan (cf. Figure 31) for all the III-N samples studied with AFM in this manuscript. The images were processed using NanoScope Analysis 1.9 software.

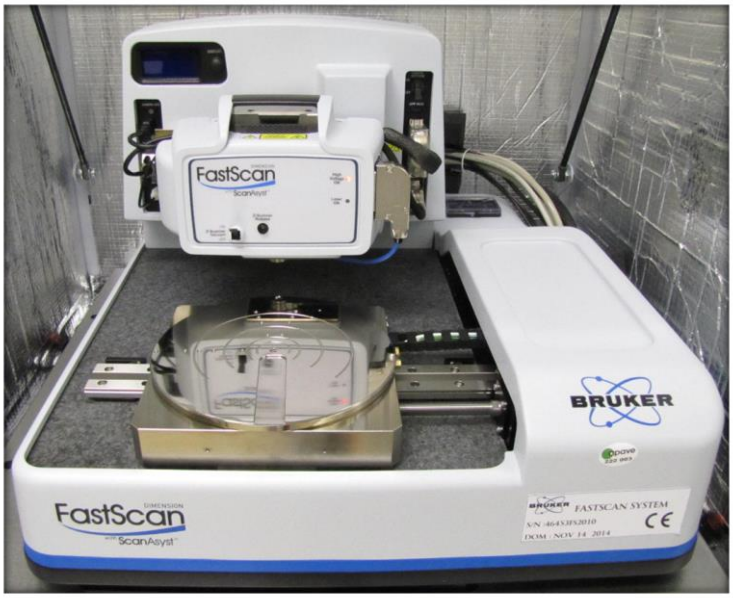

Figure 31: AFM equipment with FastScan system mounted.

The AFM principle consists in approaching a silicon probe to a surface, and then measuring the force of interaction between the atoms at the end of the sharp tip and each of the atoms of sample surface. This makes it possible to carry out surface topography measurements on a nanometric scale. A schematic diagram of a typical AFM setup is described in Figure 32.

When the tip gets near to the surface, it experiences numerous types of forces, namely capillary, van der Waals, and electrostatic forces etc. The probe is initially attracted by Van der Waals interactions and when the probe gets very close to the surface, the electron orbitals of the atoms on the surface of the probe and specimen start to repel each other. The repulsive interaction between the two molecules can be described by the power-law potential caused

by overlapping of electron clouds resulting in a conflict with the Pauli exclusion principle [131]. The nature of the forces versus the tip-surface distance can be seen in Figure 33.

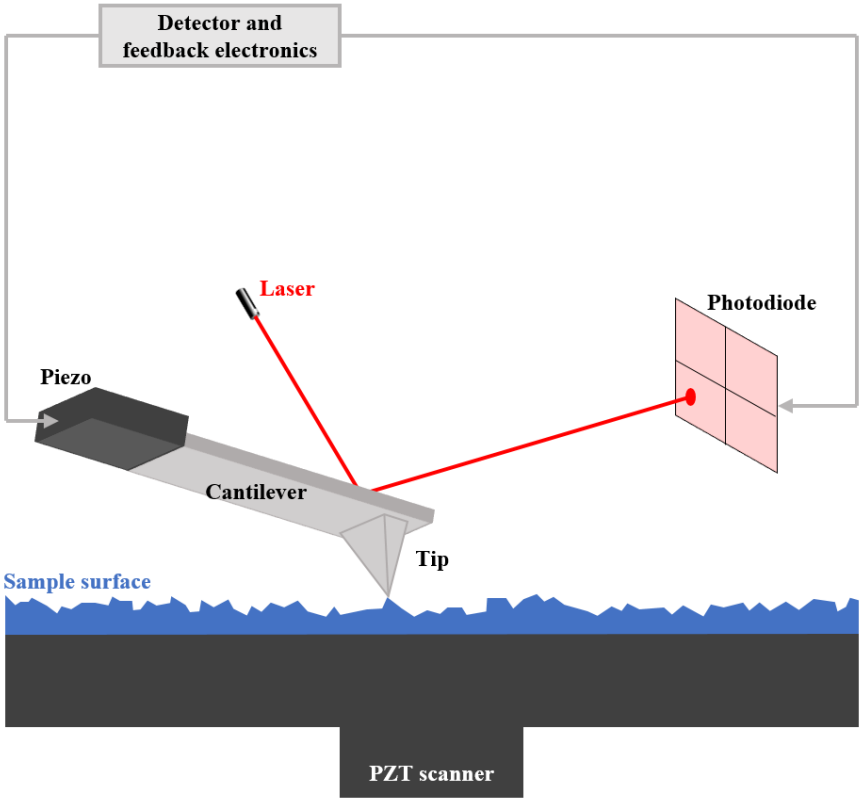

Figure 32: Schematic diagram of a typical AFM setup.

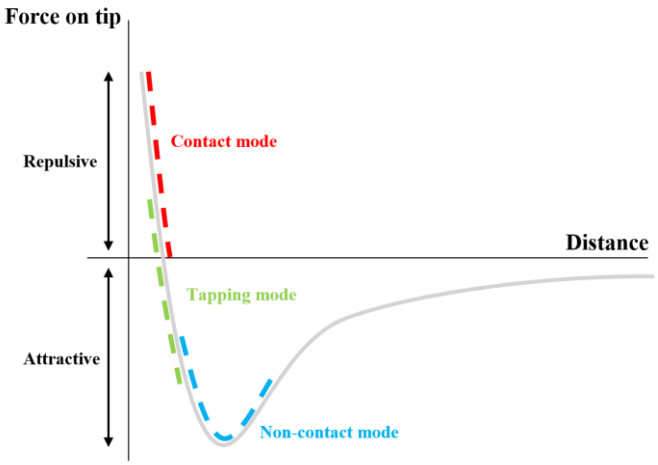

Figure 33: Variation of force with tip-surface distance.

Variations in the tip-surface distance change the force between them. This causes deflections in the cantilever and so in the laser spot on the photodiode detector. In short, the deflection in the laser spot is a function of the change in tip-surface distance. We note that the optical measurement system consists of a semiconductor laser emitting less than 1mW at a wavelength of 670 nm. The laser beam is reflected on the rear face of the silicon cantilever and then sent, through an optical path, to a photodiode separated into four dials as shown in Figure 32.

As illustrated in Figure 33, the AFM technique can be operating in three distinguished operation modes:

- **Contact mode**

In this mode, we mainly use the repulsive forces. The probe presses on the sample surface and then pushed away due to Pauli exclusion principle. This provokes a deviation of the cantilever, which is detected by the photodiode.

- **Non-contact mode**

In the non-contact mode, we mainly use the attractive forces. The cantilever is kept a few tens or hundreds of angstroms away from the sample. However, the forces are very weak and therefore very difficult to measure. Practically, this mode is rarely used.

- **Tapping mode**

In the tapping mode, we use both repulsive and attractive forces. A probe oscillating at free-air amplitude (A_0) near to its resonant frequency (ω_R) is scanned over the sample surface. As the name “tapping mode” suggests, the tip of the cantilever taps the sample surface for a very short period of time reducing the oscillation amplitude to $A<A_0$. In amplitude modulation scheme, a scan controller moves the sample or the probe in vertical direction (i.e. Z-direction) such that the tapping oscillation amplitude A stays constant at a pre-set amplitude A_{set}. In frequency modulation scheme, the shift in the resonance frequency is measured and used in the feedback loop. [132]

We used the AFM technique exclusively in tapping mode for all the topography measurements in this work.

II.6.2 Optical characterization

II.6.2.1 Low-Temperature Photo-Luminescence spectroscopy

Low-Temperature Photo-Luminescence (LT-PL) spectroscopy is a non-destructive characterization technique which allows to find the band gap energy of a material and also to study its radiative defects.

The PL principle is based on the excitation of a semiconductor material with a laser of wavelength corresponding to an energy greater than the material band gap energy (Eg). Upon absorption of photons with this energy, a quasi-particle is created consisting in the electron photo-generated in the conduction band bound, through coulombic interaction , to the hole left behind in the valence band. This quasi-particle is called an exciton and the energy binding the electron and its hole is called the exciton binding energy. The excitons have limited lifetimes and can recombine either non radiatively (mainly because of structural defects) or radiatively. Photoluminescence spectroscopy consists in following the intensity of radiative emission as a function of the emitted photon energy or wavelength. In a very simplified model, at low T, the different radiative transition mechanisms of an electron excited by the PL laser through the Forbidden Band are: 1) Band to Band (B to B) recombination BC to BV, 2) formation of a free exciton (FX): electron and hole linked by Coulomb interaction, 3) formation of a linked exciton on a donor (D°h), 4) formation of an exciton linked to an acceptor (eA°), 5) formation of a donor-acceptor pair (DAP). These mechanisms are schematized in Figure 34 [133]. At RT, the excitons are said to be dissociated (the coulomb interaction is weaker than the KT) or the binding energy on the donor or acceptor is weaker than the KT. So, we only see the edge of the band (near Band Edge) and the bands associated with the deep levels.

Hence PL is a direct mean to determine the gap of the material and/or the position of the energy levels assisted to impurities (intentional of non-intentional). In the course of this PhD, we have been using PL spectroscopy at room temperature to determine the gap of the material, hence the composition of the considered alloy.

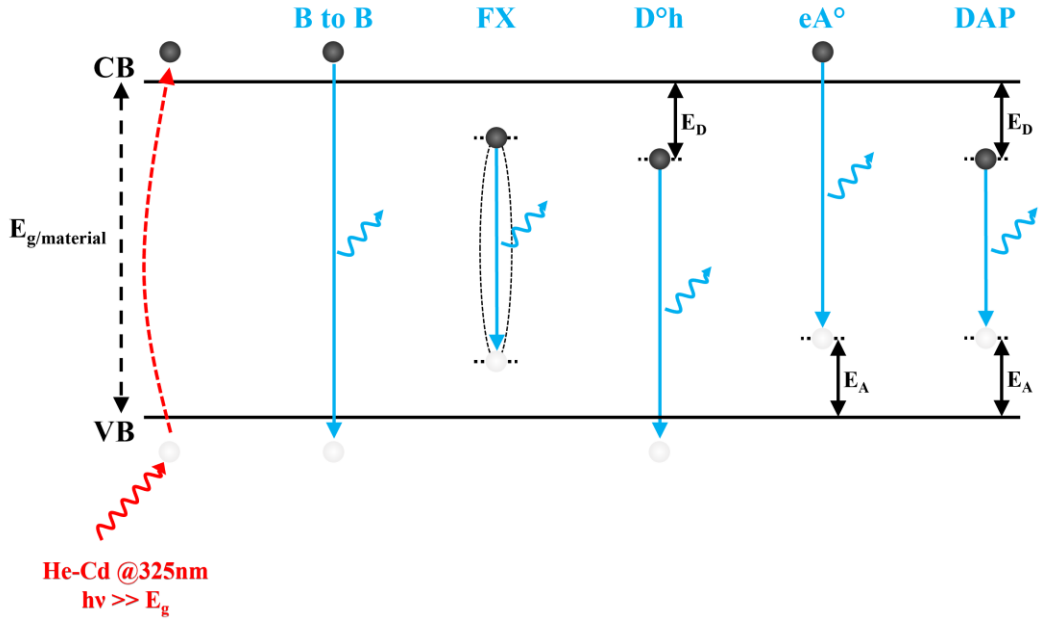

Figure 34: Luminescence mechanisms from a direct band gap semiconductor material.

For PL characterizations, we used a Horiba LabRAM HR equipment (cf. Figure 35), which allows photoluminescence measurements to be made at room temperature and low temperature (6K) using a helium cryostat. We used for our experiments a laser wavelength of 325 nm (Helium-Cadmium Laser) that allows us to excite GaN material and its ternary and quaternary alloys at an energy higher than their forbidden band.

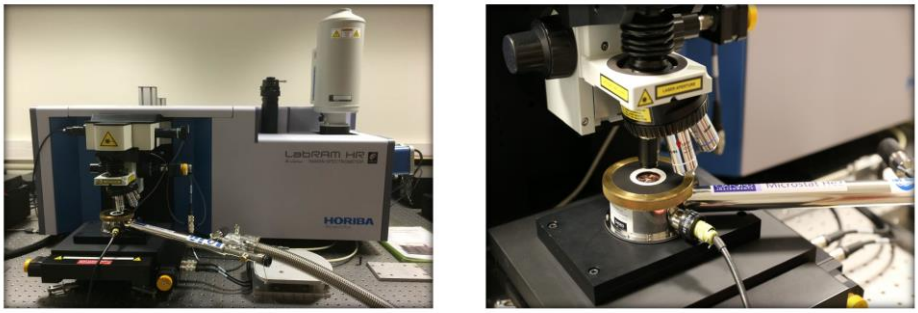

(a) **(b)**

Figure 35: a) Horiba LabRAM HR tool, b) the objective microscope turret with the removable He cryostat.

In this thesis, LT-PL were mainly used for the characterization of thin InGaN layers. For these, we deduced In% in such layers using the following equation:

$$E_g(InGaN) = xE_g(InN) + (1-x)E_g(GaN) - bx(1-x) \qquad \textit{Eq. 32}$$

Where $E_g(InGaN)$, $E_g(InN) = 0.7\ eV$ [134], and $E_g(GaN) = 3.39\ eV$ [135] are the band gap energies of InGaN (taken from main LT-PL peaks data), InN and GaN respectively. x is the indium molar fraction in InGaN layers, and b is the bowing parameter accounting for the nonlinearity of the InGaN band gap with composition. We used a bowing parameter of 1.204 eV using the following equation [136]:

$$b^{(strained)} = 1.154 * E_g^{InN} + 0.396 \qquad \textit{Eq. 33}$$

The bowing parameter shown in *Eq. 33*, is appropriate for thin strained InGaN layers with low In%, which fits well with our layers, as we are usually growing InGaN layers with low In% and thicknesses inferior to the theoretical critical thickness for plastic deformation as deduced from the model of Fisher et al. [136] [137]

II.6.2.2 Wavelength Dispersive X-Ray Fluorescence

X-Ray Fluorescence (XRF) spectroscopy is a non-destructive characterization technique used to analyze the composition of semiconductor films. Incident X-rays excite the atoms of the sample by ionizing them through the ejection of a core electron. The atom de-excites through the transition of an electron of a higher level towards the vacant quantum level. This de-excitation is accompanied by the emission of an Auger electron or by the emission of a photon. It is this last phenomenon that is called X-Ray Fluorescence, as illustrated in Figure 36. In general, elements lighter than sodium (Z = 11) are difficult to measure with XRF, because the fluorescence yield becomes too low and the predominant emission is that of Auger electrons.

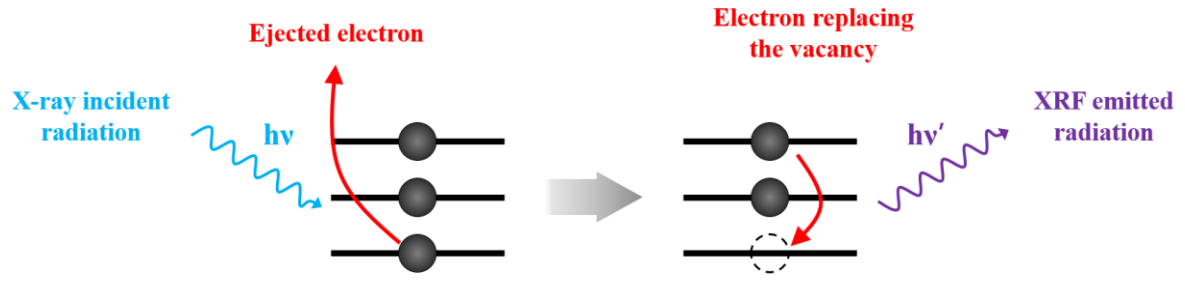

Figure 36: Visualization of the principle of X-Ray Fluorescence.

There are two methods of analyzing X-Ray Fluorescence radiation, either by EDXRF (stands for Energy Dispersive X-Ray Fluorescence) or by WDXRF (stands for Wavelength

Dispersive X-Ray Fluorescence). The major difference is the introduction in the second case of an analyzer crystal placed before and / or after the sample, which allows the selection of a single wavelength. Thus, the WDXRF technique has a reduced collected intensity but it is possible to resolve each atomic emission line. The WDXRF spectrometer tool used in our studies is an AZX400 manufactured by RIGAKU (cf. Figure 37).

Figure 37: Spectrometer tool: RIGAKU AZX400.

InAlN samples were analyzed by considering the Al-K_α and In-L_β fluorescence lines, which do not exhibit spectral overlap. The fundamental parameters method [138] is used to perform quantitative measurements by calibrating the instrument with Al and InP. The measurements by WDXRF with this instrument make it possible to detect changes in relative atomic compositions with a good accuracy of ± 0.1%at.

II.6.3 Structural characterization

II.6.3.1 X-Ray Reflectivity

X-Ray Reflectivity (XRR) is a non-destructive characterization technique used to determine the thickness, density and roughness of thin layers deposited on a substrate. XRR uses the specular reflection of a beam of X-rays measured at grazing incidence on a plane sample.

When a light beam crosses an interface, Descartes' law predicts that the angle of refraction can be determined by the following relationship:

$$n_1 \sin\left(\frac{\pi}{2} - \theta_1\right) = n_2 \sin\left(\frac{\pi}{2} - \theta_2\right) \qquad \textit{Eq. 34}$$

Where n_1, n_2 are the medium indices and θ_1, θ_2 are the angles of incidence and refraction as defined in Figure 38. This relationship remains effective in the case of X-rays reaching a surface at a grazing angle.

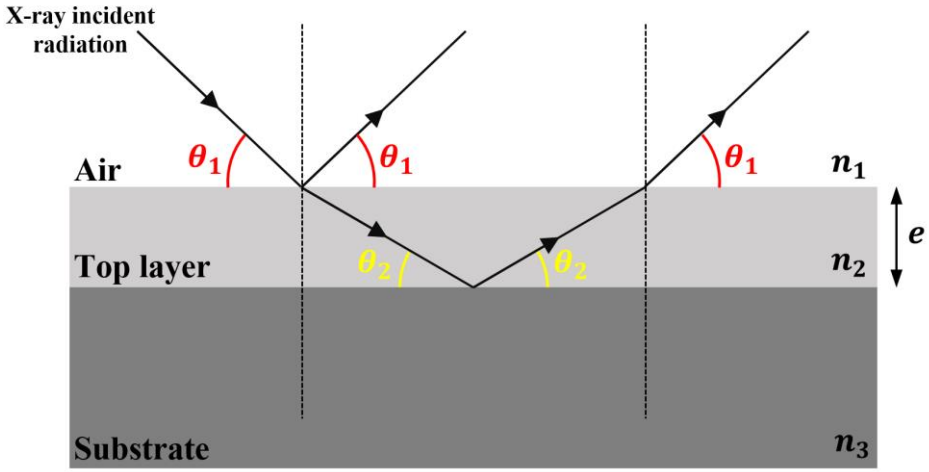

Figure 38: XRR measurement principle.

For X-rays, all materials have an index slightly less than 1. Thus, we can express the index of the material by $n_2 = 1 - \delta$, where δ is a very small positive number (of the order of 10^{-6}). This corrective term is proportional to the electron density of the material ρ_e, to the radius of the electron r_e, and to the square of the wavelength of the incident beam λ. It is defined by the following equation:

$$\delta = \frac{\lambda^2}{2\pi} r_e \rho_e \qquad \textit{Eq. 35}$$

Thus, considering that the first medium is air with an index $n_1 = 1$, *Eq. 34* is rewritten in the following form:

$$\cos(\theta_1) = (1 - \delta)\cos(\theta_2) \qquad \textit{Eq. 36}$$

There is therefore a critical angle θ_{1c} below which there is no refraction and the reflection is total. This critical angle can then be expressed as follows:

$$\cos(\theta_{1c}) = (1 - \delta) = 1 - \frac{\lambda^2}{2\pi} r_e \rho_e \qquad \textit{Eq. 37}$$

The critical angle is therefore linked to the electronic density of the material considered, which is itself correlated to its density [139]. For angles greater than the critical angle, the radiation enters the material and is both reflected and refracted. The radiation that has penetrated the layer can again be reflected and refracted many times with the substrate and / or the air, and finally comes out with a certain difference in path compared to the first reflected beam (cf. Figure 38). This phenomenon gives rise to interference, which makes oscillations in the spectra of XRR measurements called Kiessig fringes. Examples of Kiessig fringes are shown later in the manuscript.

As a first approximation, the period of the oscillations is inversely proportional to the thickness of the thin layer according to the following relationship:

$$e = \frac{\lambda}{2\Delta\theta} \qquad \textit{Eq. 38}$$

Where e is the thickness of the thin layer, λ is the wavelength of the incident radiation and $\Delta\theta$ is the period of the interference fringes. We note that this relationship is no longer valid for low θ_1 angle values.

A measurement with XRR therefore consists in carrying out a grazing incidence scan of the angle of incidence θ_1 (which is also the collection angle) over a few degrees. The different signatures of the acquisition are then studied in order to determine the critical angle, the period of the interference fringes and the attenuation of the curve (which gives information on the roughness of the layer). In general, a simulation of the sample fringes is necessary in order to determine all its characteristics.

The III-N samples were analyzed on the XRD3 JV/BRUKER, DELTA-XM model (cf. Figure 39). The data simulation were processed with JV-REFS software from BRUKER.

Figure 39: XRD/XRR tool: XRD3 JV/BRUKER, DELTA-XM.

II.6.3.2 High-Resolution X-Ray Diffraction

High-Resolution X-Ray Diffraction (HR-XRD) is a powerful, non-destructive characterization technique widely used for structural characterization of semiconductor layers. High-resolution means highly collimated and monochromatic X-ray beams and precise goniometry. This technique provides a wealth of information about epitaxial materials especially on the crystal lattice parameters, stress in the films, crystal quality, film thickness and many other important properties.

In a crystalline material, the atoms composing the crystal lattice are distributed in the form of parallel and equidistant planes, as shown in Figure 40. Planes are separated by a distance of the order of a few angstroms. By illuminating the crystal from different angles of incidence with a monochromatic and parallel X-ray beam, we obtain by diffraction an interference figure characteristic of the families of the planes of the material. In reciprocal space, the family of planes are represented with dots (Figure 41). The planes of the family (0002, 0004, and 0006) parallel to the sample surface are known as symmetrical reflections while the other types of planes inclined to sample surface are asymmetrical reflections.

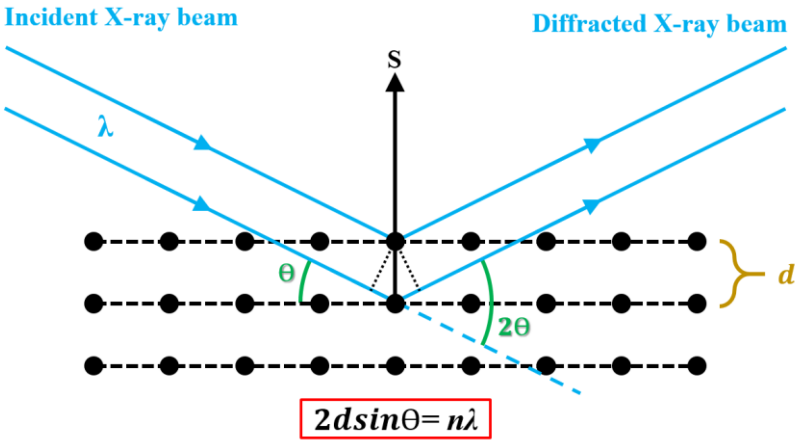

Figure 40: Diagram of the principle of Bragg's law.

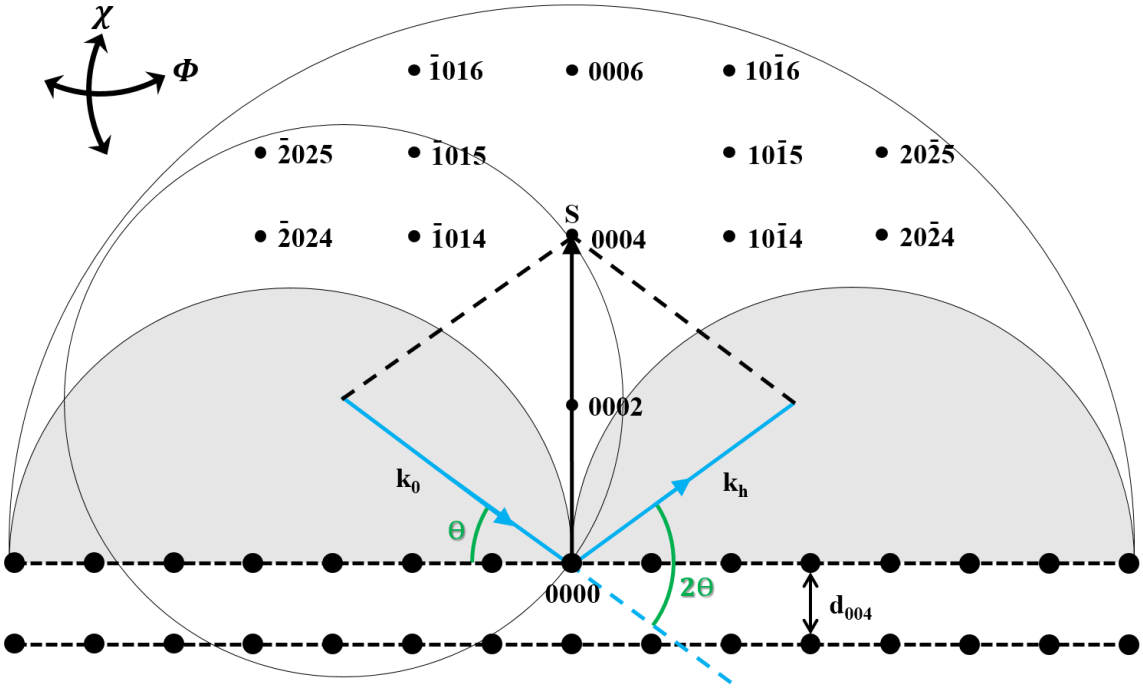

Figure 41: A section through reciprocal space for a c-oriented GaN film. The regions shown in grey are the inaccessible regions (where the sample blocks one of the beams). k_0, k_h, and S are respectively the incident, diffracted and scattering vectors with respect to the crystal. Figure reproduced from [140].

The figure responds to Bragg's law, i.e. the interferences are constructive and form diffraction peaks in specific directions which can be determined by following Bragg's law:

$$2dsin\theta = n\lambda \qquad \textit{Eq. 39}$$

Where d is the distance between two crystallographic planes, θ is the deflection half-angle, n is an integer corresponding to the order of reflection and λ is the wavelength of the incident X-ray beam. To obtain these interferences, λ must be of the order of d, that is to say a few angstroms, and that is why we use X-rays.

Figure 42 represents a schematic of the sample reference frame to show the different possible axes of rotation.

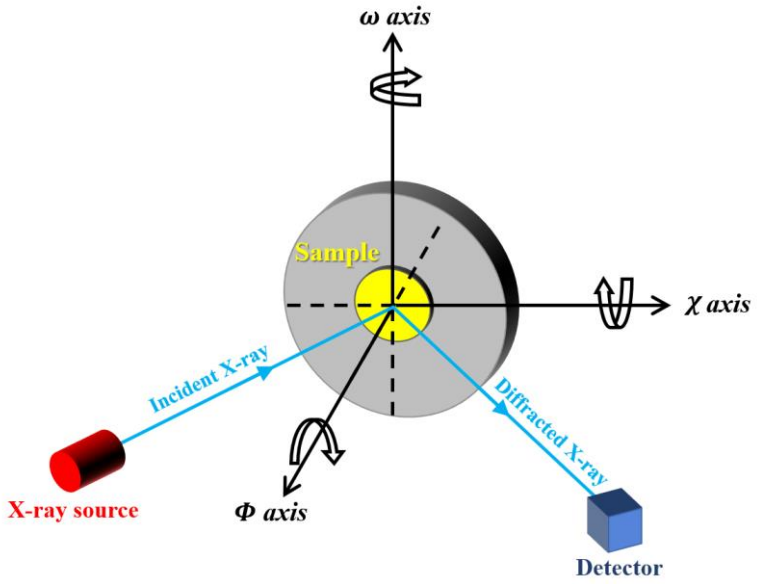

Figure 42: XRD schematic configuration with the most commonly used angles.

In this PhD work, different types of HR-XRD scans were performed in order to extract key information from the grown layers. We mainly performed:

- **ω scan – Rocking Curve (1D scan):**

During this scan, the sample rotates around the ω axis while the detector and incident beam are fixed. The length of the scattering vector S remains constant while changing its direction.

The width of the FWHM of Rocking Curve results give us information on the material properties, such as dislocation density, mosaic spread and curvature.

- **$\omega - 2\theta$ scan (1D scan):**

During this scan, the sample is rotated by an ω angle simultaneously with the 2θ rotation of the detector. This time the scattering vector S keeps the same direction while changing its length. The scan is known as $\omega - 2\theta$ scan since the results are presented with ω on the x-axis. In the case of using 2θ on the x-axis, results will be known as $2\theta - \omega$ scans. For a symmetrical scan, ω = θ.

Using the position of the $\omega - 2\theta$ peaks of InGaN or InAlN layers, one can deduce the interplanar spacing d_{hkl} which is related to the a and c lattice parameters with the following equation: [141]

$$d_{hkl} = \frac{ac\sqrt{3}}{\sqrt{4c^2(h^2+k^2+l^2)+3a^2l^2}} \qquad \textit{Eq. 40}$$

- **Reciprocal Space Mapping (RSM) (2D scan):**

Reciprocal Space Mapping scans are obtained by taking a series of $\omega - 2\theta$ scans at different ω values.

For a graphical representation of an RSM, Reciprocal Lattice Units (RLU) are used. They are defined by:

$$Q_x = \frac{2\pi}{\omega} \times (\cos(\omega) - \cos(2\theta - \omega)) \qquad \textit{Eq. 41}$$

$$Q_z = \frac{2\pi}{\omega} \times (sin(\omega) + sin(2\theta - \omega)) \qquad \textit{Eq. 42}$$

RSM scan are very useful in determining the strain state of a layer on the substrate as they allow the extraction of both the in-plane and out of plane lattice parameter.

In this PhD, HR-XRD measurements were used in order to characterize InAlN and InGaN samples. Samples were analyzed using a XRD3 JV/BRUKER, DELTA-XM tool (cf. Figure 39). Data simulation were processed with JV-RADS software from BRUKER. RSM scans were typically performed on the $(10\bar{1}5)$ asymmetrical reflection planes.

II.6.4 Chemical characterization

II.6.4.1 Secondary Ion Mass Spectrometry

Secondary Ion Mass Spectrometry (SIMS) is a destructive characterization technique, which consists of bombarding the surface of the sample with an ion beam, while analyzing the atoms which are ejected from the surface and then reconstructing the depth profile of each atom species. A CAMECA SIMS SC Ultra 1 tool was used for all the III-N samples studied with SIMS in this manuscript. A schematic diagram of this technique is shown in Figure 43.

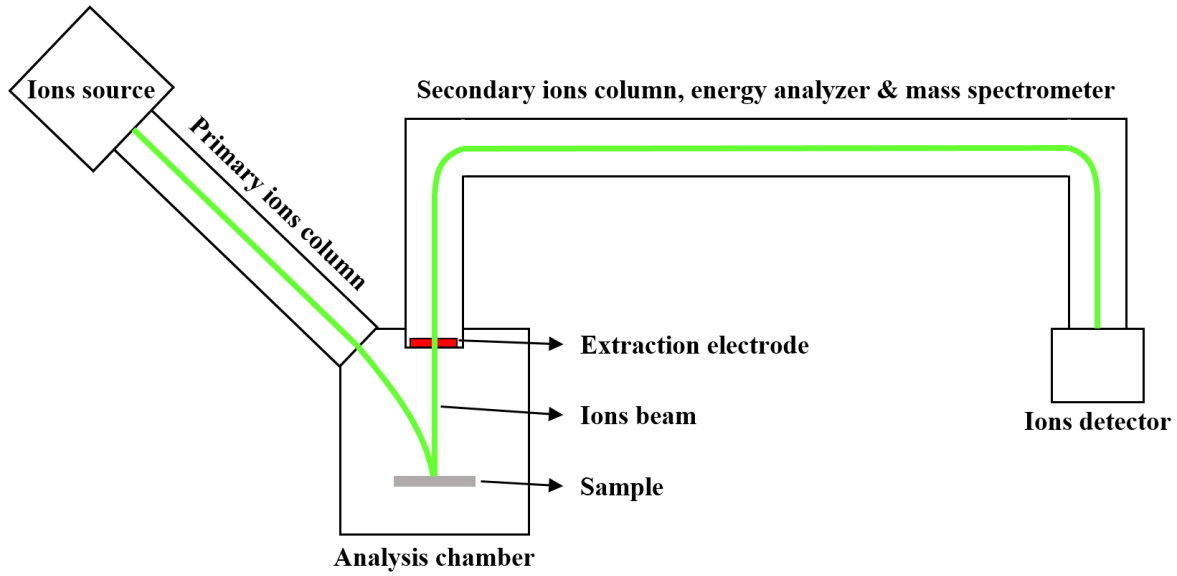

Figure 43: Schematic diagram of the SIMS principle.

The sample is subjected to a continuous primary ion bombardment of a few keV of energy, resulting in a localized atoms sputtering from the surface. Some of the sputtered atoms are ionized. Thus, secondary ions are generated, either in positive or negative state. Ions are sorted by a magnetic field according to the mass/charge ratio, and then recorded using an electron multiplier or a Faraday cage.

Two primary ion sources are available: an oxygen source for O_2^+ ions and a cesium source for Cs^+ ions at energies ranging from 0.150 to 10 keV. The equipment operates under ultra-vacuum conditions (from 10^{-7} to 10^{-10} mbar), provided by a primary pump and secondary pumps (turbo and titanium sublimation). The routing and sorting of primary and

secondary ions is carried out by the use of electrostatic lenses and magnetic sectors in the secondary compartment.

This technique is particularly useful for combining high sensitivity of the order of ppm and ppb with good depth resolution. This is particularly useful for quaternary layers such as InAlGaN, which are complex to analyze by X-ray diffraction. The SIMS quantification of InAlGaN layers was obtained using AlGaN and InGaN reference samples that were already processed and quantified.

II.6.4.2 Plasma Profiling Time of Flight Mass Spectrometry

Plasma Profiling Time of Flight Mass Spectrometry (PP-TOFMS) is a sputtering-based elemental depth profiling technique.

During PP-TOFMS analysis, the sample is bombarded with Ar^+ ions coming from the plasma. The sample is thus pulverized in the form of neutral atoms, which will then be ionized during their diffusion in the plasma. The operating principle of the plasma source is illustrated in Figure 44.

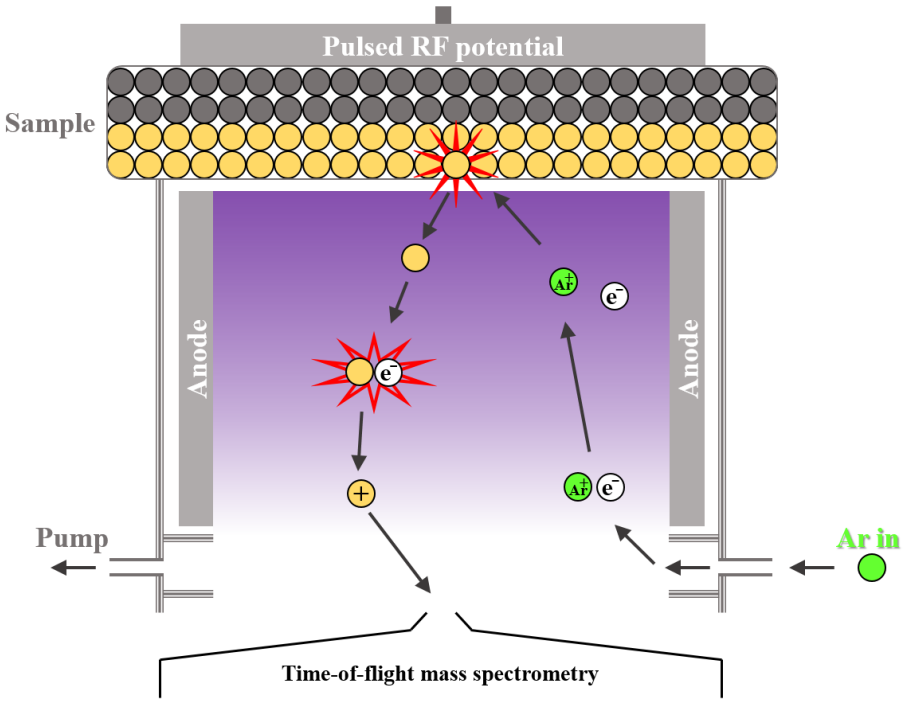

Figure 44: Schematics of glow discharge plasma for depth profiling analysis.

The ions produced in the plasma source are then extracted and guided to the time-of-flight analyzer by differential pumping and ion optics. The process mainly produces monoatomic ions. The molecular ions detected come from recombinations in plasma and not from the sample.

The sensitivity of this tool varies slightly depending on the elements measured and is typically between 10 and 100 ppm. The sensitivity is higher in the case of massive materials such as gallium, aluminum and indium, where the accumulation of signal leads to better statistics. The sensitivity to H, C, N, O, F and Cl is lower than for the other elements.

The depth resolution of such experiment is directly linked to the shape of the sputtered crater. The more the crater has steep sides and a flat bottom, the better the resolution in depth. The plasma conditions (pressure and RF power) determine the shape of the crater, and optimizing plasma conditions typically achieves a resolution of a few nanometers. Due to this restriction, the depth resolution degrades with the analysis depth.

To access quantitative measurements, a calibration phase for the material to be analyzed is necessary. In our case, a reference InAlGaN sample measured with SIMS was used for the calibration of the PP-TOFMS before each measurement.

The sample sputtering speed is high, of the order of a nanometer per second. Unlike SIMS, the vacuum conditions are not very severe, making it possible to analyze our typical III-N layers by PP-TOFMS in less than five minutes. We performed PP-TOFMS measurements on a Jobin1 Horiba Scientific tool (cf. Figure 45).

Figure 45: PP-TOFMS tool: Jobin1 Horiba Scientific.

II.6.5 Electrical characterization

II.6.5.1 Four-Point Probe

In this thesis work, as we are mainly growing GaN based HEMTs heterostructures, a two-dimensional electron gas (2DEG) is formed at the interface between the barrier and the buffer. We carried out Four-Point Probe (4PP) measurements, in order to characterize the 2DEG channel sheet resistance (R_{sh} in Ω/□) on SIAM brand equipment (cf. Figure 46) [142]

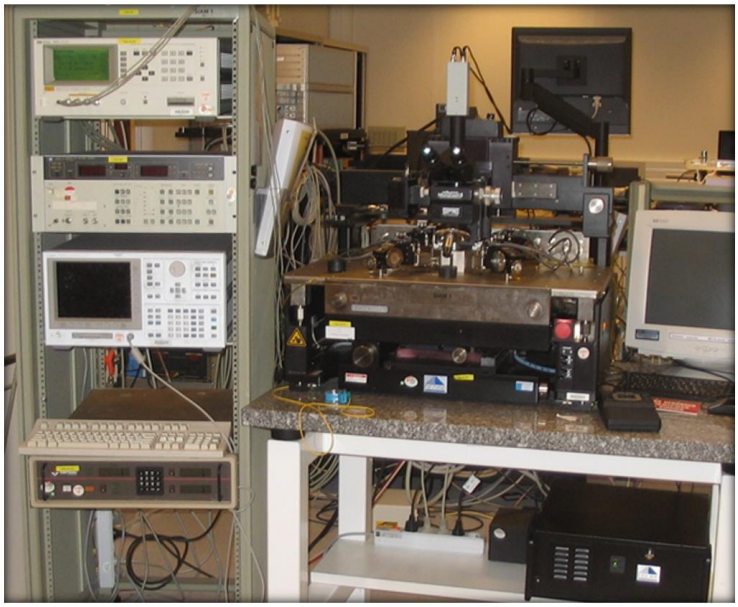

Figure 46: SIAM tool.

This measurement method has been adapted to the characterization of AlGaN/GaN nitride stacks in the work of J. Lehmann [143] and I. Nifa [144]. It requires the creation of a conduction path between the barrier layer and the electrodes, which can be achieved using a high voltage breakdown process. This method allows 2DEG sheet resistance measurements to be made without the need of the deposition of metal contacts.

The 4PP measurement of R_{sh} is based on a voltage measurement device in an infinite half-plane with four electrodes as can be seen in Figure 47. Current I is injected into electrode 1 and extracted by electrode 4. The voltage is then measured between the electrodes 2 and 3.

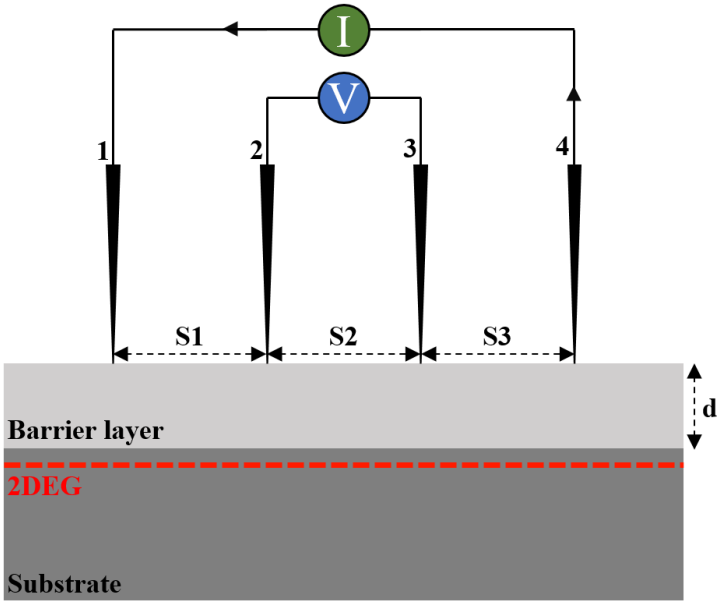

Figure 47: Rsheet measurement setup.

If the electrodes are separated by the same distance, that is to say S1 = S2 = S3 = S, we show that we can obtain an expression of the resistivity r of the layer [143]:

$$r = \frac{V(I)}{I} 2SF\pi \qquad \textit{Eq. 43}$$

Where F is a correction factor, which can be expressed in the measurement of the resistivity of a thin layer of thickness d by the formula:

$$F = \frac{\frac{d}{S}}{2\ln(2)} \qquad \textit{Eq. 44}$$

By combining these two expressions, we therefore get the sheet resistance of the 2DEG:

$$R_{sh} = \frac{r}{d} = \frac{V(I)}{I}\frac{\pi}{\ln(2)} \qquad \textit{Eq. 45}$$

In the case of 4PP measurements on a non-infinite semiconductor surface, the geometrical factor F changes in value [145].

II.7 Summary

In the first part of this chapter, we have explained the basics of the MOVPE growth of GaN. We highlighted some of the important quantities and concepts in such growth technique. In the second part of this chapter, we have shown the MOVPE growth equipment that we used for the growth of our samples, which is the AIXTRON CCS. We mainly discussed the overall tool setup with the bubbler operation and later the in-situ characterizations. In the third part of this chapter we investigated the standard HEMT buffer epitaxial heterostructure used in this PhD work. In the last part of this chapter, we described all the characterization techniques we employed. Namely, morphological optical structural chemical and electrical characterizations.

Chapter III: Understanding Ga contamination in InAlN barrier layers

III.1 Introduction

In chapter 1, we have given the context of the work undertaken during this PhD which is related to the understanding and control of the un-wanted Ga insertion within InAlN barrier layers.

The third chapter of the manuscript is dedicated to the MOVPE growth of InAlN alloys in Close Coupled Showerhead (CCS) AIXTRON reactors. As already mentioned in the first chapter, the production of such layers is gaining much interest especially in the field of power applications and they are considered as a strong competitor for the AlGaN/GaN based HEMT system thanks to their lattice matching on GaN substrates [146] and the benefit of stronger spontaneous polarization [147].

On the other hand, the growth conditions of InAlN are very challenging as the optimal conditions for the growth of AlN and InN are very different. In addition, the growth of such layers in CCS MOVPE reactors in hampered by the non-intentional incorporation of gallium [148, 149, 115, 116, 117]. This is a serious obstacle for the growth of such materials, as it affects the control and the reproducibility of the desired growth recipes, resulting in reduced indium incorporation [118].

To date, several groups have reported the non-intentional incorporation of Ga into InAlN layers and as a result InAlGaN layers were formed, with limited incorporation of indium content and with up to 20% incorporation of gallium [150] [151] [152].

We have previously shown a link between TMIn flow and the incorporated gallium, as shown in Figure 48. We see that for increased TMIn flows during the growth of InAlN, and using different carrier gas (H_2 or N_2), we have a linear increase in the effective TMGa arriving to the barrier layer. This means that the TMIn is correlated to the quantity of Ga in barrier layers. This effect was also reported in [152] in Figure 49, where we see that the increase of TMIn during the growth of InAlGaN was followed by an increase of the nonintentional incorporation of Ga. To the best of our knowledge, our work [153] was the first to investigate systematically the problem of gallium contamination, try to understand it and control it. In the chapter, we also proposed a quantitative model to explain the gallium

contamination behavior based on the hypothesis of the conversion of TMIn to TMGa by reacting with gallium on the showerhead.

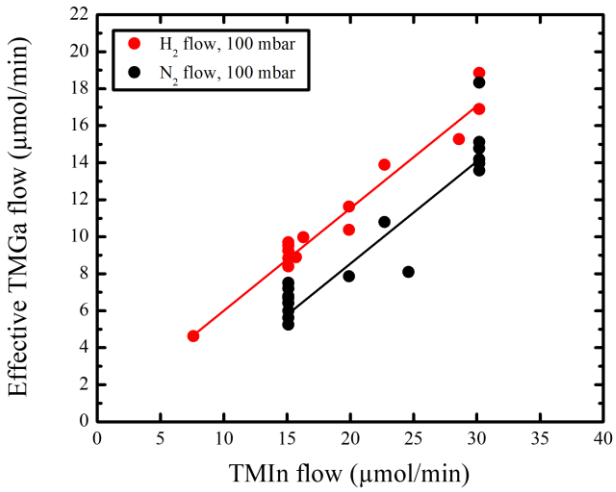

Figure 48: Relationship between effective TMGa generated, and TMIn intentionally flowed into the growth chamber under N_2 and H_2. Data from [150]

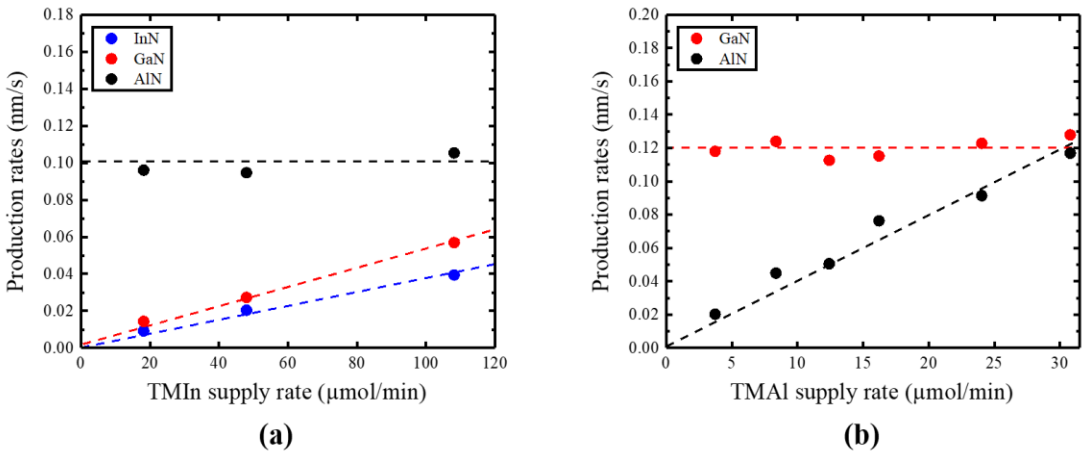

Figure 49: Production rates of InN, AlN, GaN as a function of (a) TMIn and (b) TMAl flow rates. Reproduced from [152]

III.2 Experimental details

In order to understand the undesirable incorporation of Ga into InAlN barriers, we adopted a growth interruption process where several GaN templates were grown without

HEMT active structures before being removed from the AIXTRON tool [158]. The growth chamber is then cleaned, using an in-situ Cl_2 based cleaning, and the growth of the active structures restarted without any GaN coating which might contaminate the InAlN layers.

During this growth interruption, which was typically several days or weeks, the wafers were kept in a cleanroom, exposed to air, as our tool does not allow the wafers to be stored in a pure N_2 environment.

The growth of InAlN barriers directly on GaN surfaces, which have been exposed to oxygen, may affect electrical properties, so we have studied the effect of re-growing a GaN layer before the InAlN barrier layers. Samples were then grown without chamber cleaning between wafers, maintaining the same growth conditions and simply increasing the thickness of the GaN regrowth layer from 0 to 200 nm, before growing the same barrier structure as shown in Figure 50. This allows us to study the effect of increased GaN thickness on the gallium contamination of InAlN layers, and the resulting properties of these structures.

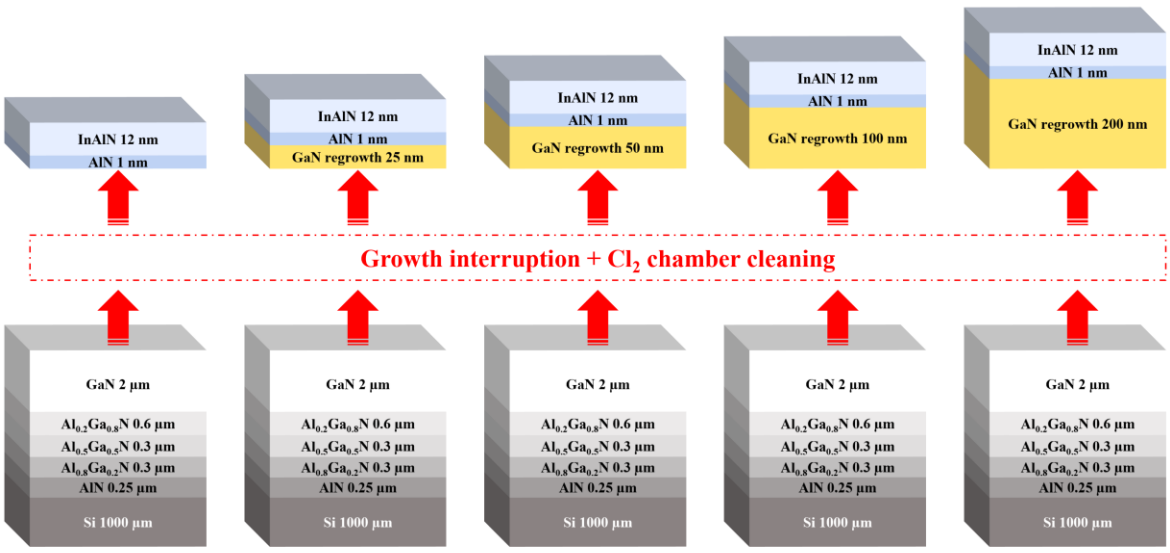

Figure 50: Schematic of growth structures.

As already discussed in chapter 2, the epitaxial growth is performed on 200 mm (111) Si substrates by MOVPE using a fully automated AIXTRON CCS Crius R200 reactor with in-situ chlorine chamber cleaning. The precursors used for the growth of InAlN and GaN were: tri-methylindium (TMIn), tri-methylaluminum (TMAl), tri-methylgallium (TMGa), and ammonia (NH_3) for indium, aluminum, gallium and nitrogen respectively. Growth

pressure and temperature were 100 mbar and 730 ºC respectively. The TMAl and TMIn flows were 30 sccm and 125 sccm respectively, to achieve the 18% indium composition required to be lattice-matched to GaN. Finally the carrier gas was nitrogen (N_2) as it inhibits indium desorption from the growing layers [150], with an ammonia partial pressure of 50 mbar. The epitaxial stack is depicted in Figure 50, and incorporates successive AlGaN layers with decreasing Al composition as necessary for strain engineering when on Si substrates.

As also detailed in chapter 2, samples characterization was performed using Atomic Force Microscopy (AFM), X-Ray Reflectivity (XRR), Secondary-Ion Mass Spectrometry (SIMS), and Wavelength Dispersive X-ray Fluorescence (WDXRF), together with Plasma Profiling Time of Flight Mass Spectrometry (PPTOMS) [154] and finally Four-Point Probe (4PP) [155] to measure the sheet resistance of the grown layer.

III.3 Results and discussion

PP-TOFMS measurements were performed on the set of five samples. For three of the samples, SIMS was also carried out, which allows us to apply a calibration factor to the PP-TOFMS data. Figure 51 shows the SIMS and the calibrated PP-TOFMS data measurements. The calibration factors used for the measurement of the first sample are applied to the 4 other samples. We see good matching for all 3 samples for which SIMS were carried out together with PP-TOFMS, which gives confidence in the measurements.

The results in Figure 51 show the presence of gallium in all of the InAlN barrier layers except for the one which had no GaN regrowth. We also see that unintentionally incorporated gallium in InAlN layers increases as GaN thickness increases, heading towards saturation at 200 nm. We also see that as there is more gallium incorporated into the layers, there is a correlated reduction in indium and aluminum composition, as seen from Figure 52. Values are deduced from Figure 51.

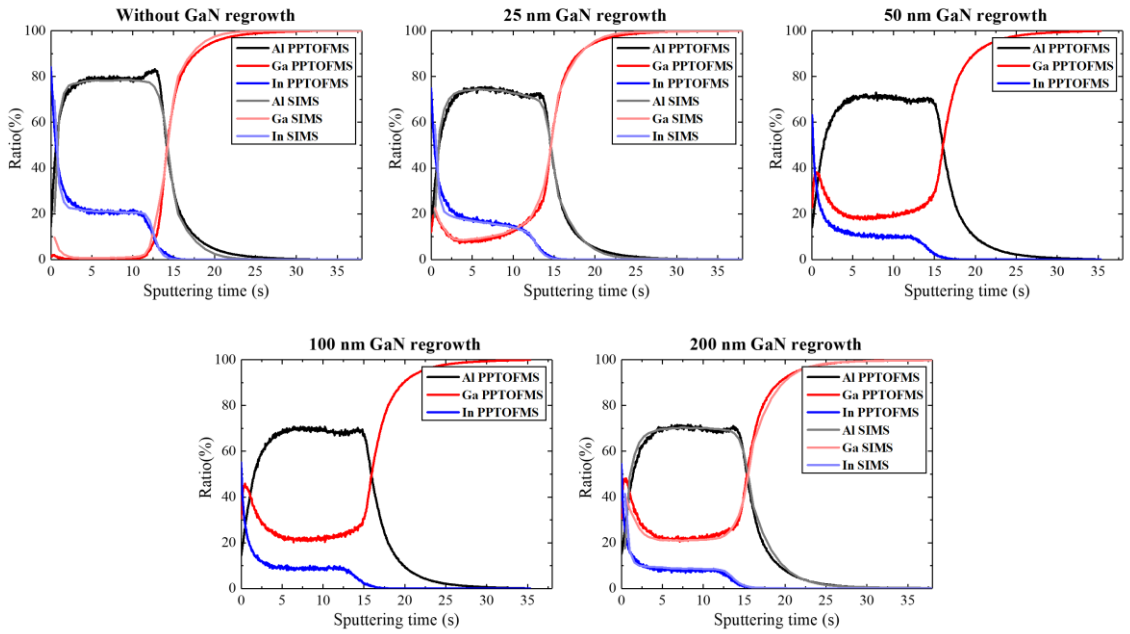

Figure 51: SIMS and calibrated PP-TOFMS measurements for all 5 samples with and without GaN regrowth.

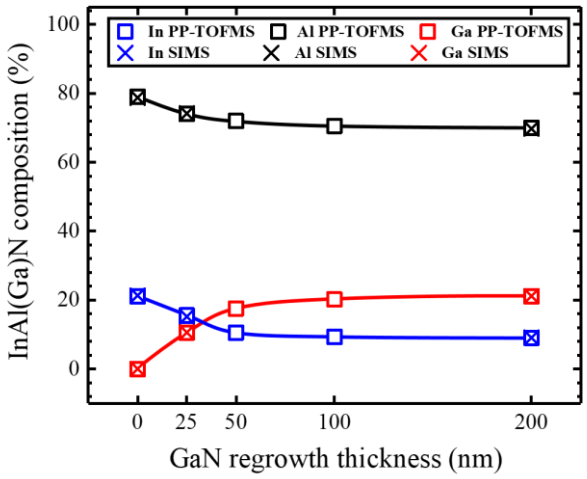

Figure 52: InAl(Ga)N barriers composition of as a function of regrown GaN thickness.

Next, we performed WDXRF measurements on the five samples in order to check the indium and aluminum peak intensity, which should be proportional to the quantity of each element in the layers for such thin layers. It is not possible to analyze the gallium content in the layers, as we are growing on thick GaN buffer layers, which would give a very high intensity of gallium, as WDXRF probes up to 2 µm into the sample.

WDXRF measurements in Figure 53 confirm that the indium content is decreasing with the increase of GaN regrowth thickness, while the quantity of aluminum in the layer stays constant. This is in contrast to the PP-TOFMS and SIMS, which, as shown in Figure 52, seems to indicate that the aluminum composition decreases with increasing GaN regrowth thickness.

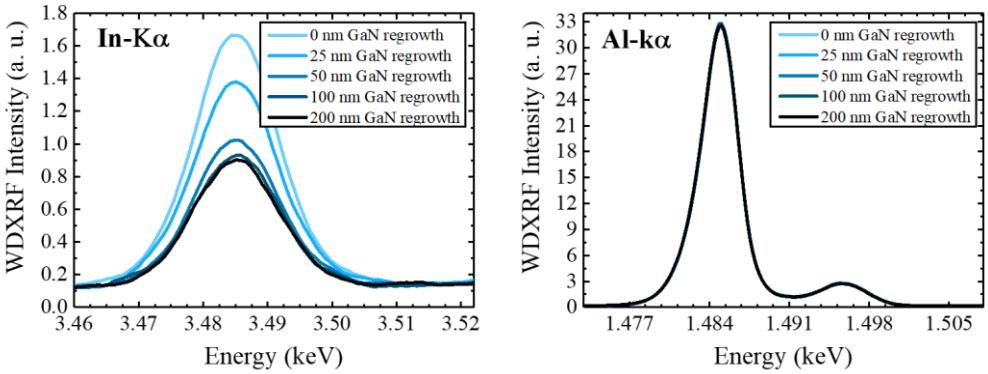

Figure 53: Indium WDXRF peak (left) and aluminum WDXRF peak (right) for all 5 samples.

However, this apparent discrepancy can be explained by the increase in the thickness of the layers as measured by XRR shown in Figure 54. We see that as the percentage of aluminum in the structure decreases, the barrier thickness increases so that the total incorporated mass of aluminum (product = barrier thickness x aluminum composition) stays the same. This implies that the incorporation of Al is not impacted by the GaN regrowth thickness.

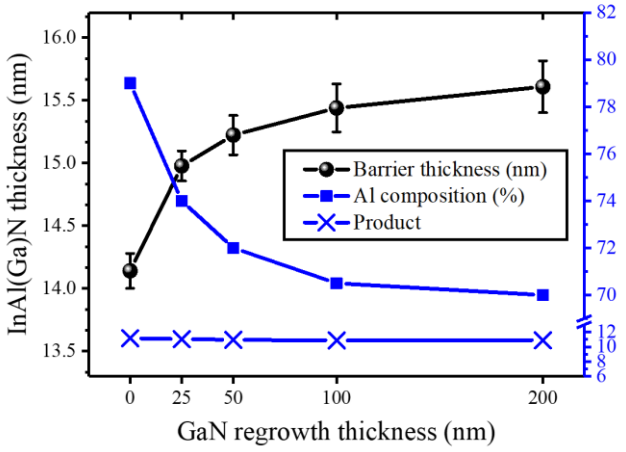

Figure 54: Barrier thickness measured by XRR (black line), Al composition in barrier (blue line/□) and the product (blue line/X): versus GaN regrowth thickness.

If we now combine the thickness measurements with the PP-TOFMS composition data, we can calculate the equivalent incorporated mass of the different III-N binaries into the final InAlN layers as a function of increased GaN regrowth thickness. This is shown in Figure 55. The use of the III-N binaries equivalent incorporated mass gives a clearer view of the effect of the gallium pollution on the final InAlN layer properties.

From Figure 55, we see that the AlN mass remains constant when the GaN regrowth thickness is increased, as we saw in Figure 54, while the InN mass decreases as the mass of GaN increases.

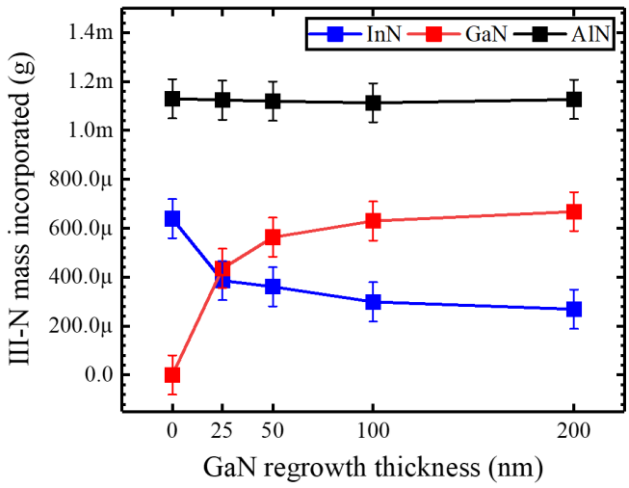

Figure 55: III-N incorporated mass in InAlN layers as a function of GaN regrowth thickness.

Next, we analyzed the surface morphology of the layers. The AFM images in Figure 56 show a slight increase in the layer roughness and the presence of surface cracks with the increase of GaN regrowth thickness above 100 nm. In order to understand such morphological behavior, it is essential to check the strain state of the InAlGaN layers on GaN buffers.

We used Vegard's law to calculate the in-plane lattice parameter of the grown InAlGaN layers:

$$a_{In_xAl_yGa_{1-x-y}N} = x.a_{InN} + y.a_{AlN} + (1-x-y).a_{GaN} \qquad \textit{Eq. 46}$$

Where a_{InN}, a_{AlN} and a_{GaN} are the lattice parameters of InN, AlN and GaN respectively (Cf. chapter 1 for values). x, and y are the indium and the aluminum molar fractions in InAlGaN layers (Cf. Table 8 for values).

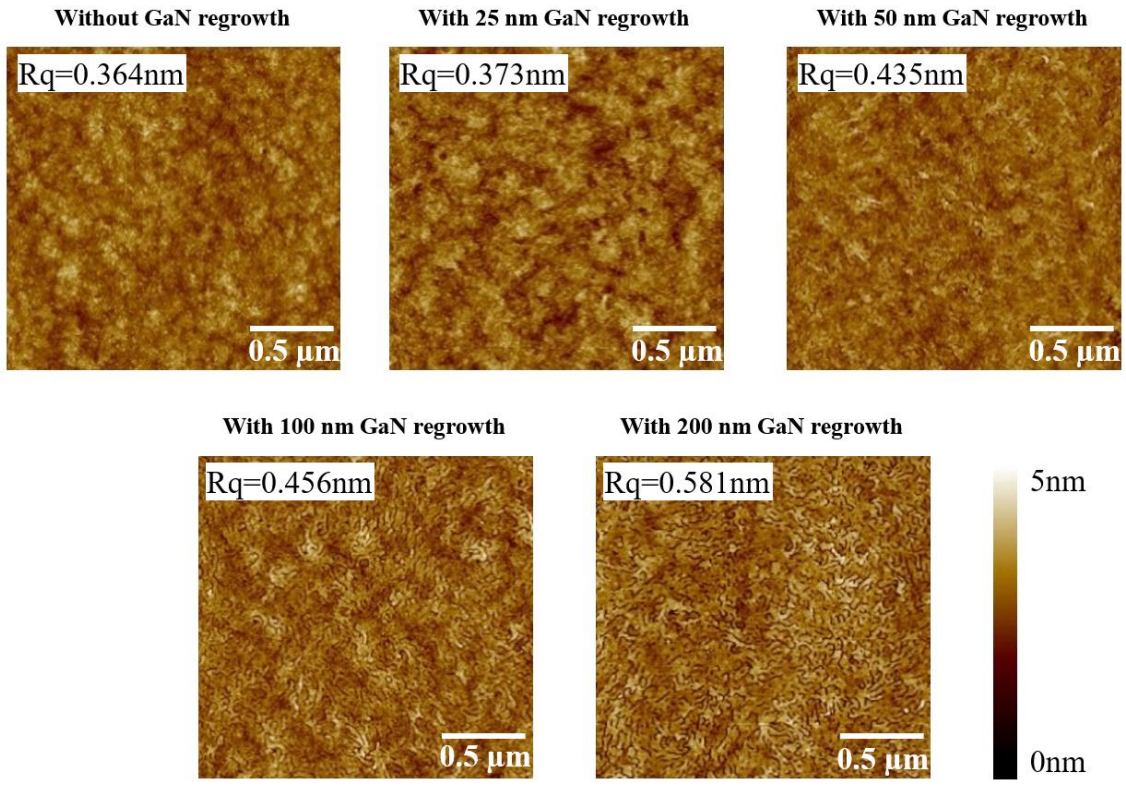

Figure 56: 2µm x 2µm AFM scans of the 5 samples.

Comparing the calculated lattice parameter of InAlGaN barrier layers from Table 8 to that of the relaxed GaN (3.189 Å cf. chapter 1), one can deduce that the sample which had no GaN regrowth is under slight compressive strain. Whereas for increased GaN regrowth thickness, a decrease in the InAlGaN lattice parameter occurs, resulting in tensile stressed material, which explains the presence of cracks.

GaN regrowth thickness	In %	Al %	Ga %	In/(In+Al)	a InAlGaN (Å)
0 nm	**21.1**	**79.0**	**0.0**	**0.21**	**3.203**
25 nm	**15.5**	**74.2**	**10.5**	**0.17**	**3.186**
50 nm	**10.3**	**72.0**	**17.4**	**0.13**	**3.170**
100 nm	**9.3**	**70.4**	**20.3**	**0.12**	**3.167**
200 nm	**9.2**	**70.2**	**21.1**	**0.12**	**3.167**

Table 8: InAl(Ga)N barriers composition and lattice parameter of as a function of overgrown GaN thickness.

We can see from the analysis above that the InAlN layers have an increased gallium contamination with increased GaN regrowth thickness, and that as the gallium contamination increases, we have a reduction in indium incorporation, with no effect on the overall

incorporation of aluminum. We suggest that this gallium contamination comes from gallium-based deposition on the showerhead, a known problem for this chamber architecture [156] [157].

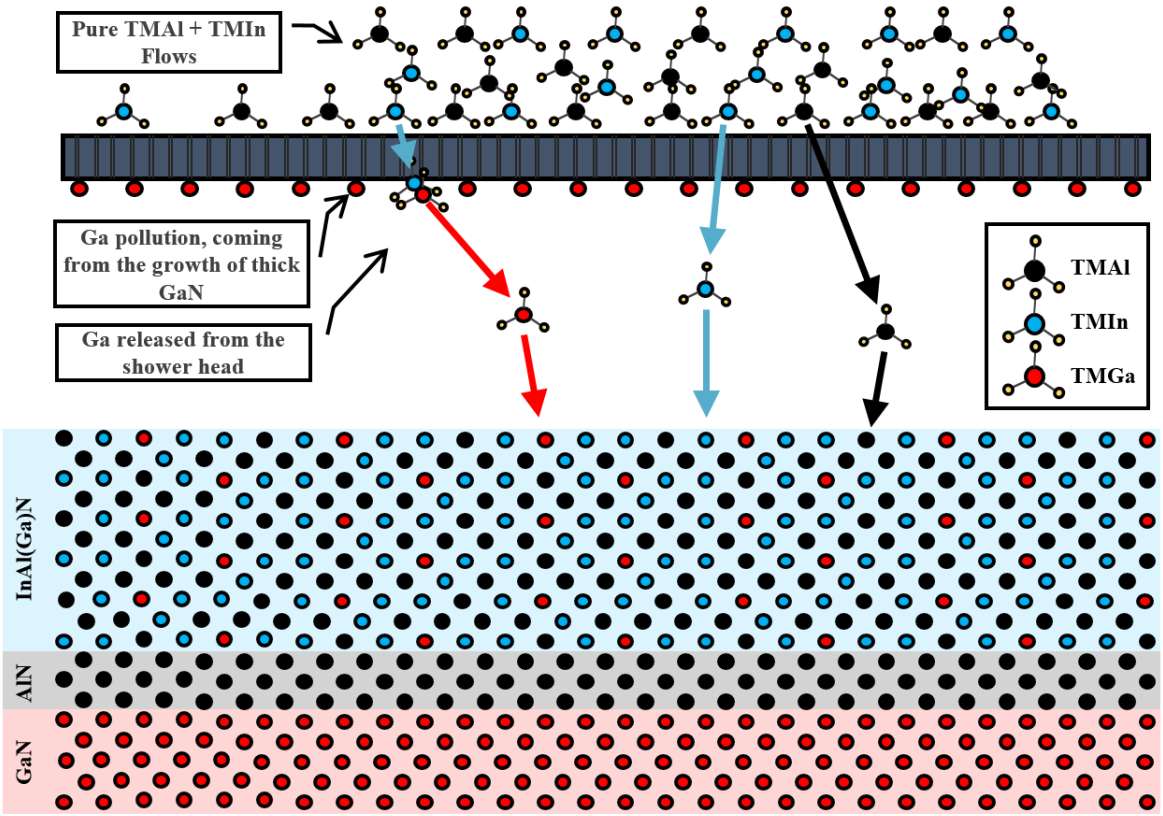

Figure 57: Schematic of proposed gallium contamination mechanism.

Metallic gallium can be found on the showerhead surface [158] as pictured in Figure 57, an illustration of the growth chamber where the TMAl and the TMIn flows are sent through the showerhead holes. We suggest that there is a parasitic chemical reaction taking place between the indium precursor and the metallic gallium, which is also implied by the data in [150] and [152] (Cf. Figure 48 and Figure 49).

According to the following dissociation chemical reactions of the organometallic compounds of TMGa and TMIn in the gas phase [127]:

$$Ga(CH_3)_3 \rightarrow Ga(CH_3)_2 + CH_3 \qquad \Delta G_{dissoc} = +293\ (kJ/mol) \qquad Eq.\ 47$$
$$Ga(CH_3)_2 \rightarrow Ga(CH_3) + CH_3 \qquad \Delta G_{dissoc} = +72\ (kJ/mol) \qquad Eq.\ 48$$
$$Ga(CH_3) \rightarrow Ga + CH_3 \qquad \Delta G_{dissoc} = +164\ (kJ/mol) \qquad Eq.\ 49$$

$In(CH_3)_3 \rightarrow In(CH_3)_2 + CH_3$ $\Delta G_{dissoc} = +267\ (kJ/mol)$ *Eq. 50*

$In(CH_3)_2 \rightarrow In(CH_3) + CH_3$ $\Delta G_{dissoc} = +72\ (kJ/mol)$ *Eq. 51*

$In(CH_3) \rightarrow In + CH_3$ $\Delta G_{dissoc} = +151\ (kJ/mol)$ *Eq. 52*

One can deduce the following reaction:

$TMIn + Ga \rightarrow TMGa + In$ $\Delta G_{dissoc} = -39\ (kJ/mol)$ *Eq. 53*

The free Gibbs energy of this reaction is negative, and therefore the reaction is energetically favorable [127]. These are energetically favorable due to the stronger Ga-C bonds versus the In-C bonds [127]. These reactions would explain why the indium content decreases as the gallium content increases.

This also explains why the effective gallium flow is proportional to the TMIn flow, as seen in [150] and [152] (Cf. Figure 48 and Figure 49). We can consider that each element has an incorporation factor, i.e. the fraction of the molar flow injected into the chamber which is incorporated into the film. This will be noted α_{In}, $\alpha_{Al}$and α_{Ga} respectively for indium, aluminum and gallium incorporation. Then the percentage of indium in the InAlN film with no gallium is:

$$\%In = \frac{TMIn_{flow} \times \alpha_{In}}{TMIn_{flow} \times \alpha_{In} + TMAl_{flow} \times \alpha_{Al}} \quad \textit{Eq. 54}$$

However, according to our hypothesis and in agreement with the previously observed proportionality between the effective Ga flow and the TMIn flow in [150] and [152] (Cf. Figure 48 and Figure 49), a fraction X_{react} of TMIn is converted to TMGa, so the effective Ga and In precursor flows are:

$$TMGa_{eff} = TMIn_{Flow} \times X_{react} \quad \textit{Eq. 55}$$

And,

$$TMIn_{eff} = TMIn_{flow} \times (1 - X_{react}) \quad \textit{Eq. 56}$$

From this, we can see that:

$$\%In = \frac{TMIn_{eff} \times \alpha_{In}}{TMIn_{eff} \times \alpha_{In} + TMAl_{Flow} \times \alpha_{Al} + TMGa_{eff} \times \alpha_{Ga}} \quad \textit{Eq. 57}$$

$$\%Ga = \frac{TMGa_{eff} \times \alpha_{Ga}}{TMIn_{eff} \times \alpha_{In} + TMAl_{Flow} \times \alpha_{Al} + TMGa_{eff} \times \alpha_{Ga}} \quad \textit{Eq. 58}$$

We have calculated the incorporation rates for Al (black) and In (dark blue) as shown in Figure 58, using the following relations:

$$\alpha_{Al} = \frac{Number\ of\ Al\ incorporated\ mols\ (mol)}{Total\ TMAl\ sent\ to\ the\ growth\ chamber\ (mol)} \quad Eq.\ 59$$

$$\alpha_{In} = \frac{Number\ of\ In\ incorporated\ mols\ (mol)}{Total\ TMIn\ sent\ to\ the\ growth\ chamber\ (mol)} \quad Eq.\ 60$$

Whereas:

$$Number\ of\ Al\ incorporated\ mols = \frac{AlN\ occupied\ volume\ (cm^3) \times AlN\ density\ (g/cm^3)}{AlN\ molar\ mass\ (g/mol)} \quad Eq.\ 61$$

$$Number\ of\ In\ incorporated\ mols = \frac{InN\ occupied\ volume\ (cm^3) \times InN\ density\ (g/cm^3)}{InN\ molar\ mass\ (g/mol)} \quad Eq.\ 62$$

Based on XRR and XRD measurements on different spots across the wafers, we know that the InAlGaN barrier layers have approximately a constant thickness and a homogenous composition of In, Al, and Ga across the 200 mm wafer. Using these assumptions, we can calculate α_{Al} and α_{In}.

The incorporation rate for Al is found around 25%, and that of In dropping from 10% to 4% as the GaN regrowth thickness increases. However, we may assume that the incorporation rate of In does not depend upon the thickness of the regrown GaN layer (and thus does not depend upon the amount of metallic Ga on the showerhead). We give it the value of 10% as obtained in the layer without GaN regrowth, we can then calculate X_{react} and α_{Ga}. These are shown in green and red respectively in Figure 58.

We see that we have an incorporation rate of around 25% for Ga, as we saw for Al. As these two elements are not in a growth regime with desorption or pre-reactions, it is logical that the two have similar value and so consolidates the theory. The value of X_{react} then increases with increased GaN regrowth thickness, which could be explained by increased gallium on the showerhead as the GaN regrowth layer becomes thicker.

An alternative explanation could be that the gallium on the showerhead evaporates directly and is incorporated in the layers. However, gallium has a very low vapor pressure at the showerhead temperature (water cooled at 50°C), and so it is not likely to cause direct contamination into the layers.

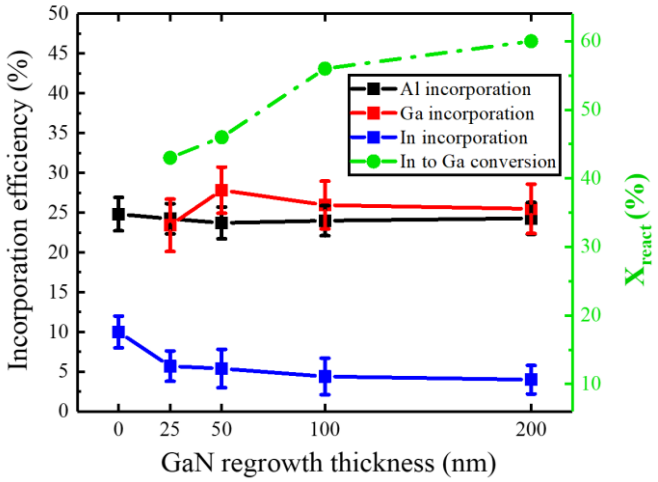

Figure 58: Incorporation rates for Al, Ga and In and X_{react}. X_{react} is calculated for a fixed In incorporation rate of 10%.

Having analyzed the effect of the GaN regrowth layers on the physical and chemical properties of the layers, we then measured the sheet resistance by 4PP, as the objective of these layers is to use them for HEMT based devices.

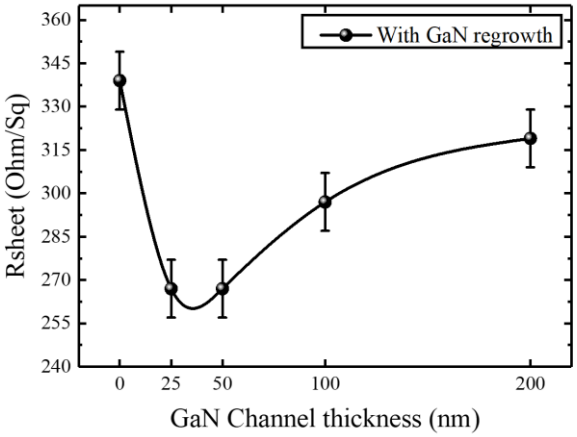

Figure 59: Sheet resistance versus GaN regrowth thickness for HEMT with InAlGaN barrier.

The 2DEG sheet resistance results are shown in Figure 59. The resistance is the highest without any GaN regrowth, but then reduces as we grow a thin layer, before increasing as the GaN regrowth thickness increases further.

In order to explain these electrical results, we calculated the spontaneous and the piezoelectric polarizations of the InAlGaN barrier layers using the following formulas (Cf. chapter 1):

$$P_{sp,In_XAl_YGa_{1-X-Y}N} = P_{sp,InN}X + P_{sp,AlN}Y + P_{sp,GaN}(1 - X - Y) \quad \textit{Eq. 63}$$

$$P_{pe,InAlGaN} = 2\frac{a-a_0}{a_0}\left(e_{31} - e_{33}\left(\frac{C_{13}}{C_{33}}\right)\right) \quad \textit{Eq. 64}$$

Both, spontaneous and piezoelectric polarizations values of our samples are displayed in Table 9.

GaN regrowth thickness	P_{pe} (C.m^{-2})	P_{sp} (C.m^{-2})	Total polarization (C.m^{-2})
0 nm	**-0.0088**	**-0.0707**	**-0.0796**
25 nm	**0.0018**	**-0.0681**	**-0.0663**
50 nm	**0.0108**	**-0.0667**	**-0.0559**
100 nm	**0.0123**	**-0.0659**	**-0.0536**
200 nm	**0.0123**	**-0.0659**	**-0.0536**

Table 9: Calculated spontaneous and piezoelectric polarizations in the InAlGaN barrier layers.

From Figure 60, a visualization of the values presented in Table 9, we see a decrease in the total polarization with the increased GaN regrowth thickness.

The first sample, which had no GaN regrowth, has the strongest total polarization of -0.0796 C.m^{-2}. This contradicts with the poor sheet resistance results shown in Figure 59. One can suggest that the 2DEG channel formed between the InAlN barrier and the GaN buffer is affected by parasitic phenomena associated with the oxidation of the GaN buffer layer before regrowth or other impurity materials or points defects generated at the regrowth interface, resulting in the higher sheet resistance.

For the second sample with the 25 nm GaN regrowth, where an increased distance from the initial regrowth interface to the 2DEG is created, has a better sheet resistance. This is coherent with the strong polarization seen in Figure 60.

Lastly, increasing the GaN regrowth thickness further results in an increase in the 2DEG sheet resistance values. This being most likely due to the change in alloy composition due to gallium contamination and indium reduction, which results in a reduced 2DEG sheet carrier concentration due to the reduced total polarization seen in Figure 60.

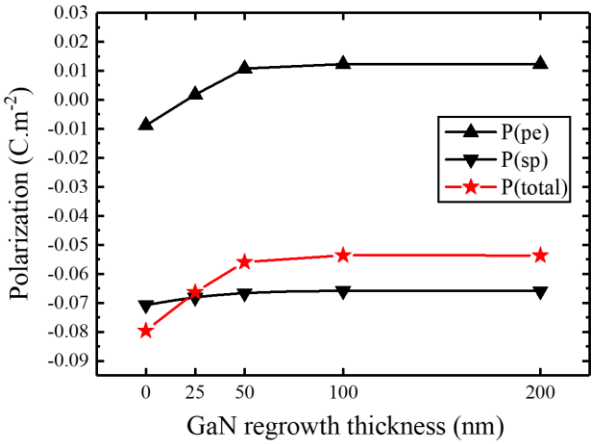

Figure 60: Spontaneous and piezoelectric polarizations of the 5 samples of InAlGaN barrier layers.

III.4 Hydrogen and chlorine etching

As we noticed from the electrical results, removing GaN templates from the growth chamber and exposing them to the clean room environment will introduce impurities to the GaN surface, resulting in poor electrical performance if we regrow InAlN layers directly on top. As described above, regrowing GaN on top of such surface helps to recover a better Rsheet, as long as the deposited thickness is limited to a few 10s of nm. However, the best result from this gave 265 Ohm/sq, when we expect to have lower values for optimized InAlN layers. Using direct regrowth also leads to some gallium pollution which we would like to avoid in order to better control our growth.

The other option is to try to remove the impurities from the GaN template surface. With this in mind, we suggested performing a GaN etch just before growing any active HEMT structure (AlN spacer + InAlN barrier).

Figure 61 shows a typical GaN surface morphology before performing an etch. The surface is smooth with screw and mixed type dislocations seen as holes.

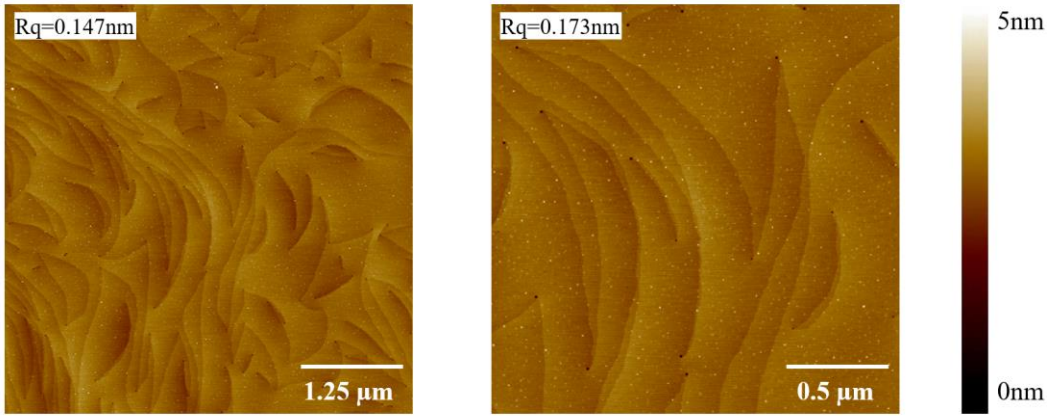

Figure 61: 5µm x 5µm and 2µm x 2µm AFM scans showing a typical GaN surface morphology without etch.

GaN etch tests were performed using either hydrogen or chlorine under the following etching conditions (Cf. Table 10), with etch depth estimated from average values of white light reflectance measurements performed before and after etching:

Etching Type	Etch T (°C)	Etch P (mbar)	Etch depth (nm)	NH_3 Flow (sccm)
Hydrogen	1030	400	40	200
Chlorine	600	100	1 - 10	0

Table 10: Hydrogen and chlorine etching conditions.

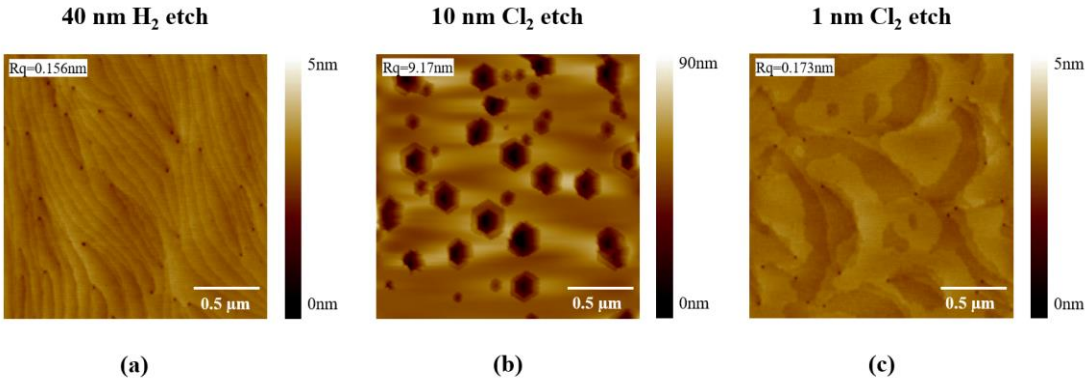

Figure 62: 2µm x 2µm AFM scans showing GaN surface morphology after performing (a) 40 nm H_2 etch, (b) 10 nm Cl_2 etch and (c) 1 nm Cl_2 etch.

Figure 62, shows GaN templates surface morphologies after performing a) 40 nm H_2 etch, b) 10 nm Cl_2 etch and c) 1 nm Cl_2 etch. It is clear that the H_2 etch does not have a strong roughening effect on GaN surface while Cl_2 etch does. Cl_2 etch has a very strong effect even for a etch depth of only 10 nm. This led us to try a less aggressive Cl_2 etch of 1 nm to give a smoother GaN surface. This successfully gave a smoother surface, but the morphology is not typical of GaN layers.

Now as both 40 nm H_2 and 1 nm Cl_2 GaN etched samples have quite a smooth surface with Rq < 0.2 nm, we decided to grow the active InAlN/AlN/GaN HEMT structures on them in addition to a third sample where we have performed only 5 nm H_2 etch. Surface morphologies of these 3 HEMT samples in addition to their barriers compositions are shown in Figure 63.

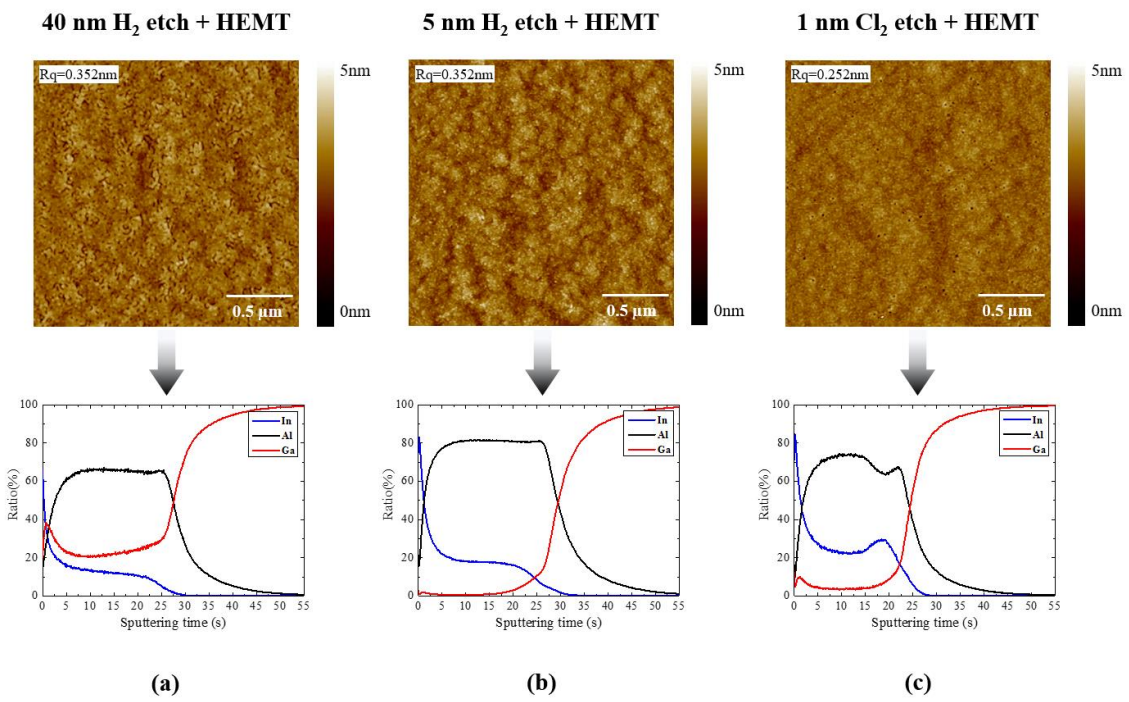

Figure 63: 2µm x 2µm AFM scans with PP-TOFMS measurements of InAlN/AlN/GaN heterostructures showing HEMT surface morphology and barrier composition after performing (a) 40 nm H_2 etch, (b) 5 nm H_2 etch and (c) 1 nm Cl_2 etch.

From Figure 63 we see a smooth AFM surface morphology for the 3 etched samples. For their composition, we notice that sample (a), after performing a 40 nm H_2 etch, has a large amount of gallium of ~20% incorporated into the barrier. This is most likely due to the

metallic deposition of gallium on the shield during the etch process. However, for a smaller H_2 etching depth of 5 nm, in sample (b), we only see ~1% of gallium incorporated into the barrier.

For the last sample, sample (c), where we have performed a 1 nm Cl_2 etch, we see ~5% of gallium incorporated into the barrier. Furthermore, we see an unusual PP-TOFMS profile, where we notice a bump in indium composition with an aluminum bowl profile when we get closer to the GaN etched surface. This is likely due to the wavy GaN surface morphology seen in Figure 62 (c), which is resulting in nonhomogeneous PP-TOFMS sputtering.

Next, in Figure 64, we plotted the Rsheet values for these heterostructures in addition to the previous data from Figure 59.

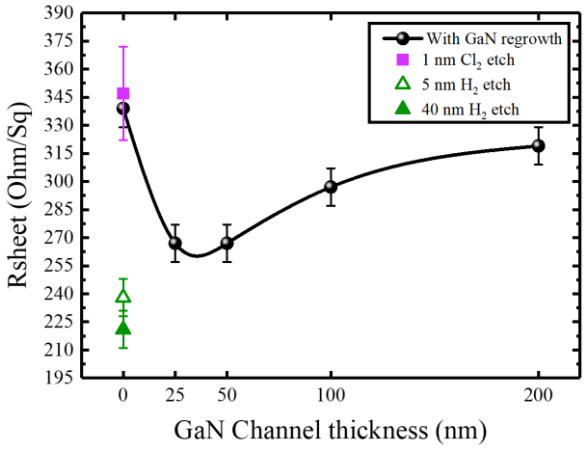

Figure 64: Sheet resistance for InAlN/AlN/GaN HEMT structures for chlorine and hydrogen etched samples compared with GaN regrowth samples.

From this figure, for the sample etched with Cl_2 we do not see any improvement, and this is most likely due to the nonhomogeneous etching performance, despite the good Rq. For the samples with H_2 etch however, we see an improvement in the electrical performance. We reached low Rsheet values of ~220 Ω/sq for samples etched with H_2 compared to GaN regrowth samples where the best sheet resistance value is 270 Ω/sq. This is thanks to the etching process where impurities are removed from the GaN surface.

III.5 Post-etch pure InAlN barrier layers growth

As we can see from the previous section, the smooth 5 nm H_2 etch of GaN buffers, allowed us to grow pure InAlN barrier layers with very low gallium pollution (less than 1%), smooth surface morphology, and good Rsheet results.

Indeed, this result can be considered to have achieved one of the main goals in this PhD work. Thus, we decided to use the 5 nm H_2 etch process to further optimize the InAlN HEMTs. We started by growing InAlN barrier layers with different In% just after performing a growth interruption followed by a chlorine chamber cleaning and then performing a 5 nm H_2 etch of the GaN before the growth of the active HEMT structure. Changing the In% in InAlN barriers was intended to provide us with more information on the electrical, chemical and morphological behaviors of such ternary when grown on GaN.

We grew 5 samples of InAlN with In% varying from 12% to 24% as shown in Figure 65. InAlN growth pressure and temperature were 100 mbar and 730 ºC respectively, as for previous samples.

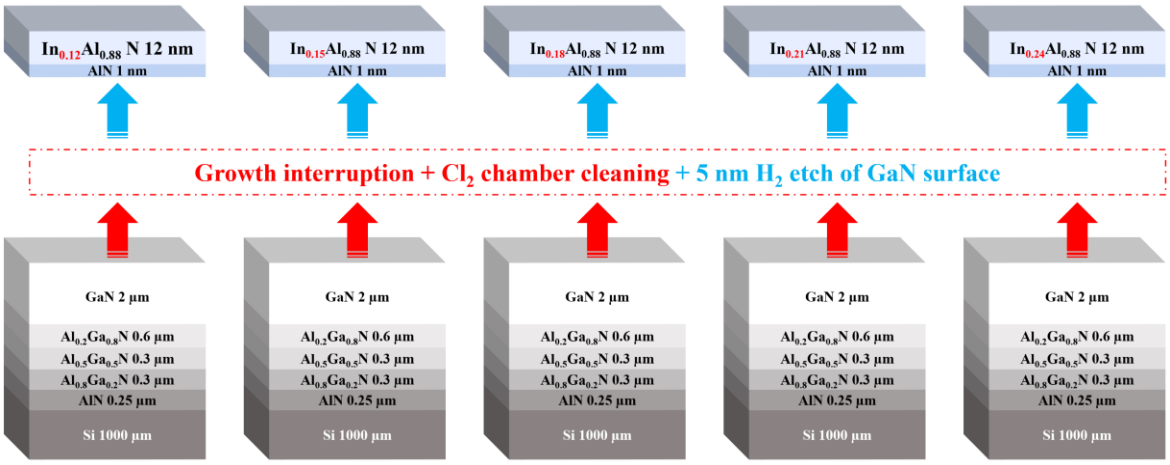

Figure 65: Schematic of growth structures of InAlN barrier layers with different In%. Growth is carried out on the GaN template after a growth intrerruption followed by Cl_2 chamber cleaning and 5 nm H_2 etch.

We varied the TMIn and TMAl flows (Cf. Table 11) during the growth of the 5 samples in order to keep the same growth rate and barrier thickness for all samples. As we can see

from the XRR analysis of the barrier thickness in Figure 66, we succeeded in this, with a near constant barrier thickness of around 12.5 nm across all the grown barriers.

Nominal In% in samples	TMIn (sccm)	TMAl (sccm)
12	82	33
15	100	31.4
18	125	30
21	143	29.7
24	164	28.5

Table 11: TMIn and TMAl flow values used for the growth of InAlN barriers with different In%..

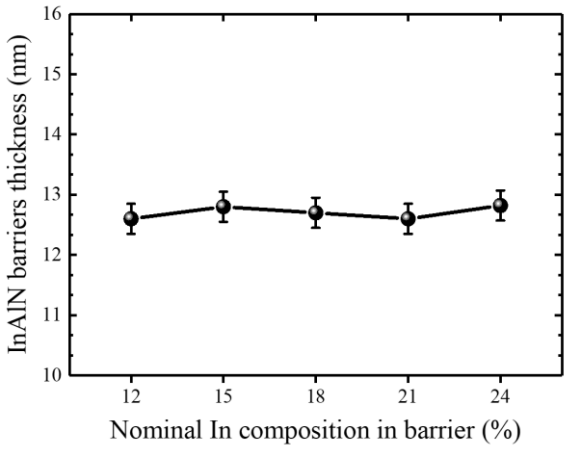

Figure 66: InAlN Barrier thickness measured by XRR for different nominal In compositions .

The barrier composition was analyzed using PP-TOFMS, as shown in Figure 67. As mentioned earlier this technique is calibrated with SIMS measurements, which gives confidence in the displayed In%.

From the PP-TOFMS measurements, we see that the real compositions of barriers are very close to the nominal ones. Secondly, we notice that Ga pollution is around 1% in all barriers, thanks to the etch process which helped in removing surface impurities and limiting the presence of gallium in layers which was up to 20 % whenever we performed a GaN growth beforehand.

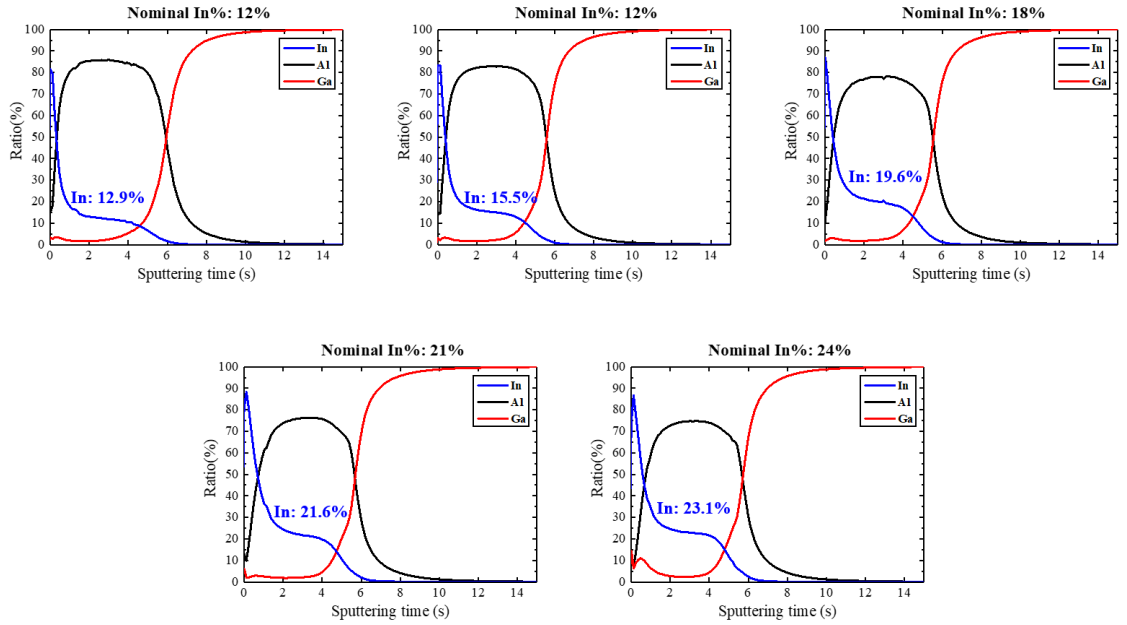

Figure 67: calibrated PP-TOFMS measurements for all 5 InAlN samples.

We also examined the surface morphology of InAlN barriers with AFM measurements, as shown in Figure 68.

All samples have similar surface morphology with the presence of small holes or cracks. It is unclear why we have this morphology, as if they were strain cracks, we would expect to have a much higher density for the lowest indium content samples. The RMS also stays roughly constant for all the samples.

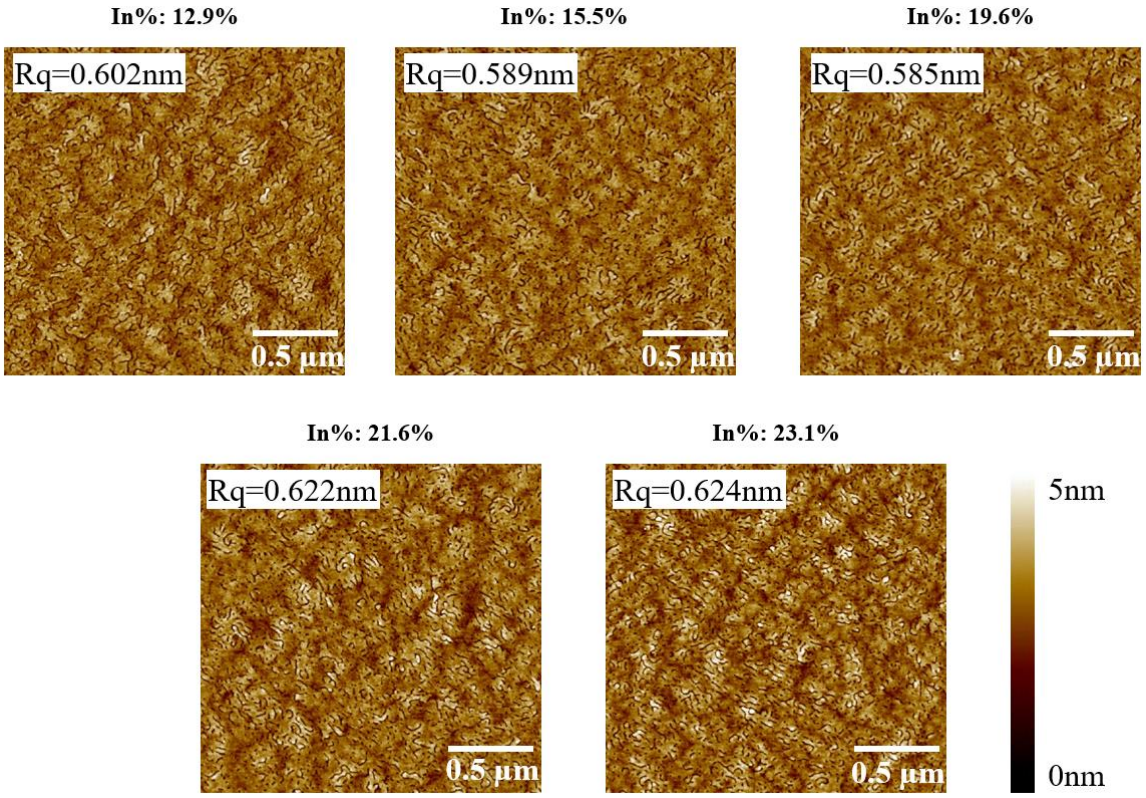

Figure 68: 2µm x 2µm AFM scans of all InAlN barrier layers with different In%.

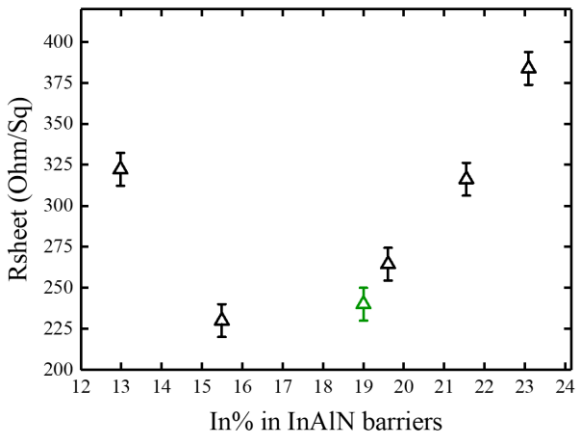

Figure 69: Rsheet measurements of the 5 InAlN samples grown onto 5nm H_2 etched GaN templates with different In% (in black) and in green the first 5 nm H_2 etched sample that we have shown in Figure 63 (b).

Lastly, we checked the electrical performance of these layers with 4PP measurements, as shown in Figure 69. It is clear from this figure that the best Rsheet values are for samples

having an In% of between 15% and 18%, e.g. for nearly lattice matched layers. Otherwise, we notice a drop in the electrical performance for either compressive or strongly tensile strained layers.

From these etching experiments and the changes in In% in layers, we can also note that we managed to get high In% in InAlN layer of ~24%. This was not the case when gallium pollution was present in the growth chamber, which was limiting the incorporation of indium into the layers. Thus, here, we should be able to increase the growth temperature during the growth of InAlN barrier layers in order improve the InAlN material quality, while still maintaining high indium content in the layers. This was expected to lead to an improvement in the electrical performance.

Thus, we grew 3 samples of InAlN barrier layers at a higher temperature of 830 °C instead of 730°C but always with the same pressure of 100 mbar. This higher temperature should decrease the growth rate of InN component due to the evaporation of indium, so we increased the TMIn flow from 125 sccm to 250 sccm to 375 sccm. With gallium pollution this would have been expected to increase significantly the gallium incorporation as well, but growing in a clean chamber allows us to get around this problem.

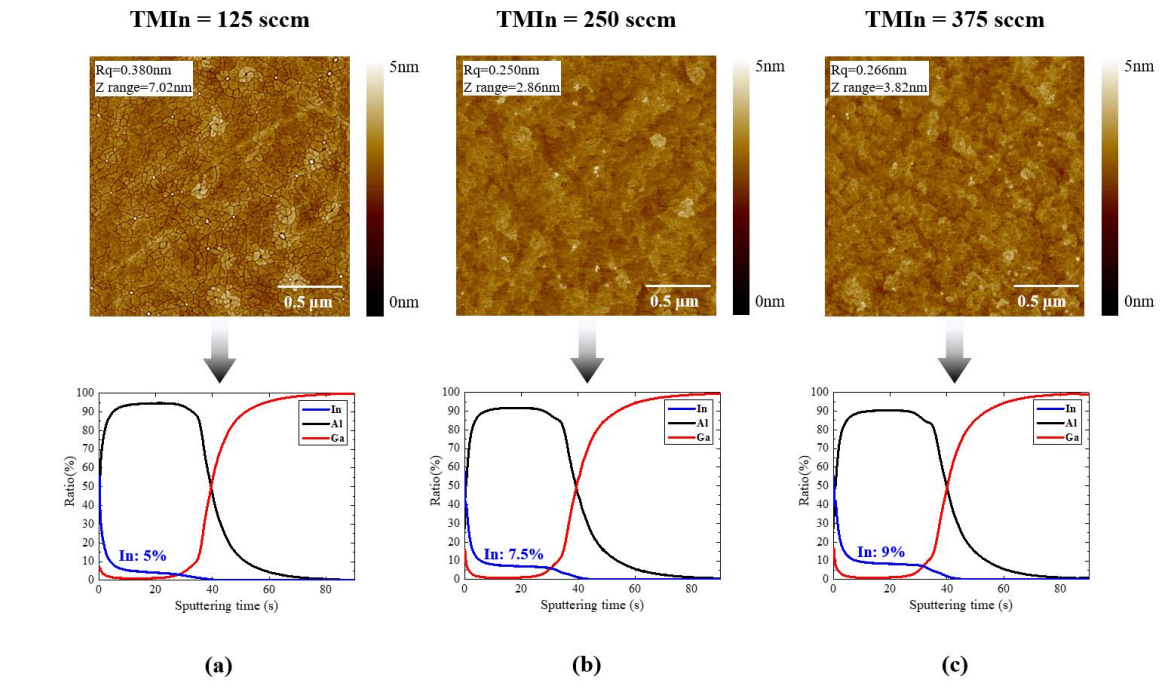

Figure 70: 2µm x 2µm AFM scans with PP-TOFMS measurements of InAlN/AlN/GaN heterostructures with different TMIn growth flows.

We examined both the surface morphology and the barrier composition of the 3 layers, as shown in Figure 70. For the lowest TMIn value of 125 sccm, we see cracks across the surface with high Z range, explained by the very low indium incorporation of 5% seen with the PP-TOFMS measurements. For higher TMIn flows of 250 and 375 sccm, we see a better AFM surface morphology with lower RMS and lower Z range. This is associated with the higher incorporation of indium.

Checking the electrical performance of these samples with 4PP technique as shown in Figure 71 (blue points), we see a clear drop to excellent Rsheet values of around 185 Ω/sq for sample grown with 250 and 375 sccm of TMIn flow. This huge improvement in the electrical performance of such layers is most likely due to good InAlN material quality that we grew at 830 °C. Unlike for the growth at 730°C, we have very good performance with low indium contents, which has not yet been fully understood. This may be due to the very smooth surface of the films, and the absence of cracks or holes in the layers.

However, for the high temperature sample with low TMIn flow of 125 sccm, we see a huge increase in the Rsheet value, indicating poor electrical performance. This is most likely due to the material and surface quality seen with the AFM images, where we have seen cracks and a high Z range.

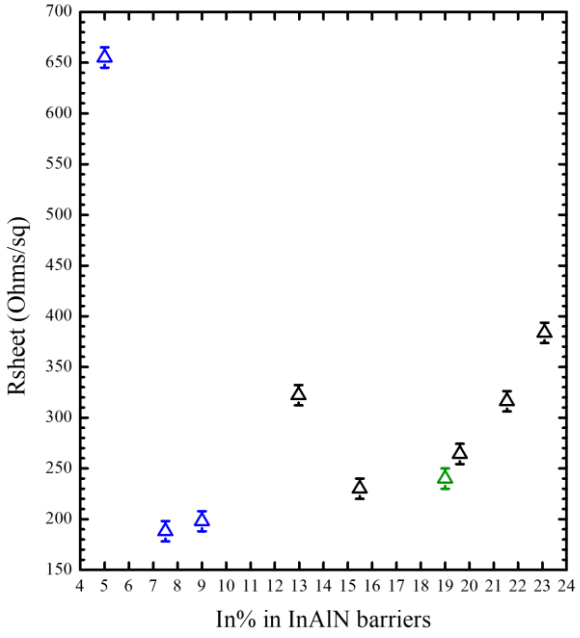

Figure 71: Rsheet measurements in function of In% for all etched samples. Blue, black and green points correspond to the samples shown in Figure 70, Figure 68, and Figure 63 (b) respectively.

III.6 Conclusion

We have shown in this chapter, that in our showerhead MOVPE system, InAlN layers are contaminated with gallium, giving increasing contamination with thicker GaN regrowth layers. We have also shown reduced indium in the layers and thicker layers as the gallium contamination increases. We proposed a quantitative model for these observations, suggesting that the TMIn precursor reacts with gallium on the showerhead surface to release TMGa, which is then incorporated as Ga into the layers.

For the InAlN barrier layers for HEMTs grown directly on a template, or after 25 nm of GaN, the 2DEG was degraded by the regrowth interface. However, for thicker layers of GaN, there was a strong gallium contamination. This led to acceptable Rsheet values of 270 Ω/sq and low gallium contamination. This shows the possibility of using regrowth of InAlN structures in a showerhead reactor to produce low resistance, and relatively gallium-free InAlN based HEMTs.

Pushing this work further, we also have shown the interest of performing GaN etching process, in order to remove the impurities introduced from the growth interruption step. By performing the same growth, we reduced the Rsheet to 220 Ohm/sq, showing effective removal of impurities. By increasing the temperature, a step which is not possible with gallium pollution, we then managed to grow smooth InAlN barriers with RMS < 0.25 nm and a gallium incorporation of less than 1% resulting in Rsheet values of around 185 Ω/sq close to the state of the art shown in chapter 1.

Chapter IV: Understanding Ga contamination in InGaN layers

IV.1 Introduction

The fourth chapter of the manuscript is dedicated to the MOVPE growth of InGaN alloys in Close Coupled Showerhead (CCS) AIXTRON reactors [159]. These ternary alloys have attracted a lot of attention, since the active zone of light-emitting diodes (LEDs) and lasers is comprised of InGaN quantum wells. In these structures, that potentially cover the near UV to visible range [160] [161] [162] [163] [164], controlling the emission wavelength requires a precise monitoring of the In concentration and of the quantum well thickness, especially in the successive quantum wells as used in most emissive structures [165] [166] [167].

It is well known that the In composition in InGaN alloys and their thickness together with their structural and optical properties can be significantly affected by growth conditions such as temperature, pressure, indium to gallium ratio, and many other parameters [160] [168].

In this chapter, we decided to investigate the effect of gallium pollution in CCS reactors, the known problem for this chamber architecture on the growth of InAlN [157] [156] [150] [169] [170]. As we reported in the previous chapter, the unwanted incorporation of Ga is critical for the growth of InAlN barrier layers for HEMT applications [171].

Although InGaN layers already have intentional gallium incorporated into the layers, possible gallium pollution makes understanding and controlling the growth non-trivial. Therefore, in this chapter, we will be examining in detail the effect of this Ga pollution on the growth of InGaN epilayers.

IV.2 Experimental details

This study approached the study of InGaN layers in the same manner as that which we already performed on InAlN layers, and samples were grown on 200 mm (111) Si substrates by MOVPE using the same AIXTRON CCS Crius R200 reactor.

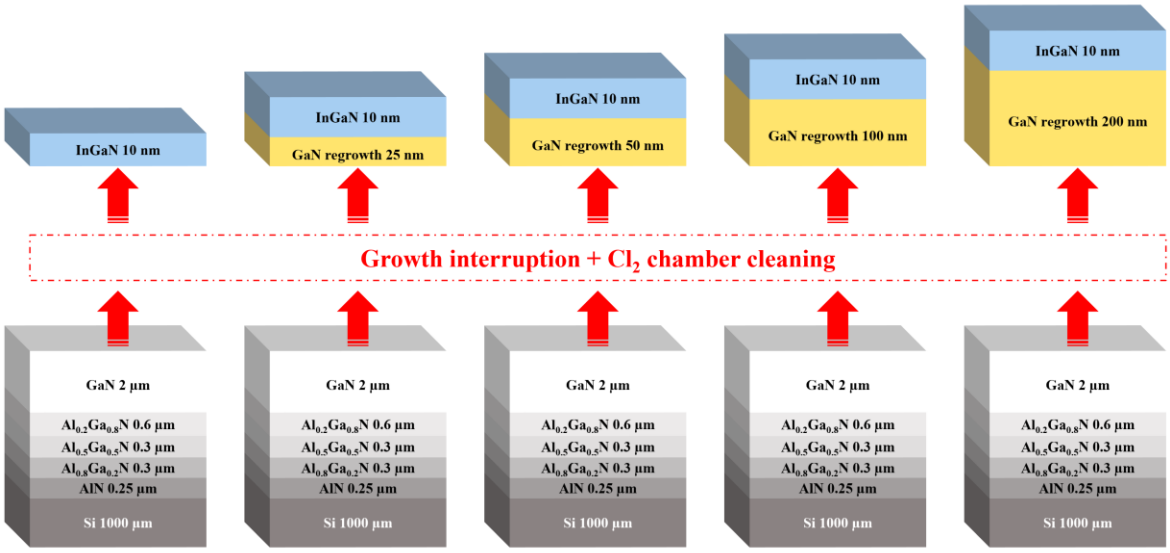

Figure 72: Schematic of growth structures.

As we can see from Figure 72, after the growth of the 2 µm thick GaN buffer layers, there was a growth interruption followed by a regrowth step of the top layers consisting of GaN layers with thickness ranging from 0 nm up to 200 nm and then 10 nm of InGaN.

During the growth interruption, a chlorine based clean of the chamber was performed, in order to remove any residual metallic gallium from the growth chamber. The GaN templates were removed from the growth chamber during this interruption, and kept in a cleanroom, exposed to air, as our tool does not allow the wafers to be stored in a pure N_2 environment. The regrowth step of the top GaN and InGaN layers was performed some days or weeks after the initial buffer growth, directly after the chlorine based chamber clean.

The epitaxial structures of our samples consist of three AlGaN layers with increasing Ga content in the buffer as explained in chapter 2. For certain samples, only the $Al_{0.5}Ga_{0.5}N$ and $A_{0.2}Ga_{0.8}N$ buffer layers were used due to the availability of these template structures. This does not change the strain state of the GaN, and so it is not expected that this would have an impact on the growth of InGaN layers. Nitrogen (N_2) was the carrier gas for all InGaN samples, as it inhibits indium desorption from the growing layers [150].

IV.3 Results and discussion

For the initial study, we grew two sets (sample sets A and B) of InGaN layers with the same growth conditions as those used for InAlN growth. The intention was to directly compare the MOVPE growth behavior of InGaN and InAlN, examining the effect of Ga pollution in the growth chamber, even though these are not optimal growth conditions for InGaN layers. We used tri-methylgallium (TMGa) and tri-ethylgallium (TEGa) precursors respectively for set A and set B, instead of tri-methylaluminum (TMAl), as we are growing InGaN material, while maintaining the same TMIn flow. We note that the use of TEGa limits the incorporation of carbon impurities in InGaN layers. However, TEGa is also more likely to be involved in parasitic reactions compared to TMGa, resulting in lower InGaN growth rate. The growth details are shown in Table 12.

Growth sets	T (°C)	P (mbar)	TMAl (µmol/ min)	TMGa (µmol/ min)	TEGa (µmol/ min)	TMIn (µmol/ min)	Growth Time (s)
InAlN [171]	730	100	26.6	-	-	9.9	315
InGaN Set A	730	100	-	21.6	-	9.9	315
InGaN Set B	730	100	-	-	21.6	9.9	315
InGaN Set C	760	400	-	7.4	-	31.8 (400 sccm)	540
InGaN Set D	760	400	-	7.4	-	3.9 (50 sccm)	540
	760	400	-	7.4	-	7.9 (100 sccm)	540
	760	400	-	7.4	-	15.9 (200 sccm)	540
	760	400	-	7.4	-	47.7 (600 sccm)	540

Table 12: InGaN and InAlN MOVPE growth conditions for samples grown in clean and gallium polluted chamber.

For sets A and B, we grew two samples with each set of conditions. One with the InGaN growth started directly on the GaN template after the reactor had been cleaned with chlorine, and another after 200 nm of GaN was regrown on the template before the InGaN layers.

We investigated the InGaN layers composition and thickness of these samples, using HRXRD. From reciprocal space maps (RSMs) around the (114) peak, shown in Figure 73, we see that the InGaN layers appear strained on the GaN, and so can be simulated from ω-2θ scans. Figure 74 shows clear thickness fringes on the ω-2θ scans around the (0002) reflection. These allow good simulation and therefore we can easily extract the properties of the InGaN layers. For set A with TMGa the fringes are lost in the background noise after -4000 arc-seconds, while for set B with TEGa, the fringes are visible up to -8000 arc-seconds.

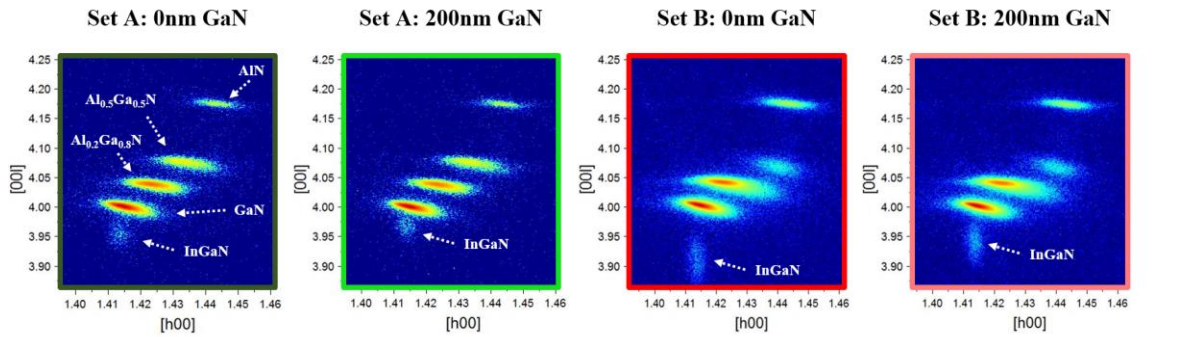

Figure 73: RSM (114) measurements of set A (TMGa as Ga source) and set B (TEGa as Ga source)samples.

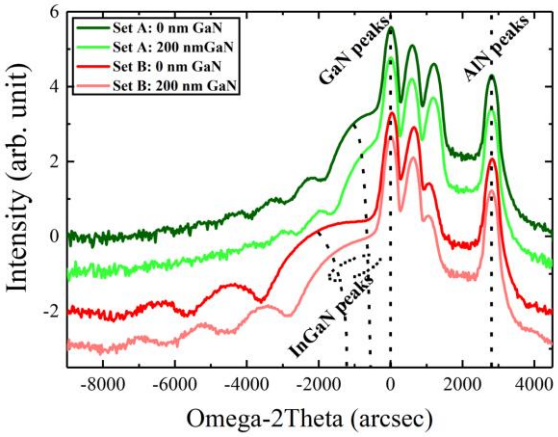

Figure 74: XRD ω-2θ measurements of set A (green) and B (red).

The HRXRD results shown in Figure 74 are coherent with the AFM measurements shown in Figure 75, where we see that the layers with TMGa in set A are rougher.

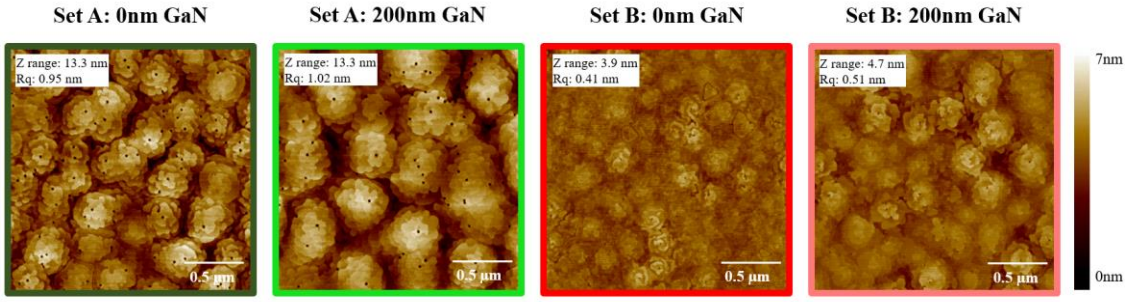

Figure 75: 2µm x 2µm AFM scans of set A (TMGa as Ga source) and B (TEGa as Ga source).

The overall InGaN morphology exhibits step flow islands with V-pits. This is a common morphology for low-temperature growth of GaN and its alloys [150, 172], due to the limited mobility of the deposited atoms. V-pit density was calculated to be 1-3 x 10^9 cm^{-2} with a diameter size of about 20-40 nm, coherent with the dislocation density.

Additionally, LT-PL measurements were performed on these samples, whose spectra are shown in Figure 76.

To extract the composition of the InGaN layers from the LT-PL measurements in Figure 76, we used the following equation:

$$E_g(InGaN) = xE_g(InN) + (1-x)E_g(GaN) - bx(1-x) \qquad Eq.\ 65$$

Where Eg(InGaN), Eg(InN) = 0.7 eV [134], and Eg(GaN) = 3.39 eV [135] are the band gap energies of InGaN (taken from LT-PL fitted peaks data), InN and GaN respectively. x is the indium molar fraction in InGaN layers, and b is the bowing parameter accounting for the nonlinearity of the InGaN band gap with composition. We used a bowing parameter of 1.204 eV using the following equation:

$$b^{(strained)} = 1.154 * E_g^{InN} + 0.396 \quad [136] \qquad Eq.\ 66$$

The bowing parameter shown in *Eq. 66*, is appropriate for thin strained InGaN layers with low In%, which is our case, as we previously saw in Figure 73.

Thus, the bowing parameter shown in *Eq. 66* fits very well with the properties of our layers, since we are growing strained InGaN layers with low In% (lower than 15%) and thicknesses inferior to the theoretical critical thickness (inferior to 25 nm) for plastic deformation as deduced from the model of Fischer et al. [136] [137]

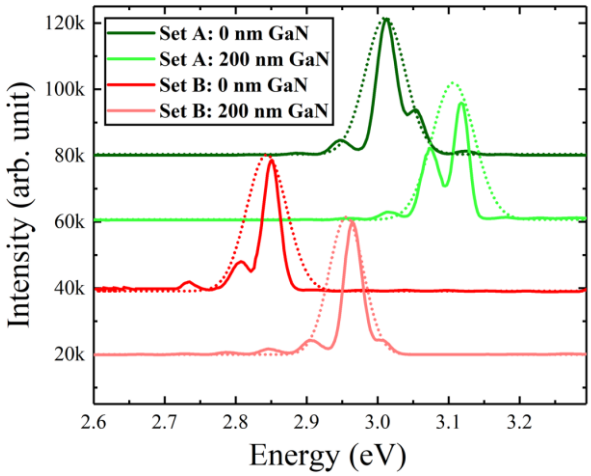

Figure 76: LT-PL spectra: InGaN normalized intensity as a function of photon energy at 6K (solid lines) and the fitted data (dash lines).

Using the XRD data from Figure 74 and the PL data from Figure 76, we extracted the thickness and the In% of the InGaN layers as shown in Figure 77.

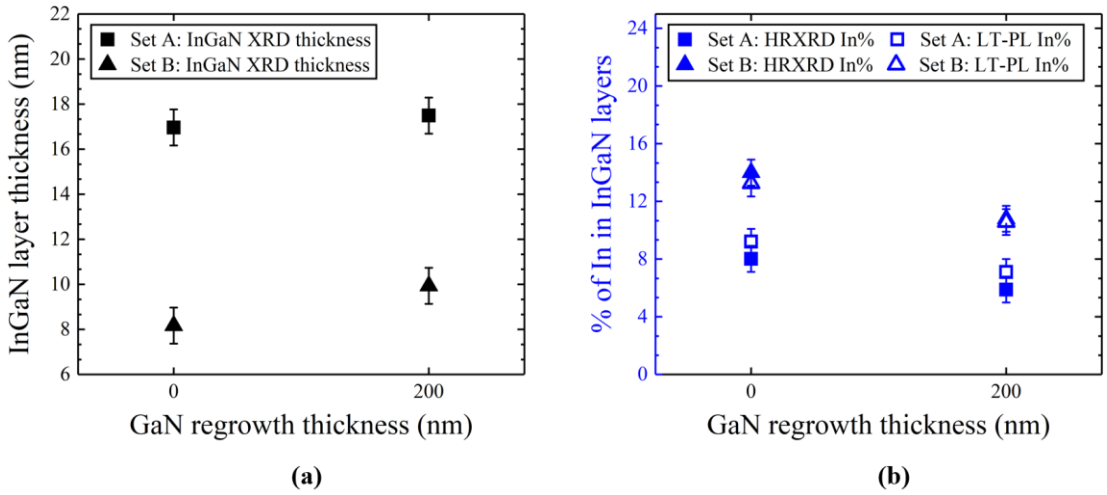

Figure 77: a) InGaN layers thickness of set A and B deduced from XRD. B) In% in InGaN layers of set A and B deduced from XRD and LT-PL.

We see that as for the InAlN layers grown in the previous study, there is a small increase in layer thickness when GaN is grown beforehand, which we attributed to gallium pollution in the chamber. For the composition data shown in Figure 77 (b), firstly, we see a good match between LT-PL In% values with HRXRD simulation data which reinforces these results. Secondly, we see a similar downward trend in composition with a smaller shift compared to the case of InAlN within the measurement uncertainty range.

Thus, both PL and XRD analysis confirm the reduction in indium content for InGaN layers after the growth of 200 nm of GaN before InGaN layers. These changes in thickness and composition are therefore coherent with our previous analysis for InAlN layers.

To explain the difference in thickness, we assume that, as for the case of InAlN depicted in the previous chapter, the TMIn is consumed and converted to TMGa on the showerhead surface due to gallium pollution. This leads to less indium incorporated into the layers, resulting from the reduced partial pressure of TMIn. The additional gallium generated is more readily incorporated into the layers, and so increases the layer thickness relative to layers without gallium pollution.

Having seen similar effects associated with gallium pollution in InGaN as in InAlN when identical growth conditions are used, we decided to check the growth of InGaN material in conditions closer to those used for LED applications. We grew set C of InGaN samples, using multi-quantum well (MQW) growth conditions for the growth of thick InGaN layers, as noted in Table 12. These conditions have a slightly higher temperature (760°C instead of 730°C) and higher pressure than for InAlN (400 mbar instead of 100 mbar). They also have reduced TMGa flow (7.4 µmol/min instead of 21.6 µmol/min) and significantly increased TMIn flow (31.8 µmol/min instead of 9.9 µmol/min).

We started with the growth of the first sample of this set directly on the GaN template after the reactor had been cleaned with chlorine, while for the other four samples, between 25 nm and 200 nm of GaN was regrown on the template before the InGaN layers.

HRXRD ω-2θ scans around the (0002) reflection and RSM (114) scans, were performed on these five samples, as shown in Figure 78, and Figure 79 respectively.

From Figure 78, we can clearly see the InGaN peaks, which are sufficiently shifted from the GaN buffer peaks to be easily separated. We also see clear thickness fringes, thanks to the good surface morphology, which is in agreement with the low roughness of the samples from the AFM scans (Cf. Figure 80).

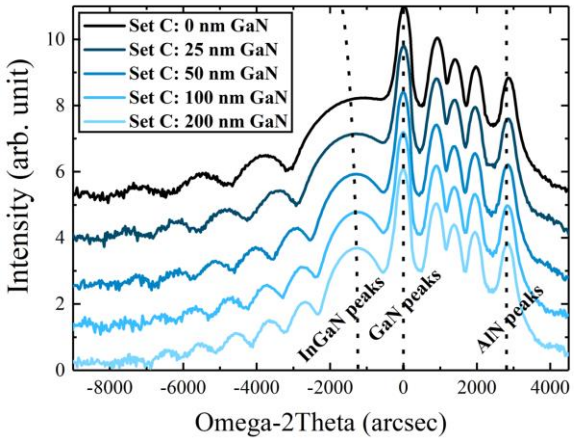

Figure 78: (0002) XRD ω-2θ measurements of set C.

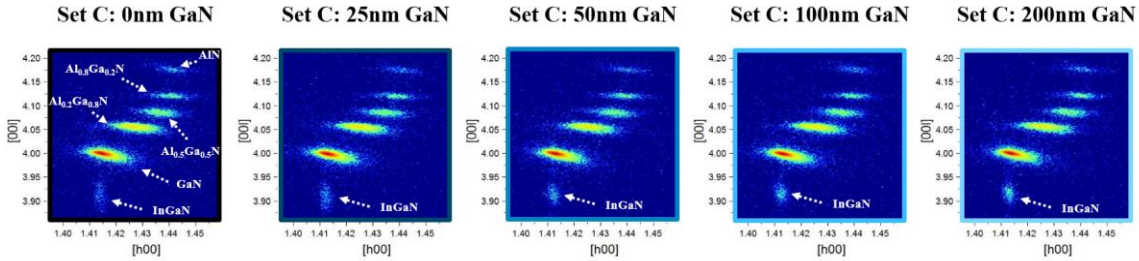

Figure 79: RSM (114) measurements of set C samples.

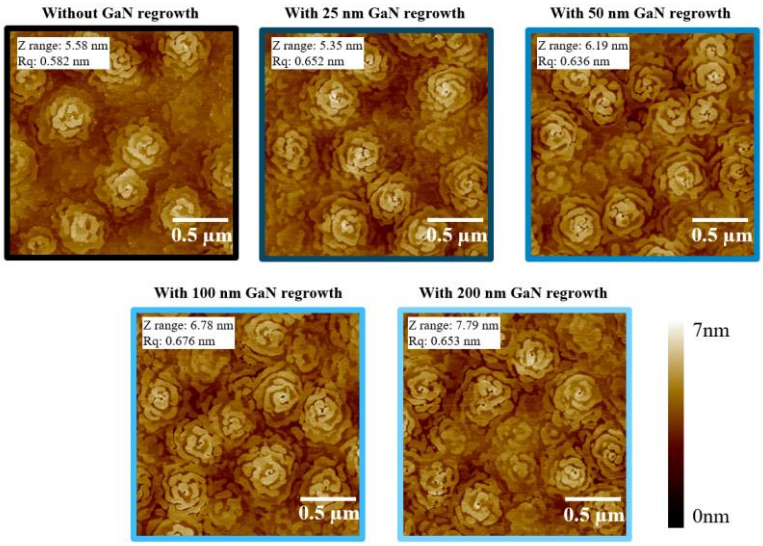

Figure 80: 2µm x 2µm AFM scans of set C.

As before, in addition to the HRXRD and the AFM, we also performed LT-PL measurements for these layers as shown in Figure 81 (a).We calculated InGaN layer thickness and In% from the XRD and PL data and then we plotted them in Figure 81 (b).

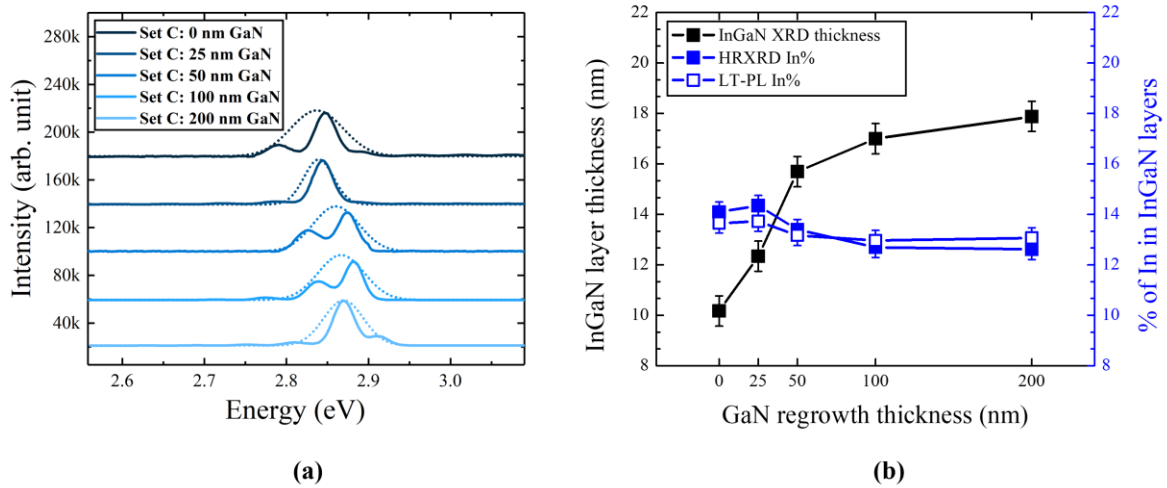

Figure 81: (a) LT-PL spectra: InGaN normalized intensity as function of photon energy at 6K(solid lines) and the fitted data (dash lines). (b) InGaN layer thickness and In% in InGaN layers as deduced from XRD and LT-PL.

Here we see that from a sample with no GaN regrowth to samples with 200 nm GaN regrowth, there is a slight decrease in indium composition from 14% down to 12.5%. The slight difference between the results from HRXRD and LT-PL is linked to the measurement uncertainty range. However, the same trend is seen for both techniques.

By contrast, the thickness shows a significant increase from 10 nm with no GaN regrowth up to 18 nm after 200 nm GaN regrowth. These results show the same trends of reduced indium content and increased thickness as for the previous sets of samples, although with a much more significant effect on the thickness, where we experienced an 80% thickness increase for InGaN growth compared to 10% thickness increase for InAlN growth.

Again, we used the HRXRD data presented in Figure 81 (b) to compare the variation in III-N incorporated masses into our wafers in Figure 82 for InGaN and previously reported InAlN layers for InN and GaN. The AlN binary mass for InAlN is omitted for clarity in this figure.

This time, we see that although the increase of gallium incorporation into InGaN layers with the increased GaN regrowth thickness is in accordance with InAlN growth behavior, the InN mass incorporated shows an opposite trend. For InAlN, the indium incorporation decreased with GaN regrowth thickness, while for these InGaN layers the InN effective incorporation shows an increase with the increase of GaN regrowth thickness.

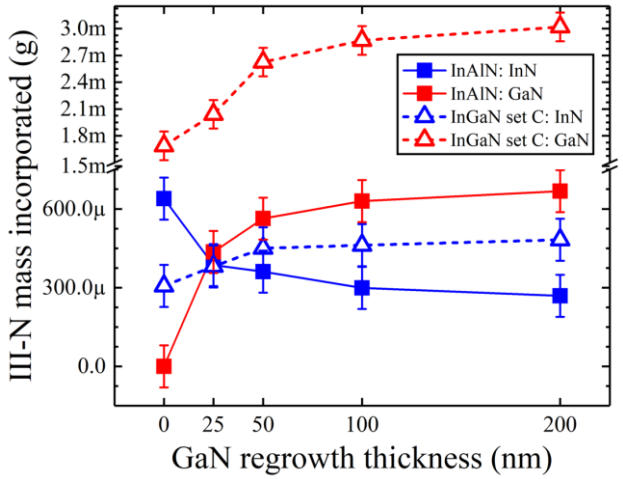

Figure 82: III-N incorporated mass into InAlN and InGaN as a function of GaN regrowth thickness.

We hypothesized that for the samples of set C, the high TMIn flow leads to saturation of In incorporation in InGaN layers. This means that although we predict that the TMIn partial pressure in the chamber is reduced by the gallium pollution (as is the case for InAlN), this barely reduces the indium incorporation into the InGaN. With a higher growth rate caused by the generation of additional gallium, this then leads to an increased InN incorporated mass.

To better understand this indium saturation regime, and the effect of gallium pollution on different layers, we grew set D, where we varied the TMIn flow from 50 sccm to 600 sccm under the same MQW growth conditions as set C for which TMIn flow was 400 sccm. TMIn values in µmol/min are shown for reference in Table 12.

For each TMIn flow used for this set, we grew two samples, one sample with a cleaned reactor and a second sample with 200 nm GaN regrowth. The first type corresponds to a chamber without gallium pollution, while the second type of sample has significant gallium pollution from the chamber.

As before, we performed HRXRD measurements on these samples as shown in Figure 83 (a) and (b) for samples grown in clean and polluted chambers respectively. As for the previous samples, we have clear thickness fringes for all samples facilitating the data extraction, except for samples with low TMIn flows. For these samples we don't see clear thickness fringes and this is likely due to the low contrast between the InGaN layers and the GaN buffers, as the AFM images in Figure 84 show that we have a high quality surface for all the samples.

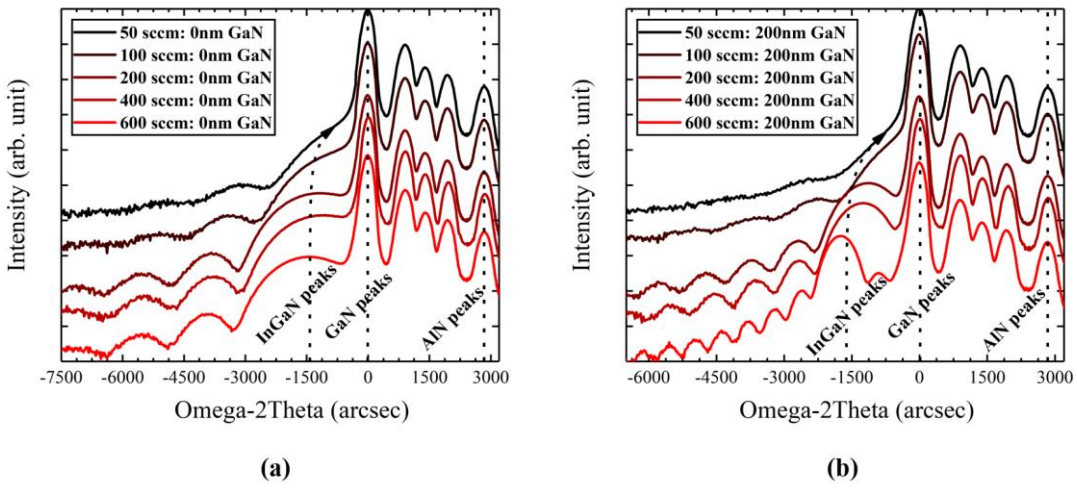

Figure 83: XRD ω-2θ measurements of set D and one sample of set C (TMIn: 400 sccm) of samples grown (a) in cleaned reactor and (b) with 200 nm GaN regrowth.

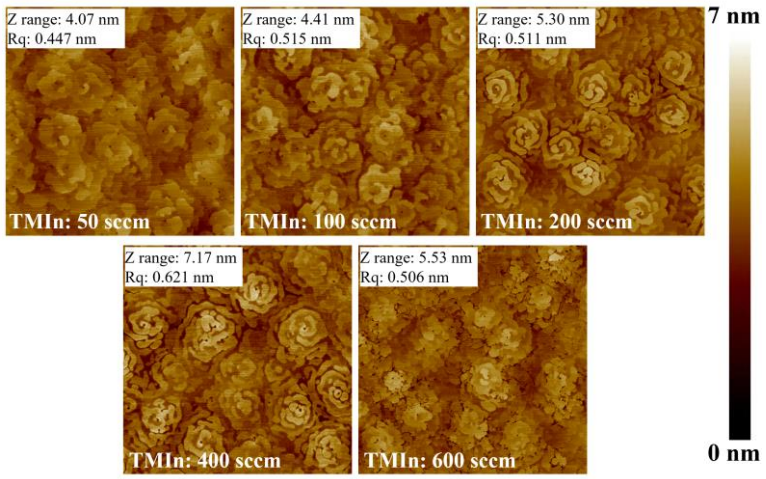

Figure 84: 2µm x 2µm AFM scans of samples grown in cleaned reactor of set D and one sample of set C (TMIn: 400 sccm).

Using HRXRD data, we plotted values for InGaN layers thickness and In% in Figure 85 (a) and (b) respectively.

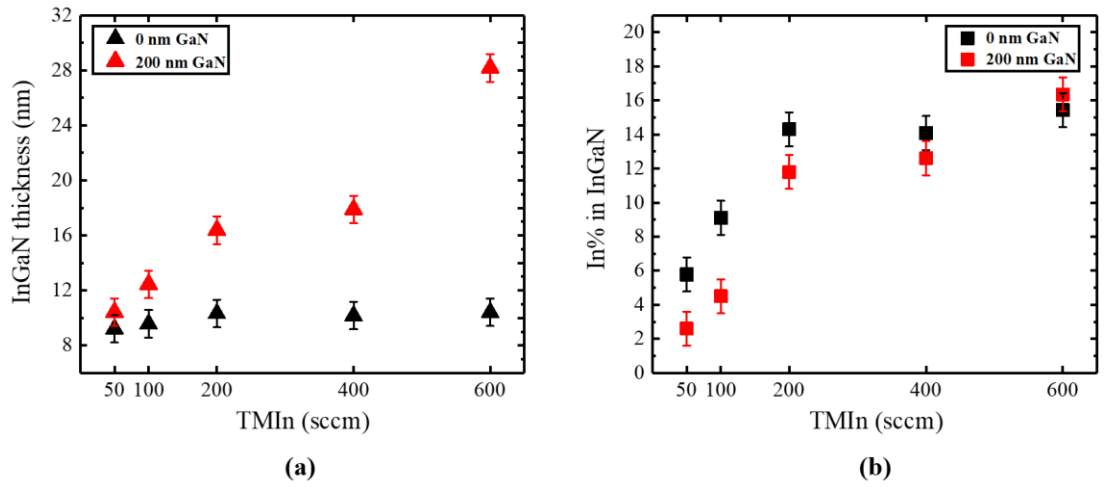

Figure 85: (a) In% in InGaN layers and (b) InGaN layers thickness as a function of TMIn flow.

From these two figures, we notice that with a clean CCS reactor, the InGaN layer thickness is roughly constant over all the TMIn flows used, ranging from 50 sccm up to 600 sccm. For the composition, we see that the indium content in the InGaN layers starts to increase in a linear way for TMIn flows increasing from 50 sccm up to 200 sccm, and then it remains unchanged from 200 to 600 sccm when we can consider that we are in an indium saturation regime. The slight reduction in thickness below 200 sccm TMIn flow reflect the reduction in indium content, with around 10 nm thickness for InGaN layers with 14% In, and 9 nm for 6% In, implying that the change in thickness is entirely linked to the quantity of indium incorporated into the layers.

By contrast, when 200 nm of GaN is regrown on the template before the InGaN layers, i.e. when the growth chamber is polluted with gallium, a very different behavior is observed. In particular, we see a significant increase of the final InGaN layer thickness with increased TMIn flow. This is consistent with the linear relationship between gallium pollution and TMIn flow that we have seen in InAlN in previous work [150], and corresponds to our hypothesis of a parasitic reaction between the TMIn and the metallic gallium on the shield. Any additional TMIn corresponds to the release of more gallium from the shield, thus increasing the final thickness of the layer.

However, concerning the In% in the final InGaN layers, we see the same tendency seen when working in a clean chamber, meaning a linear increase of In% followed by a saturation when increased TMIn flows are used. Nevertheless, the In% values here are lower when compared to the values seen when growing in a clean chamber except for the highest growth rate. This effect is particularly clear in the low indium regime below a TMIn flow of 200 sccm. This lower indium content is explained by the loss of the TMIn precursor during to the conversion of TMIn into TMGa during the parasitic reaction. However for the sample grown under very high TMIn flow of 600 sccm, we see a slight increase in In%, and this is likely due to the very high growth rate that we had for this layer due to the high gallium pollution.

When comparing these two growth regimes (with and without gallium pollution) there is a clear interest of working in conditions without gallium pollution. The growth is more easily interpreted, and easier to predict, as the requested TMIn and TMGa flows control the thickness directly. We see that the indium incorporation increases with TMIn flow until we reach the saturation regime around 200 sccm when using our growth parameters of chamber pressure, temperature, and TMGa flow. Above this value, neither the thickness nor the composition changes. However, with gallium pollution, the InGaN layer thickness is strongly affected by the TMIn flow and the composition is then indirectly affected by the growth rate.

IV.4 Conclusion

We have shown in this chapter that there is a strong effect of the gallium pollution on the growth of InGaN layers. The effect is more pronounced both for increased GaN regrowth thicknesses and for higher TMIn flows. Although the results are less clear-cut than for InAlN layers, they consolidate the hypothesis of the conversion of TMIn to TMGa by reacting with gallium on the showerhead shield, and increase the understanding behind the complicated behavior of InGaN growth.

We have found in particular that when working under typical MQW growth conditions in CCS reactors, i.e. when using high TMIn flows, gallium pollution has very strong effects on the final thickness of InGaN layers. Performing the same growth in a clean chamber show

more easily interpretable results, and more predictable growth behavior, with no change in thickness or composition of InGaN in a saturation regime.

We therefore suggest that due to the high degree of complexity in InGaN MOVPE growth, it is important to take into consideration the effect of gallium pollution when growing such layers in any growth conditions. In addition, it is indeed preferable to work in conditions without gallium pollution to better control the thickness and alloy composition of InGaN structures, a prerequisite for the reproducibility of InGaN based light emitting devices.

As discussed above, limiting gallium pollution can be achieved through growth interruption followed by chlorine cleaning, and we could also try to optimize the properties of these layers using a 5 nm H_2 etch as described in the previous chapter.

As we have clearly shown the appearance of a saturation regime versus TMIn flow, growth in a clean chamber should permit a reduction in TMIn usage without unwanted side-effects on the well thickness. This can thus reduce consumption of TMIn during the MOVPE growth of InGaN in CCS reactors.

Chapter V: Overcoming Ga contamination in Close Coupled Showerhead reactors

V.1 Introduction

As we have seen from chapters III and IV, the gallium pollution in Close Coupled Showerhead reactors has an important effect on the growth process stability of InAlN and InGaN ternary alloys This pollution results in an increase of the alloy layer thickness together with a loss of control of their composition, due to the parasitic chemical reactions between the TMIn sent to the growth chamber and the metallic Ga on the shield. The solution in chapter 3 involved removing the wafer and performing a clean in the chamber before growing the active structure. However, a preferred solution would be to perform all the growth in one run. Therefore, in the current chapter, we focus on understanding the origin of the metallic gallium on the shield in order to avoid it later on during the growth of ternary alloys.

As illustrated in Figure 86, during GaN buffer growth, the two hypotheses that we suggest for the origin of the metallic gallium pollution on the shield are: 1) gallium coming directly from the TMGa that is sent to the growth chamber, or 2) gallium coming from the condensation on the shield after being desorbed from the GaN surface.

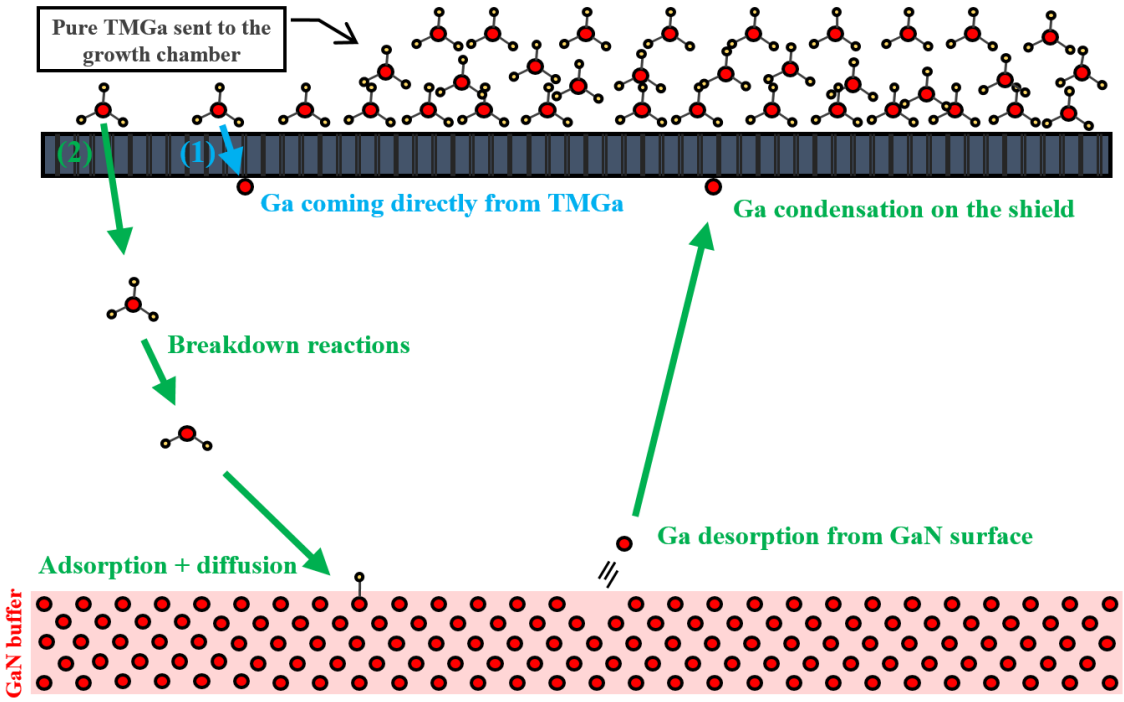

Figure 86: The potential origins of Ga pollution on the shield.

The first case, where Ga could be coming directly from the TMGa, is considered less likely to happen, as the shield has a low temperature compared to typical temperatures required for decomposition of TMGa, of around 400°C under H_2 ambient as shown in Figure 87. The desorption case is thus considered more likely to happen. In particular it is known that at typical GaN growth temperatures, there is an equilibrium between growth and desorption or etching [173]. In addition, in chapter 3 we found after desorbing 40 nm of GaN we subsequently found gallium pollution in InAlN layers. Therefore, in this chapter, we have performed many experiments in this context where we have focused on testing different strategies to avoid the desorption of Ga from the GaN surface to the shield. This should enable us to grow GaN ternary alloys in a more controllable, stable and understandable way.

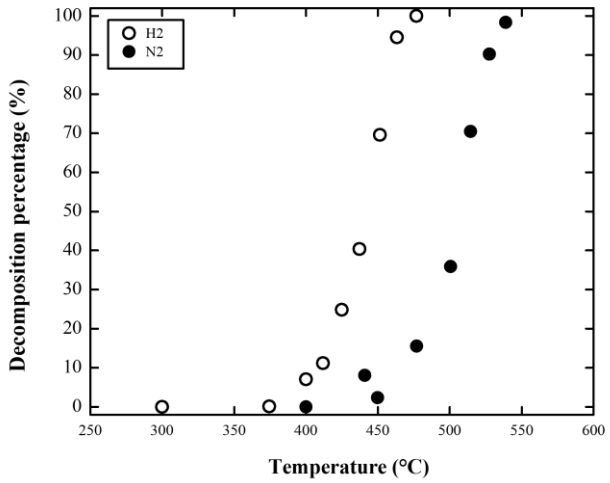

Figure 87: Percentage pyrolysis versus temperature for TMGa in ambients of H_2 and N_2. [120]

V.2 Tests to avoid Ga pollution

V.2.1 AlGaN buffers regrowth

In the third chapter of the manuscript, we performed GaN regrowth from 0 to 200 nm on the 2 µm GaN buffers just after performing a growth interruption and a chlorine cleaning. GaN regrowth was followed by the growth of the active HEMT layers (AlN spacer + InAlN barrier).

In this chapter, and as illustrated in Figure 88, we have performed the same experiment as before but this time with AlGaN regrowth instead of GaN, as it has been shown that AlGaN desorption rates are much lower than those for GaN [174]. Introducing an Al component into these regrown layers should help us understand more about the Ga desorption.

25 nm thick AlGaN layers were grown with Al% ranging from 25% down to 5% under a growth temperature of 1040 °C and a growth pressure of 100 mbar.

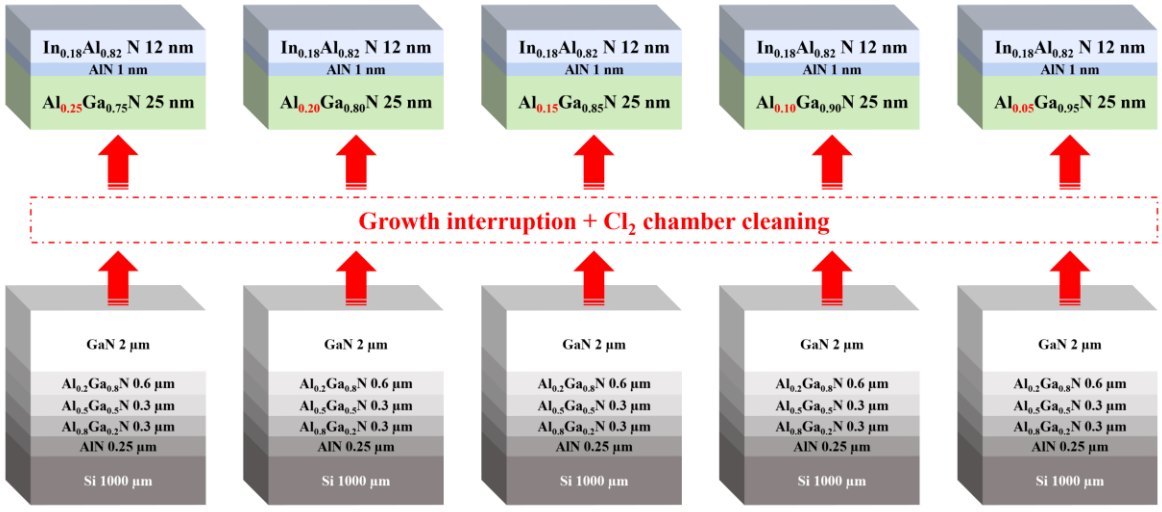

Figure 88: Schematic of growth structures of InAlN barriers on the top of AlGaN buffers with different Al%.

First, we examined the surface morphologies of these layers and we compared it to the surface morphology of the sample which had 25 nm GaN regrowth as pictured in Figure 89.

We see that growing InAlN barriers with In% of around 18% on top of AlGaN layers with high Al% of around 25%, results in a very rough surface morphology. This is due to

the high lattice mismatch between the barrier and the buffer below, and the effect of cooling down the AlGaN to InAlN conditions under an H_2/NH_3 atmosphere, which has been shown to lead to cracks [175] [176] [177]. However, when decreasing the Al% in AlGaN buffer into low values, we see a smoother barrier surface. The best morphology is seen for the sample which had pure GaN regrowth, thanks to the nearly lattice matched InAlN on GaN.

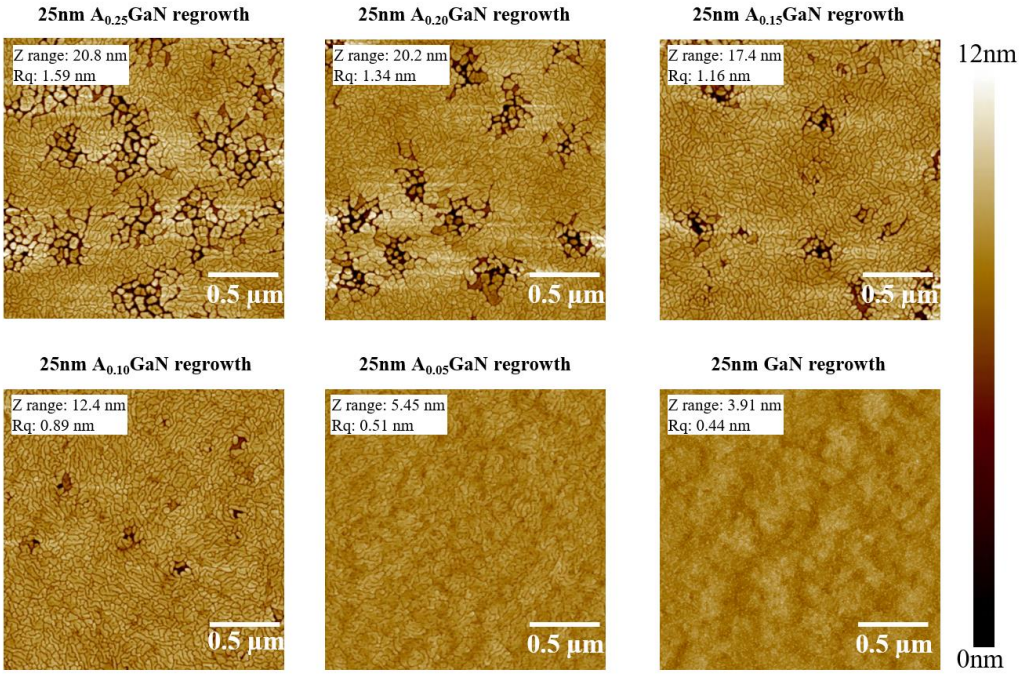

Figure 89: 2µm x 2µm AFM scans of InAlN barriers grown on the top of AlGaN and GaN buffers.

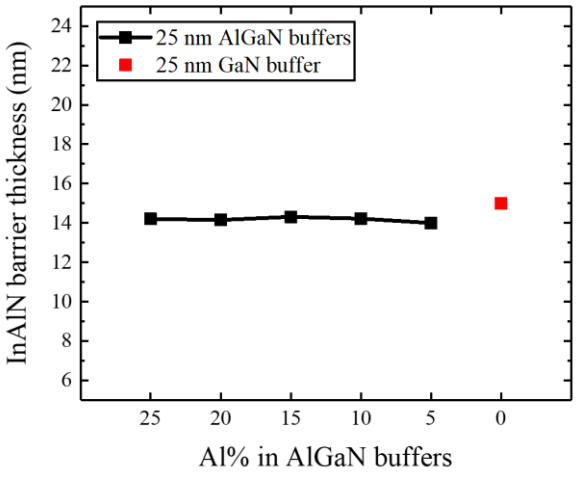

Figure 90: XRR measurements of the InAlN barriers for AlGaN and GaN buffers.

XRR measurements were also performed on the set of 5 samples, as shown in Figure 90. We see that InAlN barrier layers thickness were found to be constant across all AlGaN regrowth samples with a value of around 14 nm.

However, when performing a regrowth of 25 nm of GaN we see a small increase in InAlN barrier thickness, which we associated in chapter 3 to the nonintentional incorporation of Ga.

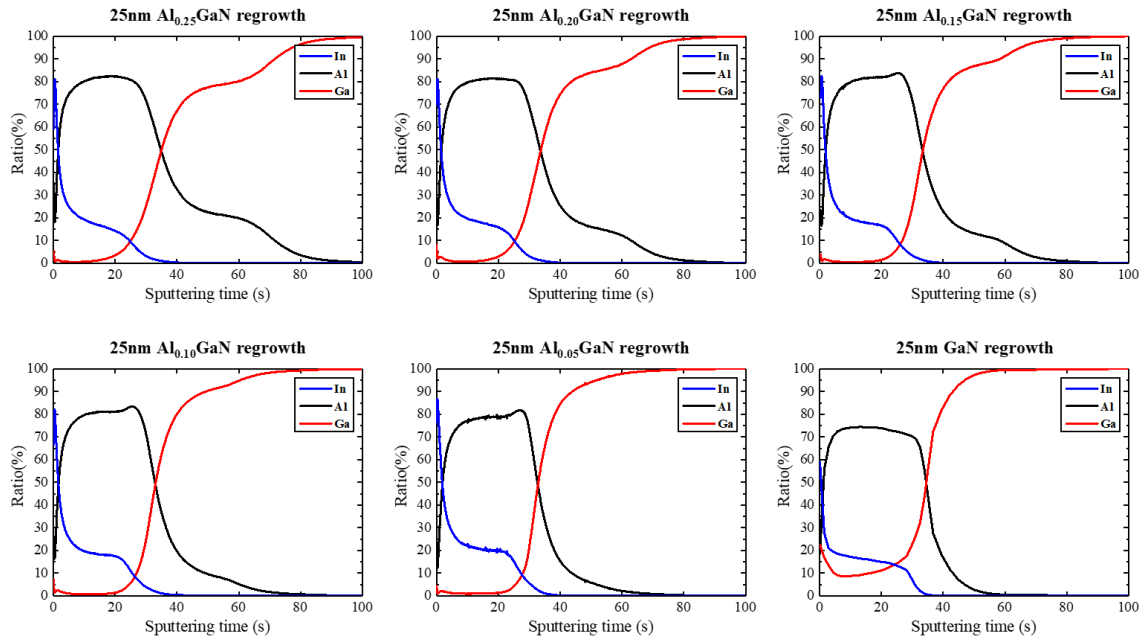

Figure 91: PP-TOFMS measurements for samples grown with 25 nm of AlGaN with different Al% and GaN.

Next, with the PP-TOFMS technique, we measured the elemental composition of these barriers, as shown in Figure 91. We see that InAlN barriers grown on AlGaN buffers have no gallium incorporated. On the other hand, the 25 nm GaN regrowth sample shown in this figure shows that even for small GaN regrowth thickness of 25 nm we have an incorporation of up to 10% of gallium into InAlN barriers.

The XRR and the PP-TOFMS results suggest that introducing Al atoms even with small amounts into GaN regrowth prevents Ga desorption from the grown layers, resulting in significantly reduced gallium pollution and the growth of pure InAlN barriers.

However, we examined the electrical performance of these samples with 4PP technique, and as illustrated in Figure 92, we see poor electrical performance for all samples

grown on AlGaN buffers compared to the sample grown on GaN buffer. This electrical performance improves as we decrease the Al% in AlGaN buffers, going towards pure GaN buffers.

This behavior is expected due to the presence of the aluminum atoms in the 2DEG channel. These atoms cause alloy scattering in the GaN 2DEG channel, and are thus expected to decrease the 2DEG mobility. In addition, increasing aluminum content in the AlGaN layer will reduce the polarization difference between the InAlN and the AlGaN (Cf. figure 6 Chapter 1) which will reduce the N_s. Both of these lead to poor Rsheet results. It was not however possible to perform Hall Effect measurements to confirm this hypothesis.

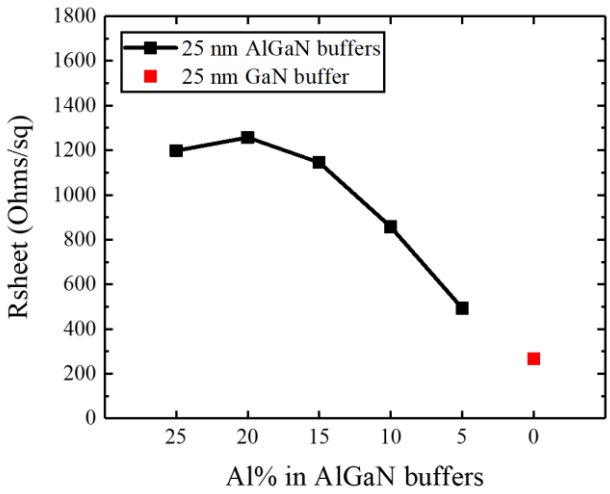

Figure 92: Sheet resistance for samples grown with 25 nm of AlGaN with different Al% and GaN buffers.

As a conclusion for this section, we see that growing AlGaN alloys instead of GaN alloys helps in preventing the Ga contamination of InAlN barriers grown afterwards. However, using AlGaN alloys as channels for HEMT was not a good idea as this leads to a drop in the electrical performance seen in Figure 92.

V.2.2 Nitridation of the shield

An alternative approach was to maintain the growth of GaN channels instead of AlGaN channels but this time remedying the problem of the metallic gallium on the shield by performing a nitridation step with ammonia post GaN growth and before InAlN growth.

During the nitridation step we basically aim to transform the metallic Ga on the shield into GaN molecules. GaN is considered as a more stable compound compared to the metallic Ga and it does not undergo any chemical reaction with the TMIn sent to the growth chamber. Therefore, this was hoped would avoid the loss of indium and the nonintentional incorporation of gallium during the growth of InAlN layers.

During the nitridation step, which lasts 600 seconds, we anneal the growth chamber in conjunction with the shield, post GaN growth in a nitrogen environment. The anneal temperatures and pressures are detailed in Table 13. The intention of this experiment was to increase the temperature of the shield towards 400°C, as GaN can be grown at this temperature, and so we can assume that cracked ammonia will be able to react with gallium [178]. Thus, we should be able to remove the metallic gallium causing the parasitic chemical reaction with TMIn.

	Sample-Shield gap (mm)	**Sample T during nitridation (°C)**	**Shield T during nitridation (°C)**	**Growth chamber pressure (mbar)**
Sample (a)	11 (standard)	1020	**290**	400
Sample (b)	7	560	**375**	400
Sample (c)	7	775	**560**	400

Table 13: Nitridation step anneal conditions.

As pictured in Figure 93 and Figure 94, three samples were grown for this experiment, sample (a), (b) and (c). We changed the gap between the shield and the wafer for samples (b) and (c) in addition to changes in sample annealing temperature. This was done in order to change the shield temperature during the nitridation step and see how this process is affected by the change in shield temperature.

For sample (a), the sample-shield distance during the nitridation step was kept the same as we used during the growth of GaN, which is 11 mm. This distance is the standard distance between the sample and the shield that we actually use for any growth. During the nitridation process the shield temperature was 290 ° C.

For sample (b), we reduced the sample-shield gap during the nitridation step down to 7 mm, in order to increase the shield T while decreasing the sample anneal T as shown in Table 13. In this case, the shield nitridation T was 375 °C.

For the last sample, sample (c), we used the same procedure as for sample (b), but this time with a higher sample anneal T of 775 °C during the nitridation step. In this case, the shield nitridation T was increased further up to 560 °C.

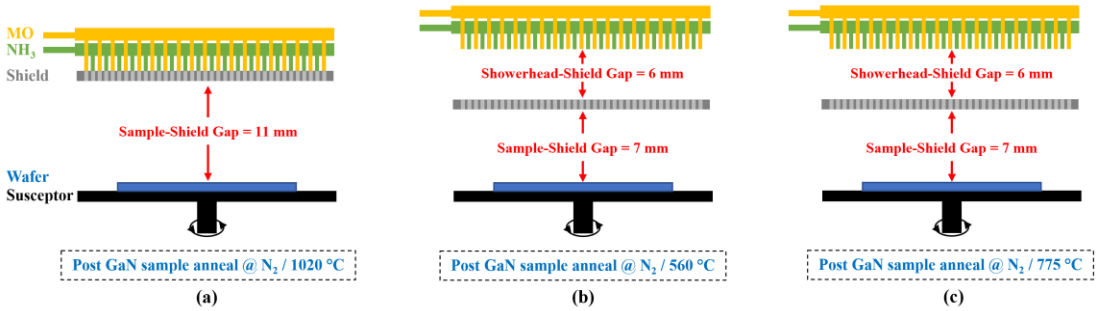

Figure 93: Diagram showing growth chamber during the nitridation step for sample (a), (b) and (c).

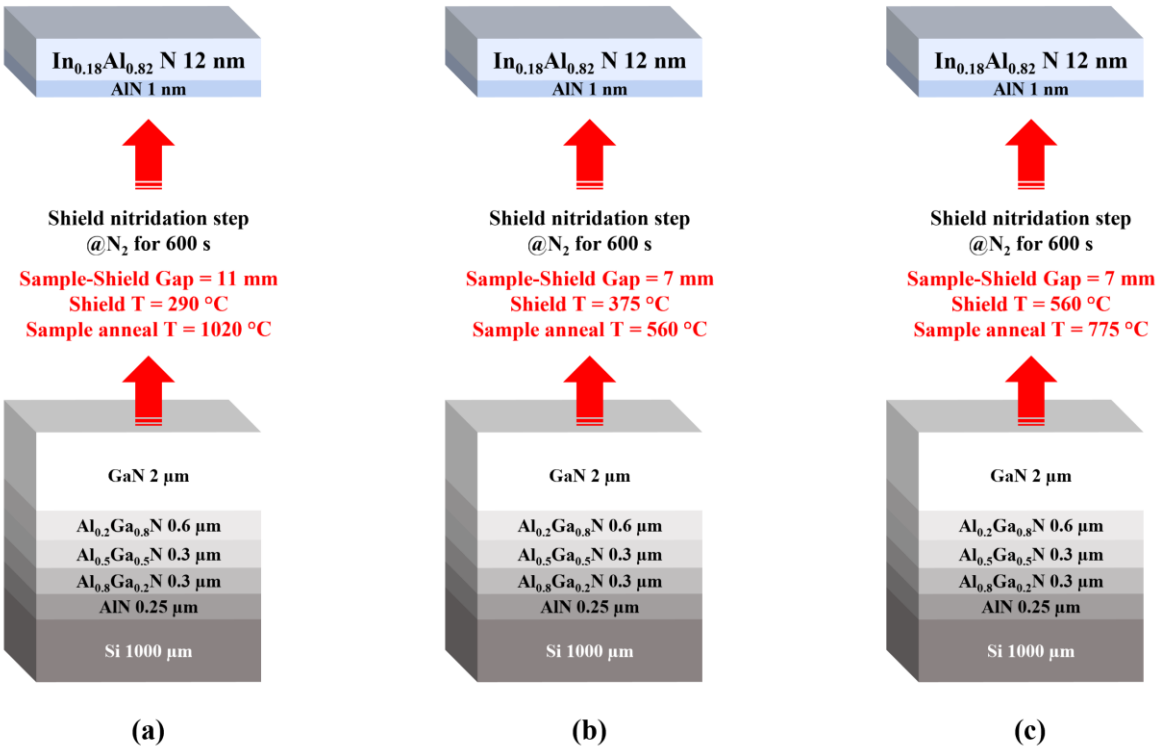

Figure 94: Schematic of growth structures during nitridation experiment for sample (a), (b) and (c).

InAlN barriers thickness were measured using XRR technique as pictured in Figure 95 where we see a drop in barriers thickness.

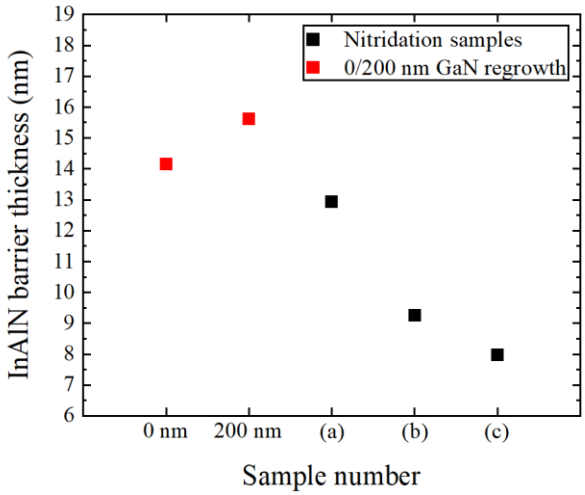

Figure 95: XRR measurements for the 200 nm GaN regrowth sample and the nitridation samples.

We further checked the surface morphology of the three samples and their InAlN barriers composition with AFM and PP-TOFMS respectively, as shown in Figure 96. We compared these results to the sample which had 200 nm GaN regrowth from chapter 3, as for more than 100 nm of GaN regrowth, the In to Ga conversion rate saturates [171].

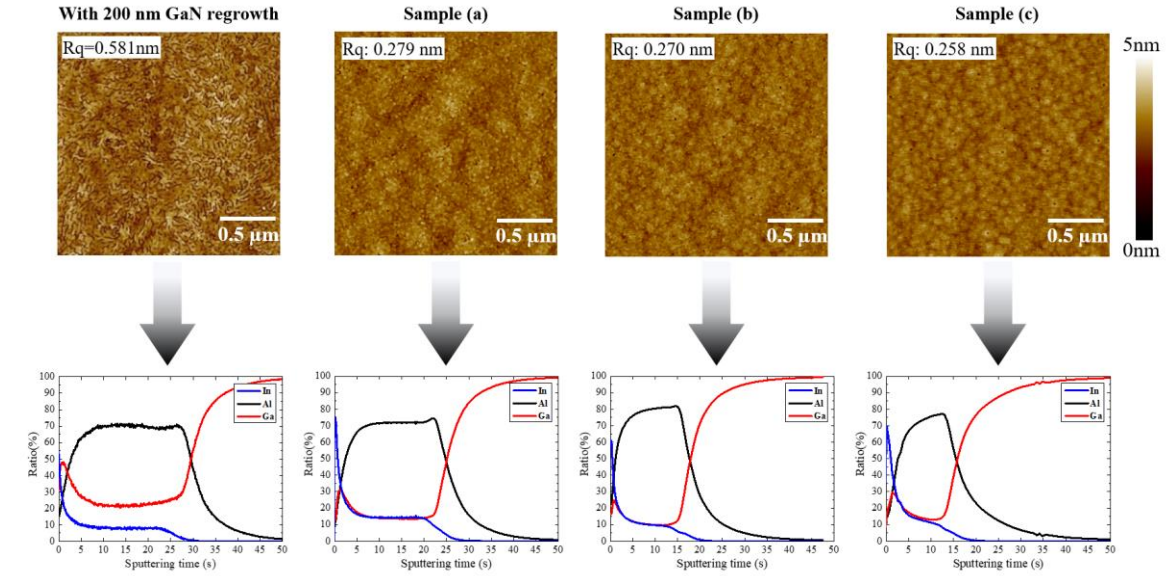

Figure 96: 2µm x 2µm AFM scans with PP-TOFMS measurements of the nitridation samples (a), (b), and (c) and the 200 nm GaN regrowth sample.

The three samples (a), (b), and (c) have a quite similar smooth surface morphology with RMS less than 0.3 nm. Their morphology is improved compared to the sample which had 200 nm GaN regrowth where we see cracks and a doubled RMS. This difference is explained by the different composition found in the layers.

For the composition by PPTOF-MS, we notice that for the first sample, sample (a), in comparison with the 200 nm GaN regrowth sample, we have a lower nonintentional incorporation of Ga and a higher incorporation of In into the barrier. For samples (b) and (c) we see a similar behavior with that of sample (a).

Next, we have performed 4PP measurements on these samples to check their electrical performance, as shown in Figure 97. From this figure, we see that we managed to get with sample (a) an Rsheet value of 163 Ohm/sq equivalent to the state of the art value of 167 Ohm/sq [62].

In sample (a) we have a reduction of Ga pollution and therefore a slight reduction of thickness. We also find an excellent electrical performance which can be explained by firstly the good In/(In+Al) ratio in the barrier layer which is about 15/(15+70) = 17.6 %. This value shows that the barrier is nearly lattice matched to GaN buffer. This explains the smooth surface morphology of sample (a) where we see no cracks.

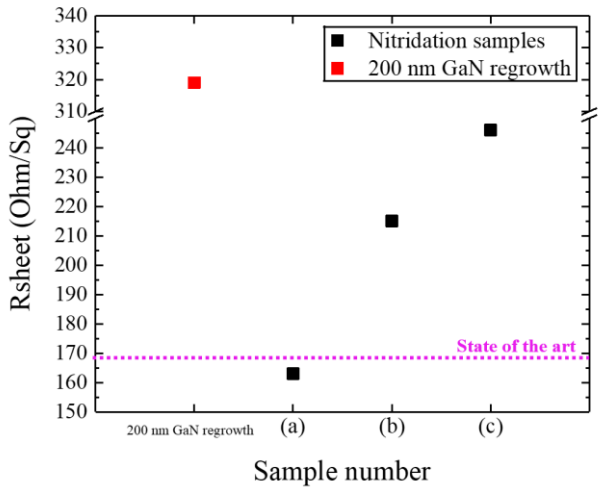

Figure 97: Rsheet measurements of the nitridation samples (a), (b), and (c) and the 200 nm GaN regrowth sample compared to the state of the art Rsheet value of InAlN on GaN on Si HEMTs [62].

For samples (b) and (c) we have reduced thickness and increased Rsheet even though the composition is the same as for sample (a). It may be that heating the shield at 7 mm from the wafer may result in desorbing some impurities from the shield which are integrated into the layers, slowing the growth and increasing the Rsheet.

From the whole work above, we suggest that the nitridation step has failed in transforming the metallic Ga pollution on the shield into GaN, as we have seen Ga incorporated into the InAlN barriers. However, the loss in In was lower with this step, which led us to grow nearly lattice matched InAlN barriers on GaN buffers, resulting in an Rsheet of 163 Ohm/sq equivalent to state of the art.

V.2.3 16.5 mm Sample-Shield growth gap

It is clear that the nitridation experiment did not help completely in overcoming the effect of Ga pollution on the growth of InAlN. Therefore, we suggested another test that would potentially help in avoiding the Ga pollution effect, where this time we increased the distance between the sample and the shield during GaN regrowth, e.g. during the desorption of Ga from the surface.

This increase of sample-shield distance from 11 mm to 16.5 mm should decrease the amount of Ga condensed on the shield.

In this context, we wanted to regrow 100 nm of GaN with the 16.5 mm sample-shield distance and compare it to the equivalent sample grown in chapter 3 with 11 mm sample-shield distance. But because of the hardware modification mentioned above, which resulted in a change of the boundary layer δ_0 thickness as seen in chapter 2, the GaN growth rate was affected, with the consequence that only 70 nm of GaN were grown, as shown in Figure 98.

The growth conditions of this sample are similar to that we used in chapter 3. The only difference is the increased sample shield gap of 16.5 mm during GaN regrowth.

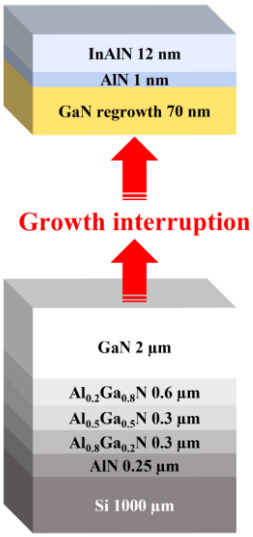

Figure 98: Schematic growth structure of the sample with 16,5 nm sample-shield gap.

Firstly, we measured the InAlN barrier thickness of this sample and compared it to the 50 nm GaN regrowth sample of chapter 3. XRR measurements of both samples are illustrated in Figure 99.

We see a drop in barrier thickness for the sample which had a 70 nm GaN regrowth under a 16.5 mm sample-shield gap compared to the 50 nm GaN regrowth under a 11 mm sample-shield gap. This suggests that gallium pollution is affected by the distance between the sample and the shield during GaN growth.

In order to make things clearer we also performed AFM and PP-TOFMS measurements on this sample, and again we compared it to the 50 nm GaN regrowth sample. AFM and PP-TOFMS measurements are shown in Figure 100.

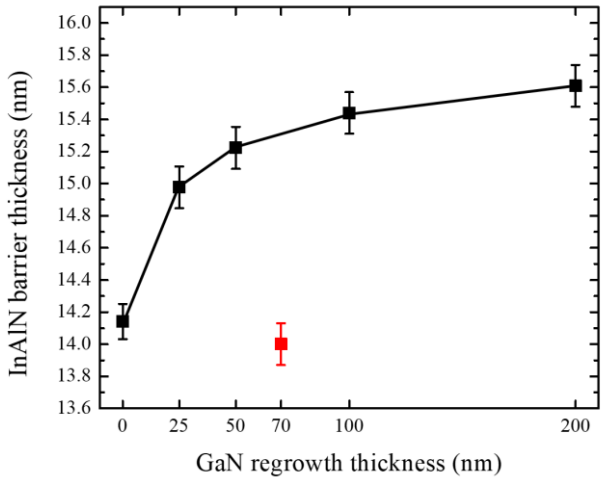

Figure 99: XRR measurements for the set of GaN regrowth samples of chapter 3 in black, including the 50 nm GaN regrowth sample (11 mm sample-shield gap) and the 70 nm GaN regrowth sample in red (16.5 mm sample-shield gap).

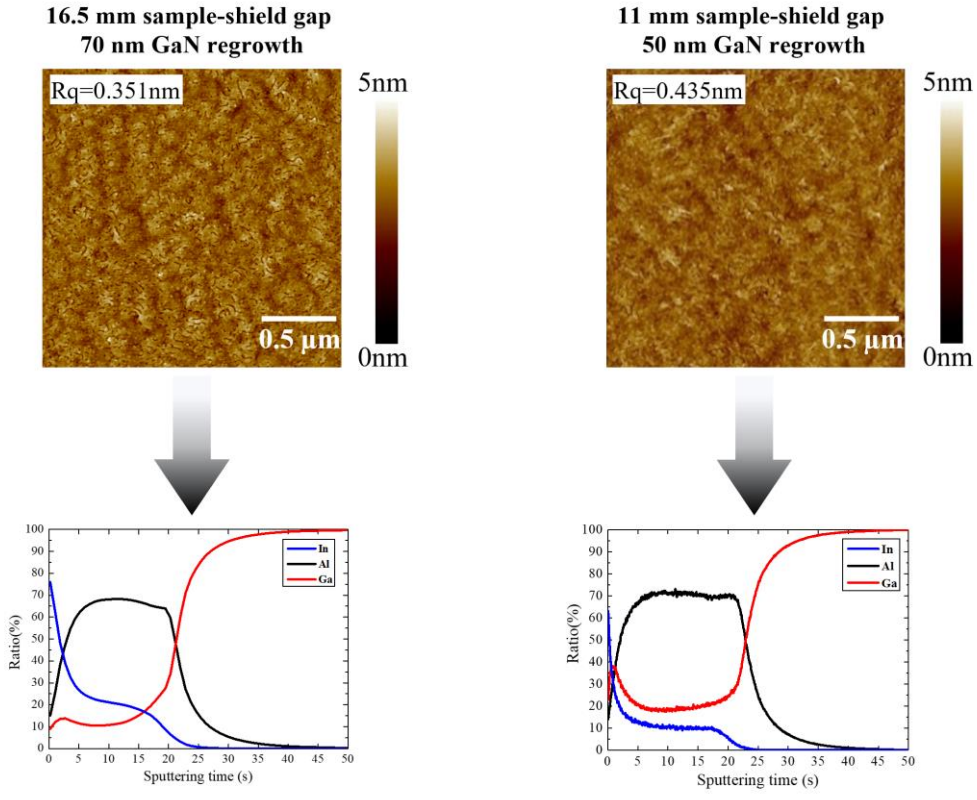

Figure 100: 2µm x 2µm AFM scans with PP-TOFMS measurements of the 70 nm GaN regrowth sample (16.5 mm sample-shield gap) and the 50 nm GaN regrowth sample of chapter 3 (11 mm sample-shield gap)

From the AFM images we see similar morphologies for both samples. From the PP-TOFMS measurements, we see a lower nonintentional incorporation of gallium of 10% for the 70 nm GaN regrowth sample compared to the 19% seen for the sample which had 50 GaN regrowth (Cf. Figure 101 for comparison with the whole set grown in chapter 3). We also see more indium incorporated with this drop of gallium incorporation, as seen for other experiments.

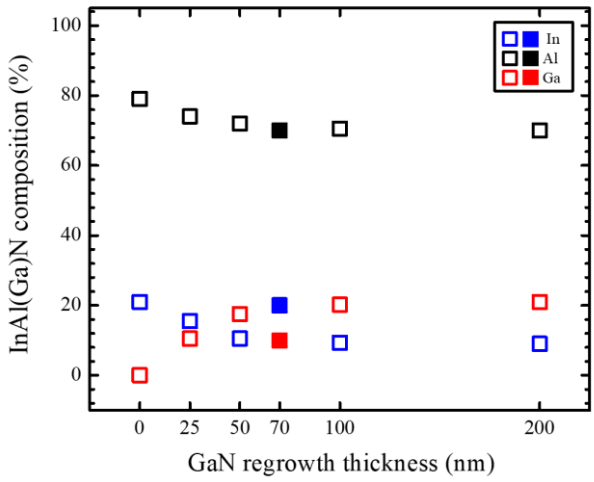

Figure 101: PP-TOFMS measurements of the set of GaN regrowth samples of chapter 3 open squares, including the 50 nm GaN regrowth sample (11 mm sample-shield gap) and the 70 nm GaN regrowth sample full squares (16.5 mm sample-shield gap).

We further checked the electrical performance of this sample with 4PP technique. As pictured from Figure 102 we find a very good 2DEG channel resistance of 205 Ohm/sq. However, this value is not as good as what we have previously seen with the nitridation sample in Figure 97. This is likely due to the higher In/(In+Al) ratio of 21/(21+68) = 23.6%. This ratio resulted in a slightly compressively strained barrier, and so an overall lower total polarization.

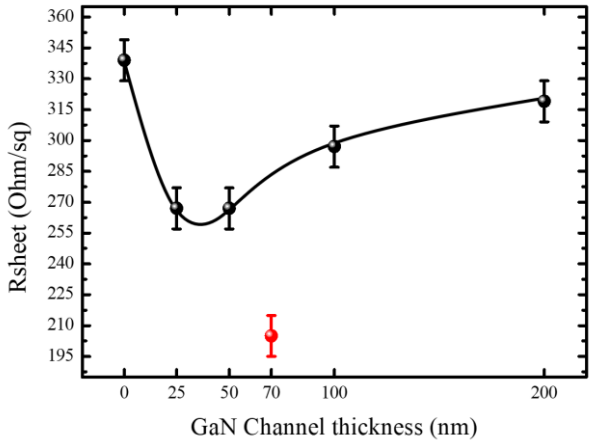

Figure 102: Rsheet measurements of the set of GaN regrowth samples of chapter 3 in black, including the 50 nm GaN regrowth sample (11 mm sample-shield gap) and the 70 nm GaN regrowth sample in red (16.5 mm sample-shield gap).

These results suggest that the increase of sample to shield distance during GaN growth has reduced the quantity of gallium deposited on the shield and so reduce the gallium pollution during the growth of InAlN, where we see more indium incorporated and less nonintentional incorporation of gallium. However, once again, this was not sufficient to completely remove the pollution.

V.2.4 Low temperature 200 nm GaN regrowth under H_2

Next, in order to understand more the link between the Ga desorption rate from GaN buffers and the growth temperature of the layer, we decided to grow GaN layer at lower temperatures. We went from the standard temperature used for the 200 nm GaN regrowth of 1040 °C in chapter 3 down to 960 °C and 880 °C, as pictured in Figure 103.

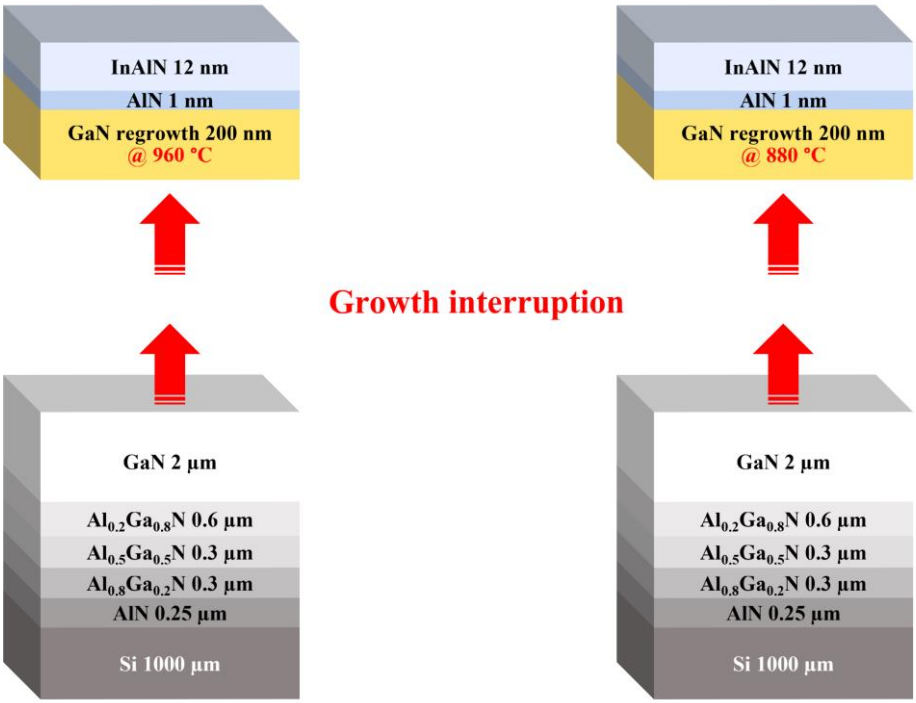

Figure 103: Schematic growth structures of the 960 °C and the 880 °C GaN regrowth samples.

InAlN barriers thickness of these samples were measured using XRR, as pictured in Figure 104, and AFM and PP-TOFMS measurements as pictured in Figure 105.

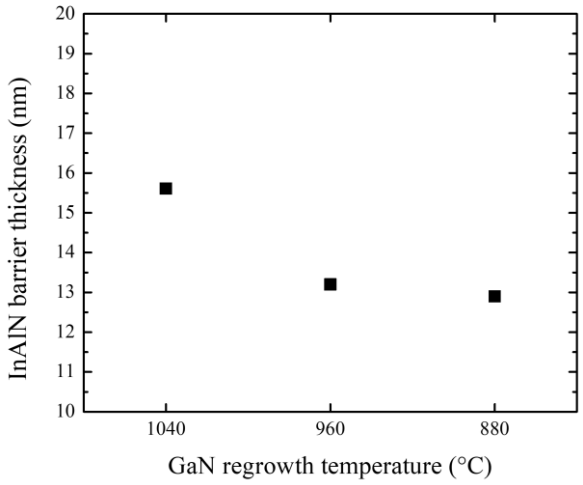

Figure 104: XRR measurements for the 1040 °C, 960 °C and 880 °C GaN regrowth samples.

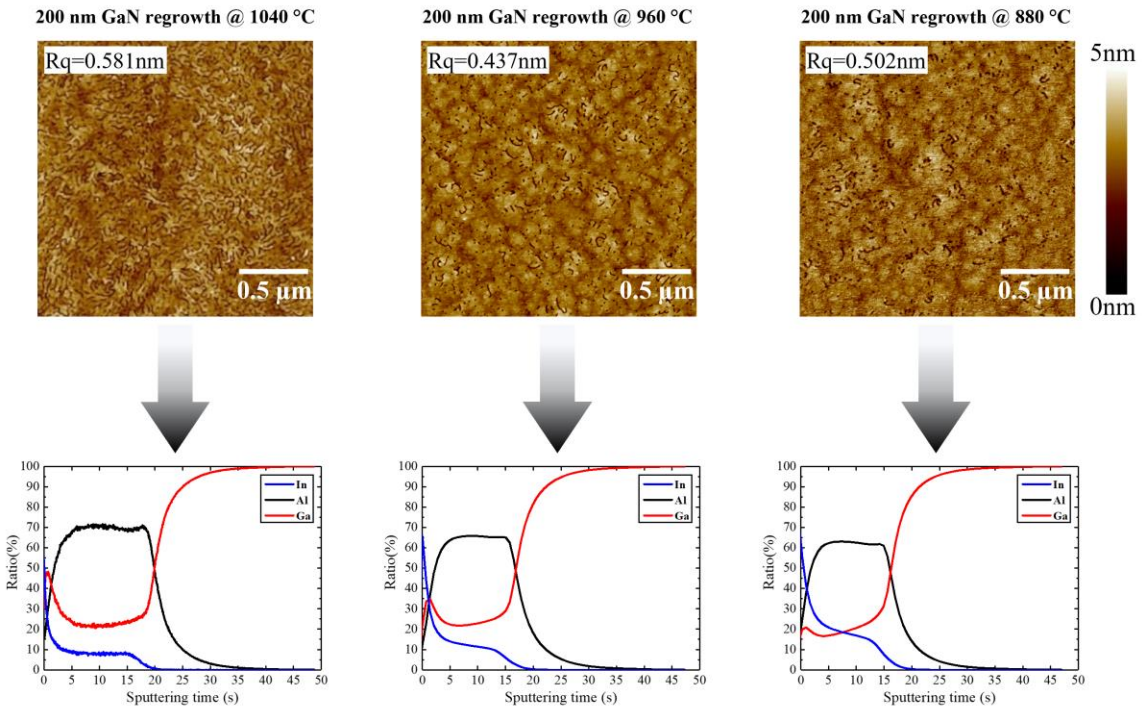

Figure 105: 2µm x 2µm AFM scans with PP-TOFMS measurements of the 1040 °C, 960 °C and 880 °C GaN regrowth samples.

From the XRR, we see a drop of around 2.5 nm in InAlN barriers thickness (i.e. about 17%) for both samples compared to the sample where we used the standard GaN growth temperature of 1040 °C. This would tend to imply less gallium pollution. From the AFM images, we see a similar morphology for all samples with a roughness varying from 0.4 nm to 0.6 nm. From the barrier composition, we see an increase of indium composition and a decrease of gallium when we decrease the GaN regrowth temperature. These results suggest that the gallium desorption has been reduced as expected by the reduction in GaN regrowth temperature, but this is still not sufficient to avoid the nonintentional incorporation of gallium into InAlN barriers.

We performed Rsheet measurements on these samples, as shown in Figure 106 (a). We see an improvement for the sample which had a GaN regrowth temperature of 960°C compared to the sample which had a GaN regrowth temperature of 1040°C. This is due to the improved In/(In+Al) ratio and the improved overall barrier polarization as we can see from Figure 106 (b). For the last sample we see a drop in the electrical performance despite the increased polarization, when we have regrown the GaN at a temperature of 880°C. This

is likely due to the increase of carbon concentration in the GaN channel at such a low growth temperature.

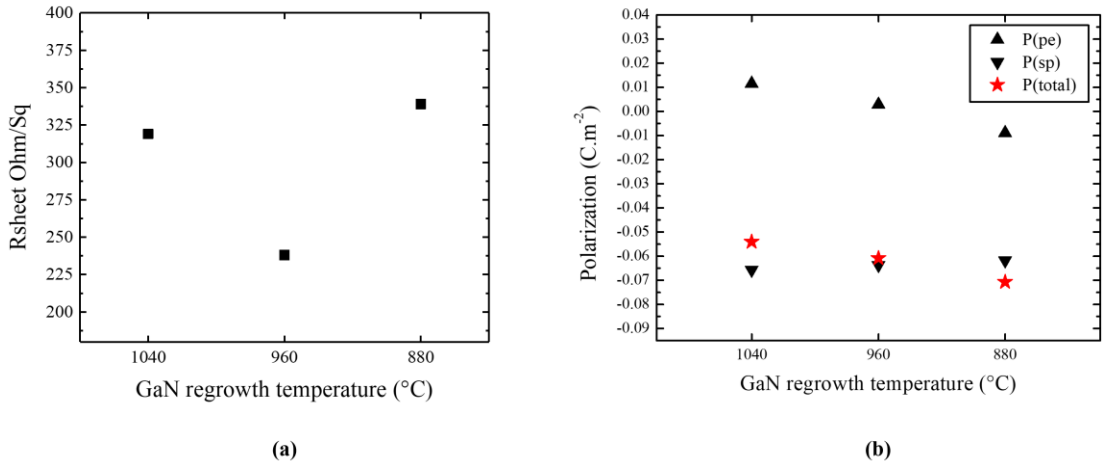

Figure 106: (a) Rsheet measurements and (b) calculated barriers polarizations of the 1040 °C, 960 °C and 880 °C GaN regrowth samples.

V.2.5 Increasing shield temperature during GaN regrowth

As a conclusion for all the experimental work presented above, one must say that overcoming the gallium pollution in CCS reactors was not an easy task to achieve by changing the growth parameters of the GaN regrowth.

The previous experiments focused on reducing the gallium desorption from the layers to the shield, but the alternative method of shifting the equilibrium was to increase the temperature of the shield. This would lead to less deposition of gallium on the shield for the same growth conditions.

Two different approaches were employed for the increase of shield temperature during GaN growth. The first approach was to alter the reactor hardware, and create a gap between the shield and the showerhead during GaN growth. As the showerhead is water cooled, and the wafer is heated to around 1040°C during GaN growth, a small gap should make a big difference. We therefore used a nominal shield showerhead spacing of 0.5 mm (versus a shield to wafer distance of 11 mm), as shown in Figure 107, configuration (A). This configuration was not always stable (and difficult to measure), and therefore there is some variability of this value during the experiments, leading to variability of shield temperature.

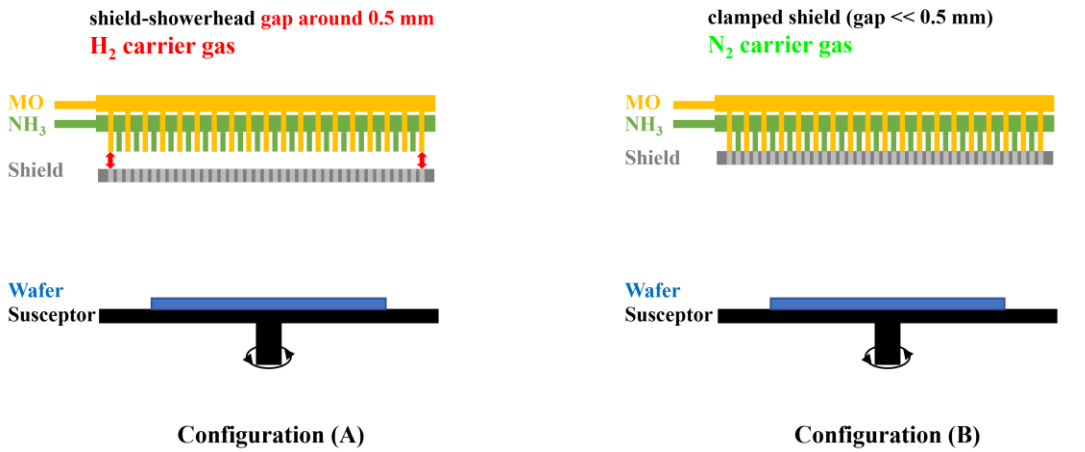

Figure 107: The two growth chamber configurations used for the increase of shield T during GaN growth.

The second approach, pictured in Figure 107, configuration (B), was to keep the shield clamped on the showerhead, but grow the GaN with N_2 as the carrier gas instead of H_2. Although the shield is clamped, neither it nor the showerhead are perfectly flat. This means that there are still some gaps for the carrier gas to pass between the two even when clamped. As N_2 has a much lower thermal conductivity than H_2 (0.024 W/m.K versus 0.168 W/m.K) [179], this insulates the shield from the showerhead by reducing the conduction. In contrast, the transfer of heat from the susceptor to the shield is dominated by radiation when the wafer temperature is above 1000°C and so the nature of the carrier gas has little impact on the heating of the shield. For both experiments the shield temperature is measured using a pyrometer pointing to a solid zone on the backside of the shield.

Samples of configuration (A) were grown in one growth run as shown in Figure 108 (a), while configuration (B) sample had a growth interruption followed by chlorine cleaning, as shown in Figure 108 (b). The GaN regrowth thickness used for configuration (B) is 200 nm, as we have previously shown in chapter 3 that for more than 100 nm of GaN regrowth, the In to Ga conversion rate saturates.

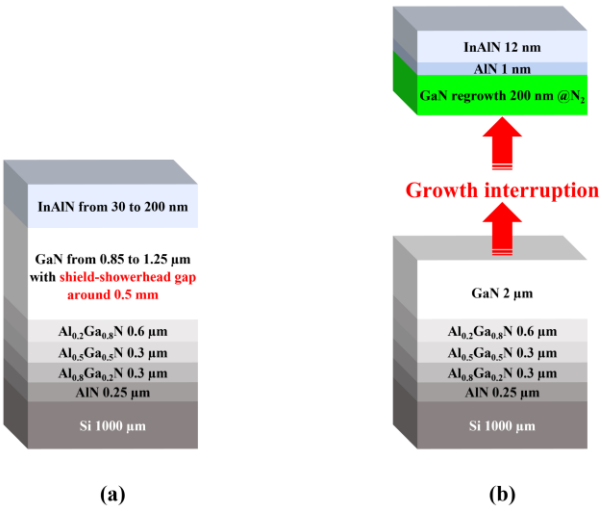

Figure 108: Schematic of grown structures, a) configuration (A) (samples A1 to A7), b) configuration (B) (sample B).

For both configurations, InAlN layers were grown with a chamber pressure of 100 mbar, at 730 °C ± 15 °C, with 15 slm of NH_3. However, differing thicknesses from 12 nm to 200 nm were grown, and the TMIn flows were not identical for all samples. The details of the different samples are shown in Table 14.

Configuration & sample number	Buffer	InAlN thickness (nm)	TMAl / TMIn (sccm)	%Ga in InAlN	Shield T during GaN (°C)
Reference sample [171]	200 nm GaN regrowth under H_2	16	30/125	**20.8**	**190**
A_1	1200 nm GaN	30	30/190	**7.7**	**284**
A_2	1200 nm GaN	30	30/190	**4.7**	**298**
A_3	1250 nm GaN	30	30/190	**5.2**	**299**
A_4	1250 nm GaN	200	20/190	**3.7**	**299**
A_5	850 nm GaN	100	30/190	**3.5**	**305**
A_6	850 nm GaN	100	30/250	**2.9**	**304**
A_7	900 nm GaN	100	30/190	**1.5**	**330**
B	200 nm GaN regrowth under N_2	12	30/125	**2.1**	**278**

Table 14: Description of the samples grown in this study.

For comparison, we include a reference sample from chapter 3, which had a 200 nm of GaN regrowth under H_2. The shield temperature during the GaN regrowth of this sample was 190°C, which had 21% of Ga incorporated into InAlN layers.

Seven samples were grown using configuration (A), A_1 to A_7, growing the entire structure in a single growth for each. The gap between the shield and the showerhead was increased to around 0.5 mm and H_2 was kept as the carrier gas during the GaN growth, as for the reference sample. As previously discussed, the shield to showerhead distance was difficult to accurately reproduce and so, as shown in Table 14, the shield temperature during the GaN growth varied from 284°C to 330°C.

In configuration (B), 200 nm of GaN was regrown under N_2 on a GaN buffer, where, as for the reference sample, we had a growth interruption followed by Cl_2 chamber cleaning. For the first part of the structure before the growth interruption, the GaN was grown under H_2. During the GaN regrowth under N_2, the shield temperature was 278 °C, around 90 °C higher than the reference sample, thanks to the low thermal conductivity of N_2 versus H_2.

Next, we extracted Ga% values from PP-TOFMS measurements at the same sputtering time (and thus distance) into the InAlN layer from the GaN/InAlN interface. This allows a better comparison of these samples, which have different thicknesses.

These values of gallium pollution are plotted against the showerhead temperature during the GaN growth for each sample in Figure 109. The symbol shape relates to the TMIn flow with the triangle, circle and square corresponding to 125 sccm, 190 sccm and 250 sccm respectively. For the samples with configuration A, the size of the symbol scales with the thickness.

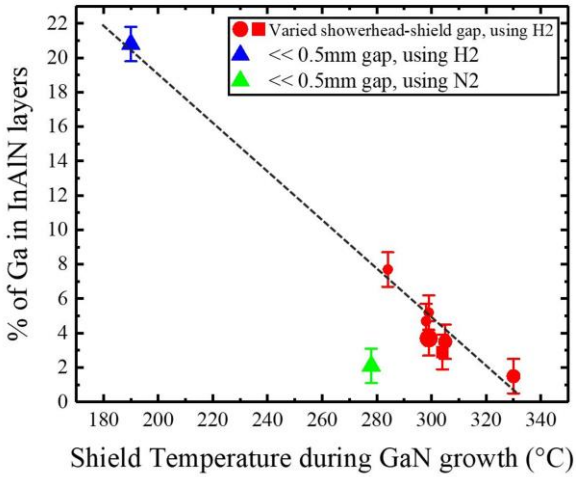

Figure 109: Ga% in InAlN layers as a function of the shield temperature during GaN growth. [180]

We see that despite differing InAlN layer thicknesses and slightly different TMIn flows, a near linear relationship is found between the incorporation of gallium into InAlN layers and the shield temperature during GaN buffer growth for GaN buffer growth under H_2, with higher shield temperature resulting in reduced gallium incorporation into the layers. There appears to be little correlation between the layer thickness and the gallium incorporation.

This confirms our hypothesis that higher shield temperatures during GaN growth would limit the condensation of gallium on the shield, and so reduce the pollution of gallium in InAlN layers.

For GaN growth under N_2, even though the temperature of the shield is a bit lower than when increasing the showerhead-shield distance, there is still a very low incorporation of gallium in InAlN layers of around 2%. This suggests that the temperature is not the only factor influencing the condensation of gallium on the shield during GaN growth but also N_2 as a carrier gas is also affecting the desorption of gallium from GaN buffer. N_2 reduces the gallium desorption from GaN layers compared to H_2 carrier gas and so this double effect gives lower gallium pollution for a given shield temperature.

4PP electrical measurements were performed on sample B, as this sample has an active HEMT heterostructure, and an Rsheet value of 263 Ohm/sq was found. This is a good value

compared to the best AlGaN/GaN based HEMTs values of around 300 Ohm/sq, but not as good as we have found with previous growths.

The GaN regrowth under N_2 is likely to have increased the incorporation of carbon impurities into the 2DEG channel, which are limiting the carrier mobility and so the electrical performance. So, we tried to remedy this problem by performing a GaN growth under N_2 but with a much lower growth rate of 0.5 µm/h compared to the standard growth rate value of 2 µm/h. This lower GaN growth rate should give more time to carbon atoms to leave the GaN grown layer. In addition, we decreased the regrowth temperature of GaN into 1020 °C instead of 1040 °C together with an increase of NH_3 flow into 15000 sccm instead of 10000 sccm to further reduce the gallium desorption during growth.

The AFM and PP-TOFMS measurements for both samples of GaN regrowth under N_2 as shown in Figure 110. We see that with the decrease of GaN growth rate from 2 µm/h to 0.5 µm/h, we find a slightly smoother InAlN surface, with RMS values dropping by 60%, from 0.925 nm down to 0.378 nm. This should lead to a better electrical performance.

With the PP-TOFM depth profiles we see very similar InAlN barriers compositions, however, with nonintentional incorporation of gallium of less than 2%.

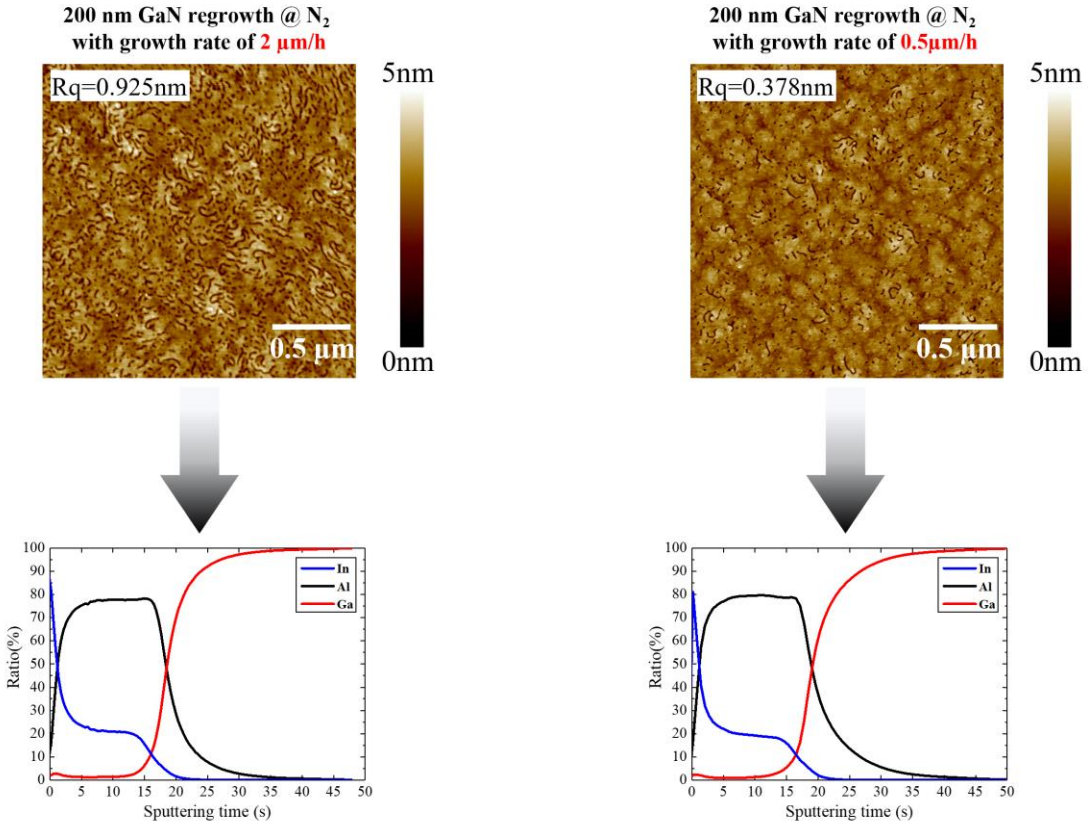

Figure 110: 2µm x 2µm AFM scans with PP-TOFMS measurements for the 200 nm GaN regrowth samples under N_2 with different growth rates.

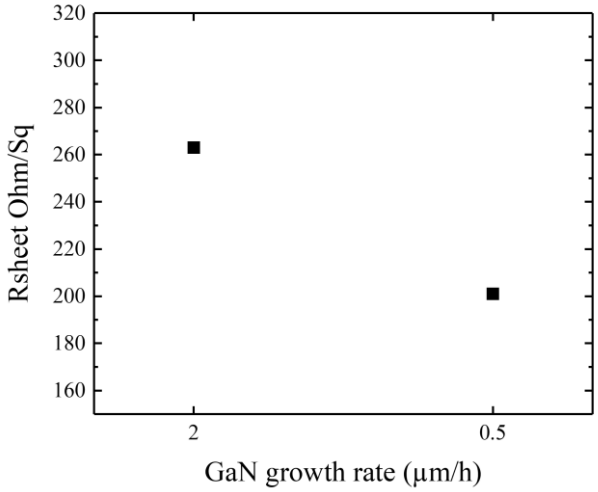

Figure 111: Rsheet measurements for the 200 nm GaN regrowth samples under N_2 with different growth rates.

Electrical measurements by 4PP are shown in Figure 111, where we see we see that the electrical performance of the pure InAlN based HEMT has improved a lot, the Rs value decreasing from 263 Ohm/sq down to 201 Ohm/sq.

With these results, we have achieved the main goal of this PhD work, where we finally managed to overcome the problem of gallium pollution in CCS reactors, and so we managed to grow pure InAlN barriers with excellent electrical performance which is essential for the production of InAlN/GaN based HEMTs. In addition, the growth process of InAlN layers is now practically considered stable, where we see no loss in indium and no unintentional incorporation of gallium into InAlN barriers.

V.3 Conclusion

In this chapter, we have discussed the possibility of overcoming gallium pollution in CCS reactors through the understanding of the main parameters affecting it.

We have shown that by changing the conditions of GaN growth to reduce GaN desorption, we can reduce the gallium pollution in InAlN layers, but only by a factor of around 2. Using AlGaN layers, the gallium pollution is well suppressed, but this is not a solution for electrical devices.

We have shown for the first time the strong link between the temperature of a deposition shield mounted on the front side of the showerhead during the growth of GaN buffers and gallium contamination in InAlN layers. Increasing the shield temperature during GaN buffer growth allowed us to significantly reduce the gallium pollution in our layers. We have found in particular a linear relationship between the increase of shield temperature and the decrease of the Ga% into very low values in InAlN layers when GaN were grown beforehand using H_2 as a carrier gas.

When GaN was grown using N_2 as a carrier gas, the shield temperature was increased by 90 °C higher than for the reference sample (where we used H_2 as a carrier gas), thanks to the low thermal conductivity of N_2 versus H_2. In addition to the reduced desorption of GaN during growth under N_2, this resulted in very low nonintentional incorporation of around 2% into the InAlN barrier. This led us to heterostructures with no gallium pollution and a very low Rsheet value of 201 Ohm/sq.

General conclusion

To initiate these three years of PhD work, we started from the fact that the growth of InAlN barriers on GaN buffers has demonstrated the possibility to surpass the AlGaN on GaN performance for HEMT applications. Currently, the CEA LETI produces GaN based HEMTs on large 200 mm Si(111) wafers using AlGaN barriers. The replacements of the conventional AlGaN/GaN system with InAlN/GaN system requires a good control and reproducibility of the desired growth recipes of such new epitaxial stacks. Yet, a serious obstacle prevents us from achieving this in Close Coupled Showerhead (CCS) MOVPE growth chambers: the non-intentional incorporation of Ga in the ternary InAlN layer during growth. Indeed, gallium pollution within the InAlN barrier affects the structural and electrical properties of these ternary epilayers, hence modifying the properties of the 2DEG.

In the first place, we focused on understanding and quantifying the gallium contamination problem in a CCS tool on the MOVPE growth of InAlN barrier layers. In order to understand the undesirable incorporation of Ga into InAlN barriers, we adopted a growth interruption process where five GaN templates were grown on 200 mm Si(111) wafers without HEMT active structures (AlN spacer + InAlN barrier) before being removed from the AIXTRON tool. The growth chamber is then cleaned, using an in-situ Cl_2 based cleaning, and the growth of the active structures restarted just after a GaN layer regrowth which ranged from 0 nm to 200 nm. From these experiments, we achieved pure InAlN layers without gallium pollution with a direct regrowth of the InAlN layer, without GaN regrowth. For various GaN regrowth thicknesses, we have seen reduced indium incorporation and increased gallium non-intentional incorporation in the InAlN barrier layers along with an increase in the thickness of these layers as the gallium contamination increases, i.e. with the increased GaN regrowth thickness. We proposed a quantitative model for these observations, where we suggest that the TMIn precursor sent to the growth chamber during the growth of InAlN reacts with the metallic gallium pollution on the showerhead shield surface to release TMGa, which is then incorporated as Ga into the InAlN layers.

However, although solving the problem of gallium pollution, the direct regrowth of InAlN layers resulted in poor electrical performance as, while awaiting the regrowth, the wafers were kept in the cleanroom, exposed to air, where potential impurities and oxidation were introduced onto the GaN surface which would form the channel of the 2DEG. To solve this issue, we introduced hydrogen and chlorine etching of the GaN surface after the growth interruption and the Cl_2 cleaning of the chamber, and before the growth of the InAlN layers. The hydrogen etching experiment resulted in good electrical performance and very low non-intentional incorporation of Ga into InAlN barriers. This optimization allowed us to grow almost Ga free InAlN samples with very good Rsheet values as low as 220 Ohm/sq.

Having analyzed the effect of gallium pollution on InAlN layers, we then investigated the effect of Ga pollution on the growth of InGaN layers. This ternary is very interesting for optoelectronic applications, and so the good control of its MOVPE growth in CCS reactors remains crucial for the manufacture of such alloy especially in MQW heterostructures. We have shown that there is a strong effect of the gallium pollution on the MOVPE growth of InGaN layers. As for InAlN layers, the effect is more pronounced both for increased GaN regrowth thicknesses after growth interruption and for higher TMIn flows. We have shown in particular that when working under typical MQW growth conditions, gallium pollution has very strong effects on the thickness of InGaN layers, with an increase of a factor of two. Performing the InGaN growth in a clean chamber shows more easily interpretable results, and more predictable growth behavior, with no change in thickness or composition of InGaN layers when changing the TMIn flows. And so, we see that overcoming the gallium pollution in CCS reactors is very important for the growth of both InAlN and InGaN alloys, for electronics and optoelectronics applications.

In the first analysis of InAlN structure, we proposed a regrowth solution to limit the gallium pollution. However, the growth interruption and the chlorine cleaning are time consuming and they complicate the process for the fabrication of InAlN/GaN HEMTs and so they remain unsuitable for production. This is why we tried to overcome gallium pollution in CCS reactors without having to resort to any growth interruption. We firstly have shown that by changing the growth conditions of GaN buffer layers to reduce Ga desorption, we can reduce the gallium pollution in InAlN layers, but only by a factor of around two. This suggests that the gallium pollution in InAlN layers is linked to the gallium desorption rate

from GaN buffer layers grown beforehand. Alternatively, using AlGaN buffer layers, the gallium pollution is well suppressed, suggesting that with the introduction of Al atoms into GaN buffers we also limit the desorption of gallium atoms, and so we keep the CCS growth chamber clean. However, this is not a solution for electrical devices, as the presence of Al atoms in the buffer degraded the 2DEG channel properties. Next, we showed for the first time the strong link between the temperature of the deposition shield mounted on the front side of the showerhead during the growth of GaN buffer layers and gallium contamination in InAlN layers. Increasing the shield temperature during GaN buffer growth allowed us to significantly reduce the gallium pollution in our barrier layers. We have found in particular a linear relationship between the increase of shield temperature and the decrease of the Ga% into very low values in InAlN layers when GaN were grown beforehand using H_2 as a carrier gas. This suggests that this increase of shield T during GaN buffer growth limited the condensation of gallium on the shield, and so allowed us to then grow InAlN barriers in a clean environment. In another test, when GaN buffer was grown using N_2 as a carrier gas, the shield temperature was increased by 90 °C higher than for the reference sample (where we used H_2 as a carrier gas), thanks to the low thermal conductivity of N_2 versus H_2. In addition to the limited gallium condensation on the shield we have a reduced desorption of Ga from GaN buffers during growth under N_2. This resulted in very low nonintentional incorporation of around 2% into the InAlN barrier.

These results allowed us to grow for the first time in a CCS reactor, InAlN/GaN heterostructures with no gallium pollution and with a very low Rsheet value of 201 Ohm/sq, most importantly with no need to introduce growth interruption. These results are extremely encouraging for the replacement of conventional AlGaN/GaN barriers, with well controlled, pure and higher performance InAlN/GaN barriers for power and RF applications.

In perspective, this work constitutes strong steps toward the replacement of conventional AlGaN/GaN barriers, with well controlled, pure and higher performance InAlN/GaN barriers for power and RF applications. It would also be very interesting at this stage to optimise the growth of protective SiN cap layers on the top of InAlN barriers, in order to protect our indium-based alloys for the next technological steps required to manufacture HEMT components. This would allow the integration of these layers into the latest generation of power transistors and diodes, as well as RF devices.

Another performance boost could be achieved through the doping of InAlN barriers with silicon atoms. We believe that additional silicon doping has the potential to increase the carrier density in the 2DEG channel, and so increase the electrical performance of the HEMT device.

Additionally, as the alloy composition can now be correctly controlled, it would be interesting to pursue this work with the development of InAlGaN quaternary alloys, for the growth of stress free MQWs heterostructures, in particular in combination with AlGaN alloys for UV emission.

Bibliography

[1] T. Matsuoka, H. Okamoto, M. Nakao, H. Harima and E. Kurimoto, "Optical bandgap energy of wurtzite InN," *Applied Physics Letters*, vol. 81, no. 7, pp. 1246-1248, 2002.

[2] D. K. Gaskill, C. D. Brandt and R. J. Nemanich, "III-Nitride, SiC and Diamond Materials for Electronic Devices, Symposium Held April 8-12 1996, San Francisco, California, USA," *MATERIALS RESEARCH SOCIETY PITTSBURGH PA*, vol. 423, 1996.

[3] H. Yamashita, K. Fukui, S. Misawa and S. Yoshida, "Optical properties of AlN epitaxial thin films in the vacuum ultraviolet region," *Journal of Applied Physics*, vol. 50, no. 2, pp. 896-898, 1979.

[4] S. J. Pearton, J. C. Zolper, R. J. Shul and a. F. Ren, "GaN: Processing, defects, and devices," *Journal of Applied Physics*, vol. 86, no. 1, pp. 1-78, 1999.

[5] Z. M. Zhao, R. L. Jiang, P. Chen, D. J. Xi, Z. Y. Luo, R. Zhang, B. Shen, Z. Z. Chen and Y. D. Zheng, "Metal-semiconductor-metal GaN ultraviolet photodetectors on Si(111)," *Applied Physics Letters*, vol. 77, no. 3, pp. 444-446, 2000.

[6] J. C. Carrano, T. Li, D. L. Brown, P. A. Grudowski, C. J. Eiting, R. D. Dupuis and J. C. Campbell, "Very high-speed metal-semiconductor-metal ultraviolet photodetectors fabricated on GaN," *Applied Physics Letters*, vol. 73, no. 17, pp. 2405-2407, 1998.

[7] D. Walker, E. Monroy, P. Kung, J. Wu, M. Hamilton, F. J. Sanchez, J. Diaz and M. Razeghi, "High-speed, low-noise metal-semiconductor-metal ultraviolet photodetectors based on GaN," *Applied Physics Letters*, vol. 74, no. 5, pp. 762-764, 1999.

[8] Q. Chen, M. Asif-Khan, J. W. Yang, C. J. Sun, M. S. Shur and H. Park, "High transconductance heterostructure field-effect transistors based on AlGaN/GaN," *Applied Physics Letters*, vol. 69, no. 6, pp. 794-796, 1996.

[9] Y.-F. Wu, D. Kapolnek, J. P. Ibbetson, P. Parikh, B. P. Keller and U. K. Mishra, "Very-high power density AlGaN/GaN HEMTs," *IEEE Transactions on Electron Devices,* vol. 48, no. 3, pp. 586-590, 2001.

[10] F. Fichter and Z. Anorg, *Chem,* vol. 54, p. 332–327, 1907.

[11] F. Fichter and F. Schroter, "Reports of the German Chemical Society," vol. 43, p. 1465, 1910.

[12] W. Johnson, J. Parson and M. C. Crew, "Nitrogen compounds of gallium. III," *The journal of physical chemistry,* vol. 36, pp. 2561-2654, 1932.

[13] R. Juza and H. Hahn, "Über die Kristallstrukturen von Cu3N, GaN und InN Metallamide und Metallnitride," *Zeitschrift für anorganische und allgemeine Chemie,* vol. 239, no. 3, pp. 282-287, 1938.

[14] H. P. Maruska and J. J. Tietjen, "THE PREPARATION AND PROPERTIES OF VAPOR-DEPOSITED SINGLE-CRYSTAL-LINE GaN," *Appl. Phys. Lett.,* vol. 15, no. 10, pp. 327-329, 1969.

[15] H. Amano, N. Sawaki, I. Akasaki and Y. Toyoda, "Metalorganic vapor phase epitaxial growth of a high quality GaN film using an AlN buffer layer," *Applied Physics Letters,* vol. 48, no. 5, pp. 353-355, 1986.

[16] H. Amano, M. Kito, K. Hiramatsu and I. Akasaki, "P-Type Conduction in Mg-Doped GaN Treated with Low-Energy Electron Beam Irradiation (LEEBI)," *Japanese Journal of Applied Physics,* vol. 28 Part 2, no. 12, p. L2112–L2114, 1989.

[17] M. A. Khan, J. M. V. Hove, J. N. Kuznia and D. T. Olson, "High electron mobility GaN/AlxGa1-xN heterostructures grown by low-pressure metalorganic chemical vapor deposition," *Applied Physics Letters,* vol. 58, no. 21, p. 2408–2410, 1991.

[18] M. A. Khan, J. N. Kuznia, A. R. Bhattarai and D. T. Olson, "Metal semiconductor field effect transistor based on single crystal GaN," *Applied Physics Letters,* vol. 62, no. 15, p. 1786–1787, 1993.

[19] M. A. Khan, J. N. Kuznia, D. T. Olson, W. J. Schaff, J. W. Burm and M. S. Shur, "Microwave performance of a 0.25 μm gate AlGaN/GaN heterostructure field effect transistor," *Applied Physics Letters,* vol. 65, no. 9, p. 1121–1123, 1994.

[20] S. Nakamura, M. Senoh and T. Mukai, "P-GaN/N-InGaN/N-GaN Double-Heterostructure Blue-Light-Emitting Diodes," *Japanese Journal of Applied Physics,* vol. 32, no. 1A/B, p. L8–L11, 1993.

[21] M. Meneghini, G. Meneghesso and E. Zanoni, *Power GaN Devices, Springer International Publishing,Cham, doi:10.1007/978-3-319-43199-4,* 2017.

[22] S. Kasap and C. Peter, "Springer Handbook of Electronic and Photonic Materials," ISBN: 978-3-319-48931-5, 2017.

[23] T. Hanada, "Basic properties of ZnO, GaN, and related materials.," Oxide and nitride semiconductors , Springer, Berlin, Heidelberg, 2009.

[24] A. L. Allred, "Electronegativity values from thermochemical data," *Journal of inorganic and nuclear chemistry,* vol. 17, no. 3-4, pp. 215-221, 1961.

[25] F. Bernardini, V. Fiorentini and D. Vanderbilt, "Spontaneous polarization and piezoelectric constants of III-V nitrides," *Physical Review B,* vol. 56, no. 16, p. R10024, 1997.

[26] W. Gian, M. Skowronski and G. S. Rohrer, "Structural defects and their relationship to nucleation of GaN thin films," *MRS Online Proceedings Library Archive,* vol. 423, 1996.

[27] I. Pichugin and M. Tiachala, "M. Izv. Akad. Nauk SSSR," *Neorg. Mater,* vol. 14, p. 175, 1978.

[28] L. Xinjiao, X. Zechuan, H. Ziyou, C. H'uazhe, S. Wuda, C. Zhongcai, Z. Feng and W. Enguang, "On the properties of AlN thin films grown by low temperature reactive rf sputtering," *Thin Solid Films,* vol. 139, no. 3, pp. 261-274, 1986.

[29] L. E. McNeil, M. Grimsditch and R. H. French, " Vibrational spectroscopy of aluminum nitride," *Journal of the American Ceramic Society,* vol. 76, no. 5, pp. 1132-1136, 1993.

[30] A. D. Bykhovski, B. L. Gelmont and M. S. Shur, "Elastic strain relaxation and piezoeffect in GaN-AlN, GaN-AlGaN and GaN-InGaN superlattices," *Journal of Applied Physics,* vol. 81, no. 9, pp. 6332-6338, 1997.

[31] A. Polian, M. Grimsditch and I. Grzegory, "Elastic constants of gallium nitride," *Journal of Applied Physics,* vol. 79, no. 6, pp. 3343-3344, 1996.

[32] A. U. Sheleg and V. A. Savastenko, "Determination of elastic constants of hexagonal crystals from measured values of dynamic atomic displacements," *Inorganic Materials,* vol. 15, no. 1, pp. 1257-1260, 1979.

[33] S. Arulkumaran, T. Egawa, H. Ishikawa and T. Jimbo, "Characterization of different-Al-content Al x Ga 1–x N/GaN heterostructures and high-electron-mobility transistors on sapphire," *J. Vacuum Sci. Technol. B,* vol. 21, no. 2, pp. 888-894, 2003.

[34] E. Zanoni, M. Meneghini, A. Chini, D. Marcon and G. Meneghesso, "AlGaN/GaN-based HEMTs failure physics and reliability: mechanisms affecting gate edge and Schottky junction," *IEEE Trans. Electron Dev. ,* vol. 60 , no. 10, pp. 3119-3131, 2013.

[35] J. Kuzmík, "Power electronics on InAlN/(In) GaN: prospect for a record performance," *IEEE Electron Dev. Lett.,* vol. 22, no. 11, pp. 510-512, 2001.

[36] F. Medjdoub, J.-F. Carlin, M. Gonschorek, E. Feltin, M. Py, D. Ducatteau, C. Gaquiere, N. Grandjean and E. Kohn, "Can InAlN/GaN be an alternative to high power/high temperature AlGaN/GaN devices?," *In 2006 International Electron Devices Meeting ,* pp. 1-4, 2006.

[37] O. Ambacher, J. Majewski, C. Miskys, A. Link, M. Hermann, M. Eickhoff, M. Stutzmann, F. Bernardini, V. Fiorentini, V. Tilak, B. Schaff and L. F. Eastman, "Pyroelectric properties of Al (In) GaN/GaN hetero-and quantum well structures," *Journal of physics: condensed matter,* vol. 14, no. 13, p. 3399, 2002.

[38] O. Ambacher, R. Dimitrov, M. Stutzmann, B. E. Foutz, M. J. Murphy, J. A. Smart, J. R. Shealy, N. G. Weimann, K. Chu, M. Chumbes, B. Green, A. J. Sierakowski, W. J. Schaff and L. F. Eastman, "Role of Spontaneous and Piezoelectric Polarization Induced Effects in Group-III Nitride Based Heterostructures and Devices," *physica status solidi (b),* vol. 216, no. 1, pp. 381-389, 1999.

[39] T. M. Tigran, E. L. Michael, I. P. Lubov, N. Y. Sergey, S. S. Grigory and K. M. Asif, "Carrier mobility model for GaN," *Solid-State Electronics,* vol. 47, no. 1, pp. 111-115, 2003.

[40] R. Trew, "SiC and GaN transistors - is there one winner for microwave power applications?," *Proceedings of the IEEE,* vol. 90, pp. 1032-1047, 2002.

[41] M. Farahmand, C. Garetto, E. Bellotti, K. F. Brennan, M. Goano, E. Ghillino, G. Ghione, J. D. Albrecht and P. P. Ruden, "Monte carlo simulation of electron transport in the III-nitride wurtzite phase materials system: binaries and ternaries," *Electron Devices, IEEE,* vol. 48, pp. 535-542, 2001.

[42] T. P. Chow, V. Khemka, J. Fedison, N. Ramungul, K. Matocha, Y. Tang and R. J. Gutmann, "SiC and GaN bipolar power devices," *Solid-State Electronics,* vol. 44, no. 2, pp. 277-301, 2000.

[43] G. A. Slack, R. A. Tanzilli, R. O. Pohl and J. W. Vandersande, "The intrinsic thermal conductivity of AIN," *Journal of Physics and Chemistry of Solids,* vol. 48, no. 7, pp. 641-647, 1987.

[44] Z. Dziuba, J. Antoszewski, J. M. Dell, L. Faraone, P. Kozodoy, S. Keller, B. Keller, S. P. DenBaars and U. K. Mishra, "Magnetic field dependent Hall data analysis of electron transport in modulation-doped AlGaN/GaN heterostructures," *Journal of applied physics,* vol. 82, no. 6, pp. 2996-3002, 1997.

[45] C. Alain and M. Pascal, "Ecole polytechnique universitaire de marseille, departement micro-electronique et telecomunications," *Physique des semi-conducteurs,* 2004/2005.

[46] E. Johnson, "Physical limitations on frequency and power parameters of transistors," *BCA Electronic Components and Devices,* vol. 13, pp. 27-34, 1965.

[47] R. W. Keyes, "Figure of merit for semiconductors for high-speed switches," *Proceedings of the IEEE,* vol. 60, no. 2, pp. 225-225, 1972.

[48] B. J. Baliga, "Semiconductors for high-voltage, vertical channel field-effect transistors," *Journal of applied Physics,* vol. 53, no. 3, pp. 1759-1764, 1982.

[49] B. J. Baliga, "Power semiconductor device figure of merit for high-frequency applications," *IEEE Electron Device Letters,* vol. 10, no. 10, pp. 455-457, 1989.

[50] *National Research Council. Materials for high-temperature semiconductor devices. National Academies Press.,* 28 sept. 1995.

[51] A. T. Schremer, J. A. Smart, Y. Wang, O. Ambacher, N. C. MacDonald and J. R. Shealy, "High electron mobility AlGaN/GaN heterostructure on (111) Si," *Applied Physics Letters,* vol. 76, no. 6, pp. 736-738, 2000.

[52] F. Semond, Y. Cordier, N. Grandjean, F. Natali, B. Damilano, S. Vézian and J. Massies, "Molecular Beam Epitaxy of Group-III Nitrides on Silicon Substrates: Growth, Properties and Device Applications," *physica status solidi (a),* vol. 188, no. 2, pp. 501-510, 2001.

[53] T. Li, M. Mastro and A. Dadgar, "III–V compound semiconductors: integration with silicon-based microelectronics," *CRC press,* 2010.

[54] M. Higashiwaki, T. Mimura and T. Matsui, "Millimeter-wave GaN HFET technology," *Proc. SPIE 6894, Gallium Nitride Materials and Devices III, 68941L,* 15 February 2008.

[55] Y. Cao and D. Jena, "High-mobility window for two-dimensional electron gases at ultrathin Al N⁄ Ga N heterojunctions," *Applied physics letters,* vol. 90, no. 18, p. 182112, 2007.

[56] J. Kuzmík, "Power electronics on InAlN/(In) GaN: Prospect for a record performance," *IEEE Electron Device Letters,* vol. 22, no. 11, pp. 510-512, 2001.

[57] H. Sun, A. R. Alt, H. Benedickter, E. Feltin, J. F. Carlin, M. Gonschorek, N. Grandjean and C. R. Bolognesi, "205-GHz (Al, In) N/GaN HEMTs," *IEEE Electron Device Letters,* vol. 31, no. 9, pp. 957-959, 2010.

[58] F. Medjdoub, M. Alomari, J. F. Carlin, M. Gonschorek, E. Feltin, M. A. Py, N. Grandjean and E. Kohn, "Barrier-layer scaling of InAlN/GaN HEMTs," *IEEE Electron device letters,* vol. 29, no. 5, pp. 422-425, 2008.

[59] F. Medjdoub, J. F. Carlin, C. Gaquière, N. Grandjean and E. Kohn, "Status of the emerging InAlN/GaN power HEMT technology," *Open Elec. Electron. Eng. J.,* vol. 2, no. 1, pp. 1-7, 2008.

[60] S. W. Kaun, E. Ahmadi, B. Mazumder, F. Wu, E. C. Kyle, P. G. Burke, U. Mishra and J. S. Speck, " GaN-based high-electron-mobility transistor structures with homogeneous lattice-matched InAlN barriers grown by plasma-assisted molecular beam epitaxy," *Semiconductor Science and Technology,* vol. 29, no. 4, p. 045011, 2014.

[61] A. Yamada, T. Ishiguro, J. Kotani and N. Nakamura, "Electron mobility enhancement in metalorganic-vapor-phase-epitaxy-grown InAlN high-electron-

mobility transistors by control of surface morphology of spacer layer," *Japanese Journal of Applied Physics,* vol. 57, no. 1S, p. 01AD01, 2017.

[62] O. Laboutin, Y. Cao, R. Wang, G. Li, D. Jena, H. Xing, C. Lo, L. Liu, S. Pearton, F. Ren and W. Johnson, "The Resurgence of III-N Materials Development: AlInN HEMTs and GaN-on-Si," *ECS Transactions,* vol. 41, no. 8, pp. 301-311, 2011.

[63] S. W. Kaun, E. Ahmadi, B. Mazumder, F. Wu, E. C. Kyle, P. G. Burke, U. Mishra and J. S. Speck, "GaN-based high-electron-mobility transistor structures with homogeneous lattice-matched InAlN barriers grown by plasma-assisted molecular beam epitaxy," *Semiconductor Science and Technology,* vol. 29, no. 4, p. 045011, 2014.

[64] M. Higashiwaki and T. Matsui, "InAlN/GaN heterostructure field-effect transistors grown by plasma-assisted molecular-beam epitaxy," *Japanese journal of applied physics,* vol. 43, no. 6B, p. L768, 2004.

[65] M. Higashiwaki and T. Matsui, "MBE growth and device characteristics of InAlN/GaN HFETs," *physica status solidi (c),* vol. 2, no. 7, pp. 2598-2601, 2005.

[66] F. Medjdoub, J. F. Carlin, M. Gonschorek, M. A. Py, N. Grandjean, S. Vandenbrouck, C. Gaquiere, J. Dejaeger and E. Kohn, " Small-signal characteristics of AlInN/GaN HEMTs," *Electronics Letters,* vol. 42, no. 13, pp. 779-780, 2006.

[67] M. Gonschorek, J. F. Carlin, E. Feltin, M. A. Py and N. Grandjean, "High electron mobility lattice-matched Al In N⁄ Ga N field-effect transistor heterostructures," *Applied physics letters,* vol. 89, no. 6, p. 062106, 2006.

[68] N. Y. H. H. M. O. Y. K. T. &. Y. T. Watanabe, " High-quality InAlN/GaN high electron mobility transistors on Si (111) by metalorganic chemical vapor deposition," *IEEE Compound Semiconductor Integrated Circuit Symposium,* pp. 257-260, 2006.

[69] F. Medjdoub, N. Sarazin, M. Tordjman, M. Magis, M. A. di Forte-Poisson, M. Knez, E. Delos, G. Gaquire and E. Kohn, "Characteristics of Al2O3/AlInN/GaN MOSHEMT," *Electronics letters,* vol. 43, no. 12, pp. 691-692, 2007.

[70] K. Jeganathan, M. Shimizu, H. Okumura, Y. Yano and N. Akutsu, "Lattice-matched InAlN/GaN two-dimensional electron gas with high mobility and sheet carrier

density by plasma-assisted molecular beam epitaxy," *Journal of crystal growth,* vol. 304, no. 2, pp. 342-345, 2007.

[71] G. H. Jessen, J. K. Gillespie, G. D. Via, A. Crespo, D. Langley, M. E. Aumer, C. Ward, H. Henry, D. Thomson and D. P. Partlow, "RF power measurements of InAlN/GaN unstrained HEMTs on SiC substrates at 10 GHz," *IEEE electron device letters,* vol. 28, no. 5, pp. 354-356, 2007.

[72] F. Medjdoub, M. Alomari, J. F. Carlin, M. Gonschorek, E. Feltin, M. A. Py, C. Gaquiere and E. Kohn, "Effect of fluoride plasma treatment on InAlN/GaN HEMTs," *Electronics Letters,* vol. 44, no. 11, pp. 696-698, 2008.

[73] M. Hiroki, N. Maeda and T. Kobayashi, "Fabrication of an InAlN/AlGaN/AlN/GaN heterostructure with a flat surface and high electron mobility," *Applied physics express,* vol. 1, no. 11, p. 111102, 2008.

[74] J. P. G. Kuzmik, S. Abermann, J. F. Carlin, M. Gonschorek, E. Feltin, N. Grandjean, E. Bertagnolli, G. Strasser and D. Pogany, "Technology and Performance of InAlN/AlN/GaN HEMTs With Gate Insulation and Current Collapse Suppression Using ZrO2 or HfO2," *IEEE Transactions on Electron Devices,* vol. 55, no. 3, pp. 937-941, 2008.

[75] L. Rahimzadeh Khoshroo, C. Mauder, W. Zhang, M. Fieger, M. Eickelkamp, Y. Dikme, J. Woitok, P. Niyamakom, A. Vescan, H. Kalisch, M. Heuken and M. Heuken, "Optimisation of AlInN/GaN HEMT structures," *physica status solidi c,* vol. 5, no. 6, pp. 2041-2043, 2008.

[76] C. Ostermaier, G. Pozzovivo, J. F. Carlin, B. Basnar, W. Schrenk, Y. Douvry, C. Gaquière, J. DeJaeger, K. Cico, K. Frohlich, M. Gonschorek, N. Grandjean, G. Strasser, D. Pogany and J. Kuzmik, "Ultrathin InAlN/AlN barrier HEMT with high performance in normally off operation," *IEEE Electron Device Letters,* vol. 30, no. 10, pp. 1030-1032, 2009.

[77] S. Zhang, M. C. Li, Z. H. Feng, B. Liu, J. Y. Yin and L. C. Zhao, "High electron mobility and low sheet resistance in lattice-matched AlInN/AlN/GaN/AlN/GaN double-channel heterostructure," *Applied Physics Letters,* vol. 95, no. 21, p. 212101, 2009.

[78] H. Behmenburg, L. R. Khoshroo, M. Eickelkamp, C. Mauder, M. Fieger, N. Ketteniss, J. Woitok, D. Wamwangi, M. Wuttig, S. Estevez Hernandez, T. Schäpers, M. Heuken, A. Vescan, H. Kalisch and R. Jansen, "Influence of barrier thickness on AlInN/AlN/GaN heterostructures and device properties," *physica status solidi c,* vol. 6, no. S2 2, pp. S1041-S1044, 2009.

[79] R. Tülek, A. Ilgaz, S. Gökden, A. Teke, M. K. Öztürk, M. Kasap, S. Özçelik, E. Arslan and E. Özbay, " Comparison of the transport properties of high quality AlGaN/AlN/GaN and AlInN/AlN/GaN two-dimensional electron gas heterostructures," *Journal of Applied Physics,* p. 013707, 2009.

[80] N. Sarazin, E. Morvan, M. A. di Forte Poisson, M. Oualli, C. Gaquiere, O. Jardel, O. Drisse, M. Tordjman, M. Magis and S. L. Delage, "AlInN/AlN/GaN HEMT technology on SiC with 10-W/mm and 50% PAE at 10 GHz," *IEEE Electron Device Letters,* vol. 31, no. 1, pp. 11-13, 2009.

[81] A. Crespo, M. M. Bellot, K. D. Chabak, J. K. Gillespie, G. H. Jessen, V. Miller, M. Trejo, G. Via, D. Walker, B. Winningham, H. Smith, T. Cooper, X. Gao and S. Guo, "High-power Ka-band performance of AlInN/GaN HEMT with 9.8-nm-thin barrier," *IEEE Electron Device Letters,* vol. 31, no. 1, pp. 2-4, 2009.

[82] M. Mikulics, R. Stoklas, A. Dadgar, D. Gregušová, J. Novák, D. Grützmacher, A. Krost and P. Kordoš, "InAlN/GaN/Si heterostructures and field-effect transistors with lattice matched and tensely or compressively strained InAlN," *Applied physics letters,* vol. 97, no. 17, p. 173505, 2010.

[83] K. Cheng, S. Degroote, M. Leys, F. Medjdoub, J. Derluyn, B. Sijmus, M. Germain and G. Borghs, "Very low sheet resistance AlInN/GaN HEMT grown on 100 mm Si (111) by MOVPE," *physica status solidi c,* vol. 7, no. 7-8, pp. 1967-1969, 2010.

[84] A. Crespo, M. Bellott, K. Chabak, J. K. Gillespie, G. H. Jessen, M. Kossler, V. Trimble, M. Trejo, G. Via, B. Winningham, H. Smith, H. Walker, T. Cooper, X. Gao and S. Guo, "High frequency performance of Ga free barrier AlInN/GaN HEMT," *physica status solidi c,* vol. 7, no. 10, pp. 2433-2435, 2010.

[85] Q. Fareed, A. Tarakji, J. Dion, M. Islam, V. Adivarahan and A. Khan, "High voltage operation of field-plated AlInN HEMTs," *physica status solidi c,* vol. 8, no. 7-8, pp. 2454-2456, 2011.

[86] D. Morgan, M. Sultana, H. Fatima, S. Sugiyama, Q. Fareed, V. Adivarahan, M. Lachab and A. Khan, "Enhancement-mode insulating-gate AlInN/AlN/GaN heterostructure field-effect transistors with threshold voltage in excess of+ 1.5 V," *Applied Physics Express,* vol. 4, no. 11, p. 114101, 2011.

[87] F. Lecourt, N. Ketteniss, H. Behmenburg, N. Defrance, V. Hoel, M. Eickelkamp, A. Vescan, C. Giesen, M. Heuken and J. De Jaeger, "InAlN/GaN HEMTs on sapphire substrate with 2.9-W/mm output power density at 18 GHz," *IEEE Electron Device Letters,* vol. 32, no. 11, pp. 1537-1539, 2011.

[88] F. Medjdoub, M. Zegaoui, D. Ducatteau, N. Rolland and P. A. Rolland, "High-performance low-leakage-current AlN/GaN HEMTs grown on silicon substrate," *IEEE Electron Device Letters,* vol. 32, no. 7, pp. 874-876, 2011.

[89] H. Behmenburg, C. Giesen, R. Srnanek, J. Kovac, H. Kalisch, M. Heuken and R. H. Jansen, "Investigation of AlN buffer layers on 6H-SiC for AlInN HEMTs grown by MOVPE," *Journal of Crystal Growth,* vol. 316, no. 1, pp. 42-45, 2011.

[90] M. Hoi Wong, F. Wu, C. A. Hurni, S. Choi, J. S. Speck and U. K. Mishra, "Molecular beam epitaxy of InAlN lattice-matched to GaN with homogeneous composition using ammonia as nitrogen source," *Applied Physics Letters,* vol. 100, no. 7, p. 072107, 2012.

[91] Z. Feng, B. Liu, J. Yin, J. Wang, G. Gu, S. Dun and S. Cai, "10-GHz 4.69-W/mm InAlN/GaN HFET on sapphire substrate," *physica status solidi c,* vol. 9, no. 3-4, pp. 855-857, 2012.

[92] J. Xue, J. Zhang, Y. Hou, H. Zhou, J. Zhang and Y. Hao, "Pulsed metal organic chemical vapor deposition of nearly latticed-matched InAlN/GaN/InAlN/GaN double-channel high electron mobility transistors," *Applied Physics Letters,* vol. 100, no. 1, p. 013507, 2012.

[93] J. Lu, D. Denninghoff, R. Yeluri, S. Lal, G. Gupta, M. Laurent, S. Keller, S. DenBaars and U. Mishra, "Very high channel conductivity in ultra-thin channel N-polar GaN/(AlN, InAlN, AlGaN) high electron mobility hetero-junctions grown by metalorganic chemical vapor deposition," *Applied Physics Letters,* vol. 102, no. 23, p. 232104, 2013.

[94] L. Bo, F. Zhihong, D. Shaobo, Z. Xiongwen, G. Guodong, W. Yuangang, X. Peng, H. Zezhao and C. Shujun, " An extrinsic fmax> 100 GHz InAlN/GaN HEMT with AlGaN back barrier," *Journal of Semiconductors,* vol. 34, no. 4, p. 044006, 2013.

[95] L. Lugani, M. A. Py, J. F. Carlin and N. Grandjean, "Leakage mechanisms in InAlN based heterostructures," *Journal of Applied Physics,* vol. 115, no. 7, p. 074506, 2014.

[96] J. J. Freedsman, A. Watanabe, T. Ito and T. Egawa, "Recessed gate normally-OFF Al2O3/InAlN/GaN MOS-HEMT on silicon," *Applied Physics Express,* vol. 7, no. 10, p. 104101, 2014.

[97] J. M. A. T. M. G. P. L. C. d. F.-P. M. A. &. R. N. Bergsten, "Low resistive Au-free, Ta-based, recessed ohmic contacts to InAlN/AlN/GaN heterostructures," *Semiconductor Science and Technology,* vol. 30, no. 10, p. 105034, 2015.

[98] F. Medjdoub, R. Kabouche, A. Linge, B. Grimbert, M. Zegaoui, P. Gamarra, C. Lacam, M. Tordjman and M. A. di Forte-Poisson, "High electron mobility in high-polarization sub-10 nm barrier thickness InAlGaN/GaN heterostructure," *Applied Physics Express,* vol. 8, no. 10, p. 101001, 2015.

[99] J. I. Chyi, Y. M. Hsin, G. Y. Lee and H. C. Chiu, "Investigations and Improvements of AlInN/GaN HEMTs Grown on Si," *ECS Transactions,* vol. 66, no. 1, pp. 217-222, 2015.

[100] A. Watanabe, J. J. Freedsman, Y. Urayama, D. Christy and T. Egawa, "Thermal stability of an InAlN/GaN heterostructure grown on silicon by metal-organic chemical vapor deposition," *Journal of Applied Physics,* vol. 118, no. 23, p. 235705, 2015.

[101] A. Yamada, T. Ishiguro, J. Kotani, S. Tomabechi, N. Nakamura and K. Watanabe, "Advantages of the AlGaN spacer in InAlN high-electron-mobility transistors grown using metalorganic vapor phase epitaxy," *Japanese Journal of Applied Physics,* vol. 55, no. 5S, p. 05FK03, 2016.

[102] M. Chunlei, G. Guodong and L. Yuanjie, "A high performance InAlN/GaN HEMT with low Ron and gate leakage," *Journal of Semiconductors,* vol. 37, no. 2, p. 024009, 2016.

[103] R. Aubry, J. C. Jacquet, M. Oualli, O. Patard, S. Piotrowicz, E. Chartier, N. Michel, L. T. Xuan, D. Lancereau, C. Potier, M. Magis, P. Gamarra, C. Lacam, M. Tordjman, O. Jardel, C. Dua and S. Delage, "ICP-CVD SiN passivation for high-power RF InAlGaN/GaN/SiC HEMT," *IEEE Electron Device Letters,* vol. 37, no. 5, pp. 629-632, 2016.

[104] E. Dogmus, R. Kabouche, S. Lepilliet, A. Linge, M. Zegaoui, H. Ben-Ammar, M. Chauvat, P. Ruterana, P. Gamarra, C. Lacam, M. Tordjman and F. Medjdoub, "InAlGaN/GaN HEMTs at cryogenic temperatures," *Electronics,* vol. 5, no. 2, p. 31, 2016.

[105] S. Çörekçi, S. Dugan, M. K. Öztürk, S. Ş. Çetin, M. Çakmak, S. Özçelik and E. Özbay, "Characterization of AlInN/AlN/GaN Heterostructures with Different AlN Buffer Thickness," *Journal of Electronic Materials,* vol. 45, no. 7, pp. 3278-3284, 2016.

[106] M. T. Hardy, B. P. Downey, N. Nepal, D. F. Storm, D. S. Katzer and D. J. Meyer, "Epitaxial ScAlN grown by molecular beam epitaxy on GaN and SiC substrates," *Applied Physics Letters,* vol. 110, no. 16, p. 162104, 2017.

[107] J. Zhang, X. Yang, J. Cheng, Y. Feng, P. Ji, A. Hu, F. Xu, N. Tang, X. Wang and B. Shen, "Enhanced transport properties in InAlGaN/AlN/GaN heterostructures on Si (111) substrates: The role of interface quality," *Applied Physics Letters,* vol. 110, no. 17, p. 172101, 2017.

[108] J. Kotani, A. Yamada, T. Ishiguro, H. Yamaguchi and N. Nakamura, "Suppression of gate leakage current in in-situ grown AlN/InAlN/AlN/GaN heterostructures based on the control of internal polarization fields," *Journal of Applied Physics,* vol. 121, no. 11, p. 115704, 2017.

[109] W. Wang, X. Yu, J. Zhou, D. Chen, K. Zhang, C. Kong, Y. Kong, Z. Li and T. Chen, "Improvement of power performance of GaN HEMT by using quaternary InAlGaN barrier," *IEEE Journal of the Electron Devices Society,* vol. 6, pp. 360-364, 2018.

[110] F. Lumbantoruan, X. X. Zheng, J. H. Huang, R. Y. Huang, F. Mangasa, E. Y. Chang, Y. Tu and C. T. Lee, "Structural and electrical properties analysis of InAlGaN/GaN heterostructures grown at elevated temperatures by MOCVD," *Journal of Crystal Growth,* vol. 501, pp. 7-12, 2018.

[111] J. H. Hwang, M. Jang, J. Park and J. H. Jang, "Quaternary In0.05Al0.70Ga0.25N/GaN HEMTs With On-Resistance of 0.97 Ω·mm," *Compound Semiconductor Week (CSW)*, pp. 1-2, 2018.

[112] M. Tsukui, Y. Iyechika, H. Nago and H. Takahashi, "Uniformity and repeatability of InAlN-barrier HEMTs growth by high-speed-rotation single-wafer MOCVD tool," *Journal of Crystal Growth*, vol. 509, pp. 103-106, 2019.

[113] M. Hiroki, Y. Oda, N. Watanabe, N. Maeda, H. Yokoyama, K. Kumakura and H. Yamamoto, "Unintentional Ga incorporation in metalorganic vapor phase epitaxy of In-containing III-nitride semiconductors," *Journal of Crystal Growth*, vol. 382, pp. 36-40, 2013.

[114] J. Lu, J. Su, R. Arif, G. D. Papasouliotis and A. Paranjpe, "Epitaxial Growth of InAlN/GaN Heterostructures on Silicon Substrates in a Single Wafer Rotating Disk MOCVD Reactor," *MRS Advances*, vol. 2, no. 5, pp. 329-334, 2017.

[115] E. Taylor, M. D. Smith, T. C. Sadler, K. Lorenz, H. N. Li, E. Alves, P. Parbrook and R. W. Martin, "Structural and optical properties of Ga auto-incorporated InAlN epilayers," *Journal of Crystal Growth*, vol. 408, pp. 97-101, 2014.

[116] S. Choi, H. J. Kim, Z. Lochner, J. Kim, R. D. Dupuis, A. M. Fischer, R. Juday, Y. Huang, T. Li, J. Huang, F. Ponce and J. Ryou, "Origins of unintentional incorporation of gallium in AlInN layers during epitaxial growth, part I: Growth of AlInN on AlN and effects of prior coating," *Journal of Crystal Growth*, vol. 388, pp. 137-142, 2014.

[117] J. Kim, Z. Lochner, M. H. Ji, S. Choi, H. J. Kim, J. S. Kim, R. D. Dupuis, R. Juday, Y. Huang, T. Li, J. Y. Huang, F. A. Ponce and J. H. Ryou, "Origins of unintentional incorporation of gallium in InAlN layers during epitaxial growth, part II: Effects of underlying layers and growth chamber conditions," *Journal of Crystal Growth*, vol. 388, pp. 143-149, 2014.

[118] Y. Guo, X. L. Liu, H. P. Song, A. L. Yang, X. Q. Xu, G. L. Zheng, H. Wei, S. Yang, Q. Zhu and Z. G. Wang, "A study of indium incorporation in In-rich InGaN grown by MOVPE," *Applied Surface Science*, vol. 256, no. 10, pp. 3352-3356, 2010.

[119] G. Laval, "Croissance sélective de pseudo-substrats de GaN sur silicium pour des applications optoélectroniques," *Doctoral dissertation, Université Grenoble Alpes,* 2017.

[120] G. B. Stringfellow, "Organometallic Vapor-Phase Epitaxy: Theory and Practice," *Elsevier,* 1999.

[121] D. H. Reep and S. K. Ghandhi, "Electrical Properties of Organometallic Chemical Vapor Deposited GaAs Epitaxial Layers Temperature Dependence," *Journal of The Electrochemical Society,* vol. 131, no. 11, pp. 2697-2702, 1984.

[122] C. Plass, H. Heinecke, O. Kayser, H. Lüth and P. Balk, " A comparative study of Ga (CH3) 3, Ga (C2H5) 3 and Ga (C4H9) 3 in the low pressure MOCVD of GaAs," *Journal of Crystal Growth,* vol. 88, no. 4, pp. 455-464, 1988.

[123] H. Kräutle, H. Roehle, A. Escobosa and H. Beneking, "Investigations on low temperature mo-cvd growth of GaAs," *Journal of Electronic Materials,* vol. 12, no. 1, pp. 215-222, 1983.

[124] M. B. Charles, "MOVPE growth and characterisation of III-nitrides on silicon," *Doctoral dissertation, University of Cambridge,* 2006.

[125] S. Fujieda, M. Masashi and M. Yoshishige, "Growth Characterization of Low-Temperature MOCVD GaN–Comparison between N2H4 and NH3," *Japanese journal of applied physics,* vol. 26, no. 12, p. 2067, 1987.

[126] Z. Kun, I. Masao, L. Jianping, Z. Shuming, L. Zengcheng, F. Meixin, T. Aiqin, W. Pengyan, L. Deyao, Z. Liqun and Y. Hui, "Abnormal InGaN growth behavior in indium-desorption regime in metalorganic chemical vapor deposition," *Journal of crystal growth,* vol. 409, pp. 51-55, 2015.

[127] B. H. Cardelino and C. A. Cardelino, "Dissociative Chemisorption of Trimethylgallium, Trimethylindium, and Ammonia on Gallium and Indium Nitride Substrates. A Computational Study.," *The Journal of Physical Chemistry C,* vol. 115, no. 18, pp. 9090-9104, 2011.

[128] D. W. Jenkins, J. D. Dow and M. H. Tsai, "N vacancies in Al x Ga1− x N," *Journal of applied physics,* vol. 72, no. 9, pp. 4130-4133, 1992.

[129] C. Matthew, B. Yannick, B. Sandra, E. René, G. Gennie, K. Joël, L. Julie and V. William, "The effect of AlN nucleation temperature on inverted pyramid defects in GaN layers grown on 200 mm silicon wafers," *Journal of Crystal Growth*, vol. 464, pp. 164-167, 2017.

[130] J. Lehmann, C. Leroux, M. Charles, A. Torres, E. Morvan and G. Reimbold, "Influence of epitaxy and gate deposition process on ron resistance of algan/gan-on-si HEMT," *EEE 27th International Symposium on Power Semiconductor Devices & IC's (ISPSD). IEEE*, pp. 261-264, 2015.

[131] "https://www.ph.tum.de/academics/org/labs/fopra/docs/userguide-42.en.pdf".

[132] G. Ihsan, V. Aydin, K. Sertac and B. Cagatay, "Adaptive Q-control for Tapping-mode Nano Scanning Using a Piezo-actuated Bimorph Probe," *College of Engineering, Koc University, Istanbul, Turkey, 34450,* 2012.

[133] P. Marotel, "Spectroscopie optique de l'oxyde de zinc. Diss.," 2011.

[134] T. Matsuoka, H. Okamoto, M. Nakao, H. Harima and E. Kurimoto, "Optical bandgap energy of wurtzite InN," *Applied Physics Letters*, vol. 81, no. 7, pp. 1246-1248, 2002.

[135] D. K. Gaskill, C. D. Brandt and R. J. Nemanich, "III-Nitride, SiC and Diamond Materials for Electronic Devices," in *MATERIALS RESEARCH SOCIETY PITTSBURGH PA*, San Francisco, California, USA, 1996.

[136] G. Orsal, Y. E. Gmili, N. Fressengeas, J. Streque, R. Djerboub, T. Moudakir, S. Sundaram, A. Ougazzaden and J. Salvestrini, "Bandgap energy bowing parameter of strained and relaxed InGaN layers," *Optical Materials Express*, vol. 4, no. 5, pp. 1030-1041, 2014.

[137] A. Fischer, H. Kuhne and H. Richter, "New approach in equilibrium theory for strained layer relaxation," *Physical review letters*, vol. 73, no. 20, p. 2712, 1994.

[138] Y. Kataoka, "Standardless X-ray fluorescence spectrometry (Fundamental parameter method using sensitivity library)," *The Rigaku Journal*, vol. 6, no. 1, pp. 33-39, 1989.

[139] L. G. Parratt, "Surface studies of solids by total reflection of X-rays.," *Physical review*, vol. 95, no. 2, p. 359, 1954.

[140] M. A. Moram and M. E. Vickers, "X-ray diffraction of III-nitrides.," *Reports on progress in physics.,* vol. 72, no. 3, p. 036502, 2009.

[141] B. a. Gil., Physics of Wurtzite Nitrides and Oxides: Passport to Devices, Springer.

[142] J. Lehmann, C. Leroux, G. Reimbold, M. Charles, A. Torres, E. Morvan, Y. Baines, G. Ghibaudo and E. Bano, "Novel sheet resistance measurement on AlGaN/GaN HEMT wafer adapted from four-point probe technique," *In Proceedings of the 2015 International Conference on Microelectronic Test Structures IEEE,* pp. 163-168, 2015.

[143] J. Lehmann, "Caractérisation électrique d'hétérostructures AlGaN/GaN pour des applications de puissance.," *Doctoral dissertation,* 2015.

[144] I. Nifa, "Caractérisation et modélisation du gaz 2D des dispositifs MIS-HEMTs sur GaN.," *Doctoral dissertation,* 2018.

[145] "http://www.4probes.com/Support_DownLoad/ASTM%20F390-98(2003).PDF".

[146] R. Butté, J. F. Carlin, E. Feltin, M. Gonschorek, S. Nicolay, G. Christmann, D. Simeonov, A. Castiglia, J. Dorsaz, H. J. Buehlmann, S. Christopoulos, G. Baldassarri H v H, A. J. D. Grundy, M. Mosca, C. Pinquier, M. A. Py and N. Grandjean, "Current status of AlInN layers lattice-matched to GaN for photonics and electronics," *Journal of Physics D: Applied Physics,* vol. 40, no. 20, p. 6328, 2007.

[147] L. Semra, A. Telia, K. M. and A. Soltani, "Effects of spontaneous and piezoelectric polarization on AlInN/GaN heterostructure.," *In 2012 International Conference on Engineering and Technology (ICET) IEEE,* pp. 1-4, 2012.

[148] M. Hiroki, Y. Oda, N. Watanabe, N. Maeda, H. Yokoyama, K. Kumakura and H. Yamamoto, "Unintentional Ga incorporation in metalorganic vapor phase epitaxy of In-containing III-nitride semiconductors," *Journal of Crystal Growth,* vol. 382, pp. 36-40, 2013.

[149] J. Lu, J. Su, R. Arif, G. D. Papasouliotis and A. Paranjpe, "Epitaxial Growth of InAlN/GaN Heterostructures on Silicon Substrates in a Single Wafer Rotating Disk MOCVD Reactor," *MRS Advances,* vol. 2, no. 5, pp. 329-334, 2017.

[150] R. Bouveyron and M. B. Charles, "Growth by MOCVD of In (Ga) AlN alloys, and a study of gallium contamination in these layers under nitrogen and hydrogen carrier gas," *Journal of Crystal Growth,* vol. 464, pp. 105-111, 2017.

[151] J. Lu, J. Su, R. Arif, G. D. Papasouliotis and A. Paranjpe, "Epitaxial Growth of InAlN/GaN Heterostructures on Silicon Substrates in a Single Wafer Rotating Disk MOCVD Reactor," *MRS Advances,* vol. 2, no. 5, pp. 329-334, 2017.

[152] M. Hiroki, Y. Oda, N. Watanabe, N. Maeda, H. Yokoyama, K. Kumakura and H. Yamamoto, "Unintentional Ga incorporation in metalorganic vapor phase epitaxy of In-containing III-nitride semiconductors," *Journal of Crystal Growth,* vol. 382, pp. 36-40, 2013.

[153] M. Mrad, M. Charles, Y. Mazel, E. Nolot, J. Kanyandekwe, M. Veillerot, P. Ferret and G. Feuillet, "Understanding and controlling Ga contamination in InAlN barrier layers.," *Journal of Crystal Growth,* vol. 507, pp. 139-142, 2019.

[154] Y. Mazel, E. Nolot, J. P. Barnes, M. Charles, R. Bouveyron and M. Mrad, "Multitechnique elemental depth profiling of InAlGaN and InAlN films," *Journal of Vacuum Science & Technology B,* vol. 36, no. 3, p. 03F119, 2018.

[155] J. Lehmann, C. Leroux, M. Charles, A. Torres, E. Morvan, D. Blachier, G. Ghibaudo, E. Bano and G. Reimbold, "Sheet resistance measurement on AlGaN/GaN wafers and dispersion study," *Microelectronic Engineering,* vol. 109, pp. 334-337, 2013.

[156] S. Choi, H. J. Kim, Z. Lochner, J. Kim, R. D. Dupuis, A. M. Fischer, R. Juday, Y. Huang, T. Li, J. Y. Huang, F. A. Ponce and J. H. Ryou, "Origins of unintentional incorporation of gallium in AlInN layers during epitaxial growth, part I: Growth of AlInN on AlN and effects of prior coating. Journal of Crystal Growth," *Journal of Crystal Growth,* vol. 388, pp. 137-142, 2014.

[157] J. J. Zhu, Y. M. Fan, H. Zhang, G. J. Lu, H. Wang, D. G. Zhao, D. S. Jiang, Z. S. Liu, S. M. Zhang, G. F. Chen, B. S. Zhang and H. Yang, "Contribution of GaN template to the unexpected Ga atoms incorporated into AlInN epilayers grown under an indium-very-rich condition by metalorganic chemical vapor deposition (MOCVD)," *Journal of Crystal Growth,* vol. 348, no. 1, pp. 25-30, 2012.

[158] J. Kim, Z. Lochner, M. H. Ji, S. Choi, H. J. Kim, J. S. Kim, R. D. Dupuis, A. M. Fischer, R. Juday, H. Huang, T. Li, J. Y. Huang, F. A. Ponce and J. H. Ryou, "Origins of unintentional incorporation of gallium in InAlN layers during epitaxial growth, part II: Effects of underlying layers and growth chamber conditions," *ournal of Crystal Growth,* vol. 388, pp. 143-149, 2014.

[159] M. Mrad, L. Christophe, D. Amélie, Y. Victor, R. Jérôme, L. Matthieu, K. Joel, F. Guy and C. Matthew, "Unravelling the unwanted Ga incorporation effect on InGaN epilayers grown in CCS MOVPE reactors," *Journal of Crystal Growth,* vol. 536, p. 125596, 2020.

[160] F. Yam and Z. Hassan, "InGaN: An overview of the growth kinetics, physical properties and emission mechanisms," *Superlattices and Microstructures,* vol. 43, no. 1, pp. 1-23, 2008.

[161] T. Miyoshi, S. Masui, T. Okada, T. Yanamoto, T. Kozaki, S. I. Nagahama and T. Mukai, "510–515 nm InGaN-based green laser diodes on c-plane GaN substrate," *Applied Physics Express,* vol. 2, no. 6, p. 062201, 2009.

[162] Y. Enya, Y. Yoshizumi, T. Kyono, K. Akita, M. Ueno, M. Adachi, T. Sumitomo, S. Tokuyama, T. Ikegami, K. Katayama and T. Nakamura, "531 nm green lasing of InGaN based laser diodes on semi-polar {2021} free-standing GaN substrates," *Applied Physics Express,* vol. 2, no. 8, p. 082101, 2009.

[163] A. Avramescu, T. Lermer, J. Müller, S. Tautz, D. Queren, S. Lutgen and U. Strauß, "InGaN laser diodes with 50 mW output power emitting at 515 nm," *Applied Physics Letters,* vol. 95, no. 7, p. 071103, 2009.

[164] K. Mukose and M. Sano, "Theoretical study of composition fluctuation in InGaN films on various substrates," *Journal of Physics: Conference Series,* vol. 152, no. 1, p. 012025, 2009.

[165] A. Even, G. Laval, O. Ledoux, P. Ferret, D. Sotta, E. Guiot, F. Levy, I.C.Robin and A. Dussaigne, "Enhanced In incorporation in full InGaN heterostructure grown on relaxed InGaN pseudo-substrate," *Applied Physics Letters,* p. 262103, 2017.

[166] D. Sotta, A. Dussaigne, S. Chenot and B. Damilano, "Soitec's Relaxed InGaN Substrates Enable Pure Red Emission for Full-Color Micro LED Displays," 5 November 2018. [Online]. Available:

https://www.ledinside.com/press/2018/11/soite_relaxed_ingan_substrates_enable_pure_red_emission_for_fullcolor_micro_led_displays.

[167] L. Redaelli, A. Mukhtarov, S. Valdueza-Felip, A. Ajay, C. Bougerol, C. Himwas, J. Faure-Vincent, C. Durand, J. Eymery and E. Monroy, "Effect of the quantum well thickness on the performance of InGaN photovoltaic cells," *Applied Physics Letters*, vol. 105, no. 13, p. 131105, 2014.

[168] Y. Guo, X. L. Liu, H. P. Song, A. L. Yang, X. Q. Xu, G. L. Zheng, H. Y. Wei, S. Y. Yang, Q. S. Zhu and Z. G. Wang, "A study of indium incorporation in In-rich InGaN grown by MOVPE," *Applied Surface Science*, vol. 256, no. 10, pp. 3352-3356, 2010.

[169] K. Zhou, H. Ren, M. Ikeda, J. Liu, Y. Ma, S. Gao, C. Tang, D. Li, L. Zhang and H. Yang, "Unintentional gallium incorporation in InGaN layers during epitaxial growth," *Superlattices and Microstructures*, vol. 101, pp. 323-328, 2017.

[170] M. Hiroki, Y. Oda, N. Watanabe, N. Maeda, H. Yokoyama, K. Kumakura and H. Yamamoto, "Unintentional Ga incorporation in metalorganic vapor phase epitaxy of In-containing III-nitride semiconductors," *Journal of crystal growth*, vol. 382, pp. 36-40, 2013.

[171] M. Mrad, M. Charles, Y. Mazel, E. Nolot, J. Kanyandekwe, M. Veillerot, P. Ferret and G. Feuillet, "Understanding and controlling Ga contamination in InAlN barrier layers," *Journal Of Crystal Growth*, vol. 507, pp. 139-142, 2019.

[172] N. A. Kaufmann, L. Lahourcade, B. Hourahine, D. Martin and N. Grandjean, "Critical impact of Ehrlich–Schwöbel barrier on GaN surface morphology during homoepitaxial growth," *Journal of Crystal Growth*, vol. 433, pp. 36-42, 2016.

[173] M. Charles, Y. Baines, A. Bavard and R. Bouveyron, "High growth rate GaN on 200 mm silicon by metal-organic vapor phase epitaxy for high electron mobility transistors," *Journal of Crystal Growth*, vol. 483, pp. 89-93, 2018.

[174] M. Charles, K. Joël and L. Matthieu, "Simple and Accurate Prediction of AlGaN Metal-Organic Vapor Phase Epitaxy Growth," *physica status solidi (b)*, p. 1900576, 2020.

[175] C. Matthew, B. Yannick, B. Renan and P. Anne-Marie, "The Characterization and Optimization of GaN Cap Layers and SiN Cap Layers on AlGaN/GaN HEMT

Structures Grown on 200 mm GaN on Silicon," *physica status solidi (b),* vol. 255, no. 5, p. 1700406, 2018.

[176] K. Junji, T. Shuichi, M. Toyoo, N. Norikazu, K. Toshihide, W. Keiji and I. Kenji, "Tensile strain-induced formation of micro-cracks for AlGaN/GaN heterostructures," *physica status solidi c ,* vol. 10, no. 5, pp. 808-811, 2013.

[177] M. D. Smith, D. Thomson, V. Z. Zubialevich, H. L. G. Naresh-Kumar, C. Trager-Cowan and P. J. Parbrook, "Nanoscale fissure formation in AlxGa1–xN/GaN heterostructures and their influence on ohmic contact formation," *physica status solidi (a),* vol. 214, no. 1, p. 1600353, 2017.

[178] R. A. Talalaev, E. V. Yakovlev, S. Y. Karpov and Y. N. Makarov, "On low temperature kinetic effects in metal–organic vapor phase epitaxy of III–V compounds," *Journal of crystal growth,* vol. 230, no. 1-2, pp. 232-238, 2001.

[179] "Engineering ToolBox, Thermal Conductivity of common Materials and Gases," 2003. [Online]. Available: https://www.engineeringtoolbox.com/thermal-conductivity-d_429.html.

[180] M. Mrad, Y. Mazel, J. Kanyandekwe, R. Bouveyron, G. Feuillet and M. Charles, "Solving the problem of gallium contamination problem in InAlN layers in close coupled showerhead reactors," *Applied Physics Express,* vol. 12, no. 4, p. 045504, 2019.

Scientific contributions resulting from this work

Journal papers:

[1] M. Mrad, M. Charles, Y. Mazel, E. Nolot, J. Kanyandekwe, M. Veillerot, P. Ferret, G. Feuillet. Understanding and controlling Ga contamination in InAlN barrier layers. **Journal of Crystal Growth** vol. 507, page 139-142, 2019.

[2] M. Mrad, Y. Mazel, J. Kanyandekwe, R. Bouveyron, G. Feuillet, M. Charles. Solving the problem of gallium contamination problem in InAlN layers in close coupled showerhead reactors. **Applied Physics Express** vol. 12, page 045504, 2019.

[3] M. Mrad, C. Licitra, A. Dussaigne, V. Yon, J. Richy, M. Lafossas, J. Kanyandekwe, G. Feuillet, M. Charles. Unravelling the unwanted Ga incorporation effect on InGaN epilayers grown in CCS MOVPE reactors. **Journal of Crystal Growth** vol. 536, page p.125596, 2020.

Selected conferences:

[4] M. Mrad, J. Kanyandekwe, Y. Mazel, V. Yon, G. Feuillet, M. Charles. **Oral presentation**, 13th International Conference on Nitride Semiconductors 2019 (ICNS-13), Bellevue, Washington, USA, July 2019.

[5] M. Mrad, C. Licitra, A. Dussaigne, V. Yon, J. Richy, M. Lafossas, J. Kanyandekwe, G. Feuillet, M. Charles. **Oral presentation**, SPIE. Photonics West - OPTO, San Francisco, California, USA, February 4.

[6] M. Mrad, M. Charles, Y. Mazel, E. Nolot, J. Kanyandekwe, M. Veillerot, P. Ferret, G. Feuillet. **Oral presentation**, 19th International Conference on Metalorganic Vapor Phase Epitaxy (ICMOVPE-XIX), Nara, Japan, June 2018.

[7] M. Mrad, M. Charles, V. Yon, J. Kanyandekwe, E. Nolot, Y. Mazel, P. Ferret, A. Dussaigne, G. Feuillet. **Oral presentation**, 2018 Fall Meeting | EMRS - European Materials Research Society, Warsaw, Poland, September 2018.

[8] M. Mrad, M. Charles. **Poster presentation**, 17th European Workshop on Metalorganic Vapor Phase Epitaxy (EW-MOVPE17), Grenoble, France, June 2017.